LED-Based Photoacoustic Imaging of the Lymphatic Vessels

Master's Thesis

Saskia van Heumen

LED-BASED PHOTOACOUSTIC IMAGING OF THE LYMPHATIC VESSELS

Saskia van Heumen

Student number: 4345479

16 Dec 2021

Thesis in partial fulfilment of the requirements for the joint degree of Master of Science in

Technical Medicine

Leiden University; Delft University of Technology; Erasmus University Rotterdam

Master thesis project (TM30004; 35 ECTS)

Dept. of Plastic and Reconstructive Surgery, Erasmus MC

Dept. of Biomedical Engineering, Erasmus MC

March 2021 – December 2021

Supervisor(s):

Prof. Gijs van Soest, PhD

Dalibor Vasilic, MD, PhD

Jonas Riksen, MSc

Thesis committee members:

Prof. Gijs van Soest, PhD (Chair)

Dalibor Vasilic, MD, PhD

Willem Grootjans, PhD

Eleftheria Astreinidou, PhD

Jonas Riksen, MSc

Preface and acknowledgements

This thesis marks the end of my time as a Technical Medicine student. Ever since I was young, I was intrigued by the human body and how technology was used to treat the most complex disease cases. Because of this, I was so excited to be part of the first 100 students to start with the bachelor's degree Clinical Technology in Delft, Leiden and Rotterdam. During my second-year master internships I became increasingly interested in implementing imaging for surgical planning and evaluation. When I came across the *photoacoustic imaging of the lymphatic vessels* project, it was the perfect combination between surgical planning, advanced imaging techniques and organizational aspects of research for a technical medicine thesis project. Even though lymphatic surgery and photoacoustic imaging were relatively unfamiliar territory for me, I was eager to learn more. Now, 9 months later, I can say that this was truly an exciting and challenging experience. I look forward implementing the knowledge and skills I gained in the future.

This thesis would not have been possible without my supervisors and I would like to express my sincere gratitude toward Gijs, Dalibor and Jonas. Gijs, thank you for your view on the project and motivating me to stay critical during every step of this project. I always appreciated your elaborate feedback and helping me to keep my head in the game. Dalibor, thank you for always welcoming me to join you in the outpatient clinic and operating room. These days have not only helped me grasp the medical side of this project but have also shown everything that encompasses complex reconstructive surgery. I always loved discussing technological innovations in surgery, your enthusiasm was truly infectious. Jonas, I am extremely glad you were part of the project. Without your valuable input and critical review of all documentation, the final product would not have been where it is now. It was nice to collaborate and discuss with someone with a similar background. I also thank the lighthearted lab for welcoming me in the group and helping me along the way. I would also like to extend a thanks to Mithun Singh. Your input and expertise on photoacoustic imaging and troubleshooting gave me the knowledge and skills to use the Acoustic X.

Finally, I would like to thank my friends and family for their support during this process. I would like to especially thank my mom and dad for their unconditional support and making life during Covid-19 a little easier with your endless ideas to treat myself every once in a while. You always help me to strive for the best and always support me to pursue what I love to do.

Saskia van Heumen
Delft, December 2021

Summary

Lymphedema is the accumulation of protein-rich fluid in the intersitium (i.e., dermal backflow (DBF)), causing swelling. It is a commonly seen due to iatrogenic damage to the lymphatics after surgical and radiotherapeutic treatment of cancer. An important microsurgical treatment is lymphovenous bypass (LVB) surgery, during which a lymphatic vessel is anastomosed to a vein to bypass the site of lymphatic flow obstruction. Pre-operative imaging of the lymphatic vessels is a prerequisite for planning of LVB surgery. Imaging of these structures is challenging due to the small size of the lymphatic vessels and the lack of inherit contrast of the lymphatic fluid. In this thesis, we investigated the feasibility of lymphatic vessel imaging using light emitting diode (LED) based photoacoustic imaging (PAI) for LVB surgical planning.

Chapter 1 gives an introduction to the physiology of lymphedema and (surgical) treatment options for lymphedema. Current challenges related to lymphatic vessel imaging and pre-operative planning are also discussed.

The systematic review in **Chapter 2** gives an overview of the existing imaging modalities used for pre-operative visualization of the lymphatic vessels. Findings of the systematic literature review emphasized the importance of adequate imaging for clinical decision making and showed the heterogeneity of the field. Indocyanine green (ICG) contrast mediated near-infrared fluorescence lymphography (NIRF-L) has become the most popular in recent years and is currently used at the Erasmus Medical Center Rotterdam. NIRF-L facilitates lymphatic vessel depiction and lymphedema severity assessment based on the extent of DBF. However, NIRF-L has a low resolution and cannot visualize lymphatic vessels in the presence of DBF. Photoacoustic imaging (PAI) using LED light pulses is a novel technique that has properties that may overcome some of the disadvantages of NIRF-L.

Chapter 3 introduces the technical principles of PAI, and dual-wavelength PAI of ICG contrast and hemoglobin in blood is discussed. We performed phantom experiments to show the effect of several parameters on the image quality and demonstrate principle of dual-wavelength (820 & 940 nm) PAI of ICG and blood. The experimental results showed that the ratio between the PA signal at 940 nm and 820 nm differentiates blood from ICG. The 940/820 nm ratio might therefore be useful for in-vivo imaging of the lymphatic vessels and veins. With regards to imaging parameters, there is a trade-off between the frame rate and the image quality depending on the application (static or dynamic processes), and absorber characteristics and depth. Finally, the light pulse width must be tuned based on imaging target characteristics, the desired resolution and signal strength, and the fractional bandwidth of the ultrasound probe.

Chapter 4 describes preliminary results of a clinical feasibility study on handheld LED-based PAI of the lymphatic vessels in patients with secondary limb lymphedema. We investigated novel features such as the possibility of visualizing lymphatic vessel contractility and lymphatic vessel depiction behind DBF patterns. To date, three patients with breast-cancer related lymphedema were included in the study. We demonstrated that dual-wavelength, LED-based PAI can visualize lymphatic and blood vessels even in the presence of DBF. These findings suggest that PAI has potential for pre-operative lymphedema assessment, especially in cases with extensive DBF pattern hindering adequate assessment with NIRF-L.

Chapter 5 provides an overall discussion and future challenges are discussed. In this thesis we demonstrated the potential for lymphatic vessel identification using PAI. However, LED-based PAI is still consistently being improved. Our findings need to be confirmed in larger groups of patients and additional clinical studies. Technological advances are needed to improve user experience, image quality and minimize image artefacts.

List of abbreviations

ABR	Algemeen beoordelings- en registratieformulier
BMI	Body Mass Index
CCMO	Centrale Commissie Mensgebonden Onderzoek
CE	Conformité Européenne
CEMRL	Contrast Enhanced Magnetic Resonance Lymphography
CLG	Cheng's Lymphedema Grade
CT	Computed tomography
CDT	Complete decongestive therapy
CHFUS	Conventional High Frequency Ultrasound
CNR	Contrast to Noise Ratio
DARC	Dual-agent relaxation contrast
DBF	Dermal Backflow
DBS	Dermal Backflow Scale
DPIA	Data Protection Impact Assessment
e-CRF	Electronic Case Report Form
EMC	Erasmus University Medical Center Rotterdam
EU	European Union
FSE	Fast Spin Echo
FWHM	Full Width Half Maximum
GRE	Gradient-recalled echo
ICG	Indocyanine Green
IMDD	Investigational Medical Device Dossier
ISF	Investigator Site File
ISL	International Society of Lymphology
LED	Light Emitting Diode
LSG	Lymphoscintigraphy
LVB	Lymphovenous bypass
MDACC	MD Anderson Cancer Center
MDR	Medical Device Regulation (EU)
MEC-U	Medical Research Ethics Committees United
MIP	Maximum Intensity Projection
MLD	Manual Lymphatic Drainage
MRL	Magnetic Resonance Lymphography
MREC	Medical Research Ethics Committee (Dutch: Medisch Ethische Toetsingscommissie (METC))
NCMRL	Non-Contrast Magnetic Resonance Lymphography
NEB	NOTA-Evans Blue
NIRF-L	Near Infrared Fluorescence Lymphography

PA	Photoacoustic
PAI	Photoacoustic imaging
PET	Positron Emission Tomography
PMCF	Post Market Clinical Follow-up
PRF	Pulse Repetition Frequency
ROI	Region of Interest
SNR	Signal to Noise Ratio
SPECT	Single Photon Emission Computed Tomography
TAT	Tracer appearance time
TI	Transport Index
TLS	Taiwan Lymphoscintigraphy Staging
TMF	Trial Master File
TT	Transit time
UHFUS	Ultra-High Frequency Ultrasound
US	Ultrasound
VLNT	Vascularized Lymph Node Transfer
WMO	Medical Research Involving Human Subjects Act (Dutch: Wet medisch-wetenschappelijk onderzoek)

Table of contents

1

An introduction to lymphedema

1.1 Clinical context

1.1.1 The lymphatic system

The lymphatic system is a network of tissues, vessels and organs that fulfills several functions and is relatively poorly understood and understudied. The primary function is transportation of interstitial fluids and proteins to the blood circulation while maintaining osmotic and hydrostatic pressure within the interstitial space.[1] The lymphatic system also plays a critical role in mediating the immune response and is the primary route for spread of tumor cells.[2]

Small lymphatic capillaries initially collect the lymphatic fluid which flow to the lymphatic trunks back to the circulatory system via precollectors and larger collecting lymphatic vessels. During transport, lymphatic fluid passes through lymph nodes stationed throughout the body, such as the inguinal and the axillary lymph nodes.[3]

Unlike the blood circulatory system, lymphatic transport is not facilitated by a central pump. Two main factors contributing towards adequate lymph flow are extrinsic/passive forces (i.e., muscle contractions in the extremities, inflow pressure or outflow resistance) and intrinsic/active forces (i.e., lymphatic vessel contractions). Unidirectional valves divide the collecting lymphatic vessels in subsequent elementary pumping units and prevent backflow. Periodically coordinated contractions of smooth muscle layers around the lymphatic vessel segments, propel the lymphatic fluid forward toward the next pumping unit.[4]

1.1.2 Lymphedema

Dysfunction or obstruction of the lymphatic system impairs the essential transport function and can manifest in formation of incompetent valves and buildup of the lymphatic fluid in the superficial dermal layer (i.e., dermal backflow (DBF)), causing lymphedema.[4] Figure 1.1 shows the lymphatic system at different depths in normal and obstructed scenarios schematically.

There are two types of lymphedema, namely primary and secondary. In primary lymphedema, congenital malformations of the lymphatic system cause failure of lymphatic fluid transport, while in secondary lymphedema external damage to the lymphatics is the cause. Secondary limb lymphedema is most prevalent and often associated with radiotherapeutic and surgical cancer treatment.[5-7] Damage to the lymphatic system leads to a complex progressive pathology of edema, chronic inflammation and even irreversible fibrosis. Since survival rates of cancer treatment have increased substantially, long term effects of the treatment have come to light more often.[8] Lymphedema is not a life-threating condition but has a major impact on quality of life and can cause life-long discomfort, pain and psychological distress.[9]

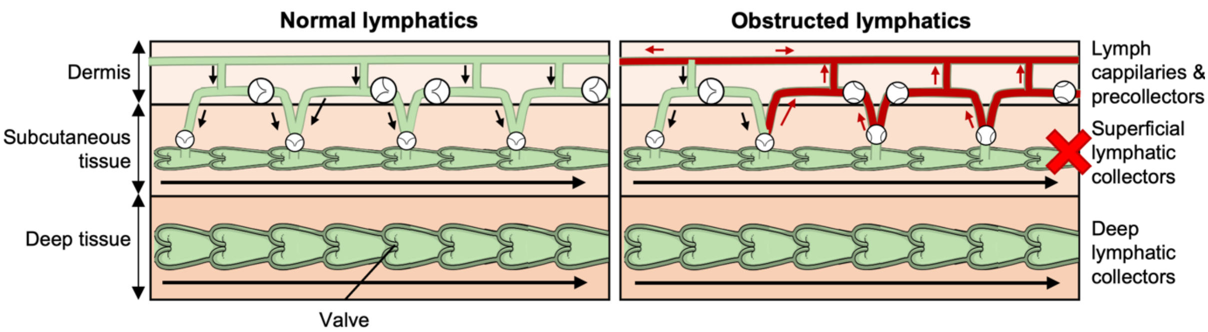

Figure 1.1 Overview of physiology of lymphedema due to proximal obstruction causing dermal backflow. The left image represents the layers of the healthy lymphatic system. Lymphatic vessels consist of elementary pumping units with unidirectional valves in between to make sure lymph can only flow in one direction. The right image represents obstructed lymphatics where the lymphatic fluid cannot flow anymore due to some type of damage (red cross). This causes a pressure rise in the lymphatic vessel and eventually backflow of the lymphatic fluid to the superficial layers, causing swelling.

1.1.3 Lymphedema diagnosis and treatment

Diagnosis of lymphedema is generally based on the clinical presentation and medical history of a patient. Confounding factors such as obesity or venous insufficiency can complicate the final diagnosis.[10] Clinical severity staging is mostly done using the four stage International Society of Lymphology (ISL) scale for classification of a lymphedematous limb (see Table 1.1).[11]

Table 1.1: International Society of Lymphology lymphedema clinical staging scale[11]

ISL stage	Characteristics	Severity
0	Latent or sub-clinical condition: swelling is not evident despite impaired lymph transport. Patients can complain of heaviness or aching of the affected body part. It can take years before swelling becomes evident.	
1	Reversible lymphedema: early onset of the condition where accumulation of tissue fluid results in visible swelling and subsides with limb elevation. The edema may be pitting at this stage.	Mild - <20% increase in excess limb volume
2	Irreversible lymphedema: swelling does not subside with limb elevation and pitting is manifested.	Moderate – 20-40% increase in excess limb volume
3	Lymphostatic elephantiasis: Tissue is hard (fibrotic) and pitting is absent. Trophic skin changes such as acanthosis, fat deposits and warty overgrowths develop.	Severe - >40% increase in excess limb volume

Conventional non-surgical treatment is the first step toward alleviation of the symptoms and consists of a two-phase complete decongestive therapy (CDT). It encompasses meticulous skin care, manual lymph drainage (MLD) to encourage lymph flow, range of motion exercises and compression garment therapy.[11,12] For secondary lymphedema patients that are refractory to conventional treatment, microsurgical lymphovenous bypass (LVB) surgery has become a good alternative to alleviate symptoms and slow down deterioration of the lymphatic vessels. During LVB surgery, one or multiple small incisions (~ 2 cm) are made and (patent) lymphatic vessels are anastomosed to nearby veins. Figure 1.2 shows a schematic of the LVB surgery. The goal of the anastomosis is to divert the lymphatic fluid into the blood circulation before lymphatic transport fails more proximally in the limb, thus preventing DBF.[13-16] This reduces the amount of lymphatic fluid buildup and swelling of the limb. Ultimately the goal is to reduce the intensity of CDT needed.

In severe cases, surgeons opt for vascularized lymph node transfer (VLNT) due to for example the absence of suitable lymphatic vessels for anastomosis.[17] A lymph node is transplanted to the lymphedema limb from elsewhere in the body and functions as a biological vacuumlike pump and drain.[18] This procedure is more extensive and invasive compared to LVB and has the risk of donor site lymphedema. LVB and VLNT aim to tackle the physiological aspects of lymphedema. Debulking procedures such as liposuction and wedge resection are sometimes used to remove built up fibrotic tissue and treat the symptoms of the underlying pathological processes.[17]

A minimum requirement for LVB surgery is finding a suitable lymphatic vessel and vein for anastomosis, which is difficult due to small size of the lymphatic vessels (< 1 mm). Pre-operative localization of the lymphatic vessel is crucial, since the surgery is ideally performed with a small incision. Another important aspect is the degree of lymphosclerosis since the efficacy of the LVB depends largely on the presence of the lymphatic pump. Knowledge on the level of sclerosis and/or lymphatic vessel contractility benefits surgical outcomes.[19]

For this reason, pre-surgical imaging is done to determine if a patient is a surgical candidate and identify the anastomosis site.

1.1.4 Image based surgical planning using fluorescence imaging

Currently, the Erasmus MC University Medical Center Rotterdam uses near-infrared fluorescence lymphography (NIRF-L) for visualization of the lymphatic vessels and DBF using subcutaneous injections of indocyanine green (ICG). ICG is a safe exogenous contrast agent and binds to serum albumin, which is transported in lymphatic fluid.

NIRF-L utilizes the fluorescence properties of ICG where a region of interest is illuminated with light at the excitation wavelengths of 760 nm. The resulting fluorescence light (peak wavelength at 845 nm) is detected and displayed.[20-22] The severity of lymphedema is assessed based on the MD Anderson Cancer Center (MDACC) scale (see Figure 1.3) and potential anastomosis sites are identified.[23] If no patent lymphatic vessels are observed such as in MDACC stage 4 and 5, VLNT is often considered.

NIRF-L provides real-time imaging of lymphatic transport and is used to identify potential suitable lymphatic vessel for anastomosis.[24-28] However, NIRF-L lacks information about the depth of the lymphatic vessels and has low resolution. Lymphatic vessels might be missed when the superficial signal from DBF masks any deeper signal. Moreover, veins cannot be visualized with NIRF-L,[28-31] which can lead to uncertainties in LVB site selection and even surgical failure due to the absence of a vein in the surgical field.

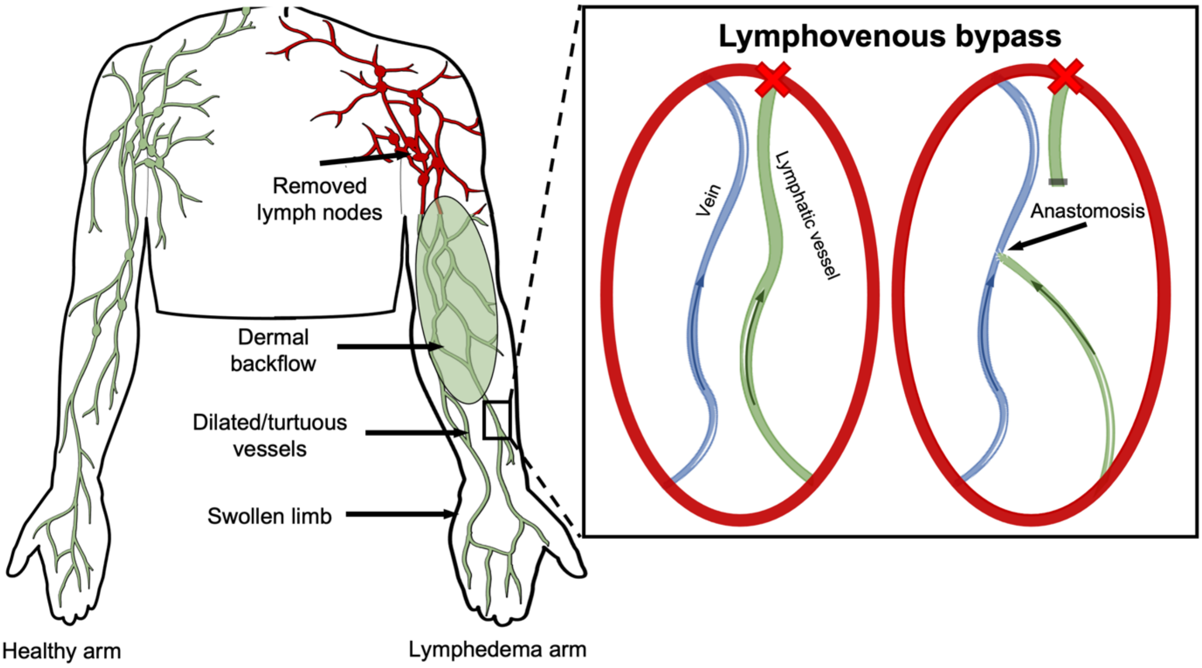

Figure 1.2: Schematic of (secondary) lymphedema and lymphovenous bypass. Lymphedema due to damage to the lymph nodes (dissection/radiotherapy) lead to a blockage of lymph flow. This result in dilated and tortuous lymphatic vessels and backflow of the lymphatic fluid into the superficial layer (dermal backflow). With the lymphovenous bypass surgery a lymphatic vessel is anastomosed to a vein to divert the lymphatic fluid into the blood circulation and prevent dermal backflow and swelling of the affected area.

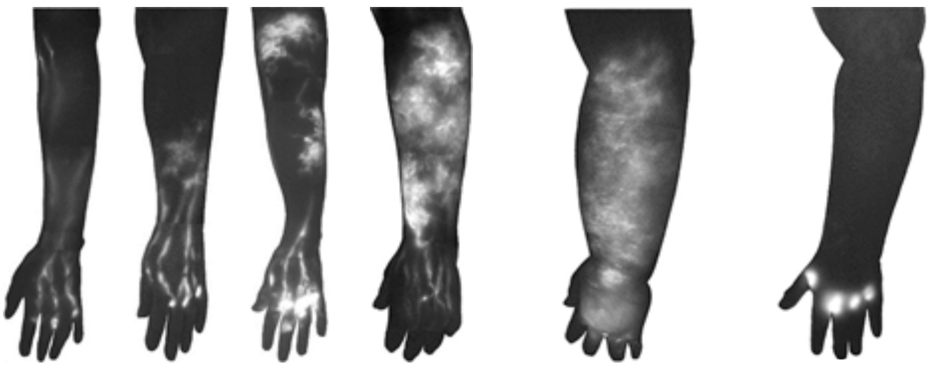

Stage	0	1	2	3	4	5
Patent lymphatic vessels	++++	+++	++	+	0	0
Dermal backflow	0	+	++	+++	++++ finger/toe palm/sole signs	0
Lymphatic vessel contractility	++++	+++	++	+	0	0

Figure 1.3: MD Anderson Clinical Center Indocyanine Green Fluorescence Lymphography Staging Scale. Modified from ref[23]

1.1.5 Photoacoustic imaging

Photoacoustic imaging (PAI) is an imaging modality based on the photoacoustic effect. It exploits the advantages of optical imaging contrast and the resolution of ultrasound imaging. Pulsed near-infrared light illuminates a region of interest followed by optical absorption in the tissue. Chromophores of interest such as ICG in the lymphatic vessels and hemoglobin in blood vessels have specific optical absorption characteristics, which can be used for PAI. Optical absorption leads to thermoelastic expansion, resulting in pressure waves that propagate through the tissue and are detected by an ultrasound probe on the tissue surface. The detected acoustic waves are reconstructed to form the photoacoustic image which represents the optical absorption.[32]

PAI has shown its potential in multiple clinical fields to visualize physiological changes such as pathological angiogenesis on a small scale.[33,34] By combining multiple excitation wavelengths, both ICG in the lymphatic vessels and hemoglobin in blood can be visualized and differentiated. Moreover, high resolution information is available in all three dimensions.[35]

Although commercial systems are available, PAI is still an emerging technology. Translation into clinical practice is still rather complicated due to the dependency of high-power lasers for tissue illumination. These systems are bulky, expensive and demand additional safety measures.[36-38] Substituting lasers with light emitting diodes (LED), even though accompanied with their own disadvantages due to significantly lower light pulse energy, overcomes the previously mentioned drawbacks of lasers. In recent years, developments have made it possible to obtain sufficient image quality for clinical implementation of LED-based systems.[39,40]

1.2 Master's thesis objective and outline

Due to the small scale of the lymphatic system and colorless nature of the lymphatic fluid, imaging of these structures is not straightforward and poses challenges. Ideally, an imaging modality:

- Can visualize lymphatic vessels in three dimensions
- Can visualize receiving veins in three dimensions
- Can perform real-time imaging
- Can visualize lymphatic vessel functionality (i.e., contractions)
- Is portable for easy implementation in multiple clinical settings (outpatient clinic & operating room)

The goal of this thesis is to investigate the clinical feasibility of LED-based photoacoustic imaging of lymphatic vessels and the venous network for the purpose of lymphovenous bypass surgical planning.

This thesis consists of four different subgoals (Figure 1.4):

1. Conduct a systematic literature review to give an overview of modalities used for lymphatic vessel imaging.
2. Coordinate and write a Medical Research Ethics Committee (MREC) application for a clinical feasibility study with an LED-based photoacoustic imaging device.
3. Set up and execute phantom experiments to investigate parameters influencing photoacoustic imaging quality.
4. Carry out a clinical feasibility study for LED-based photoacoustic imaging of the lymphatic vessels in patients with secondary limb lymphedema.

Figure 1.4: Thesis subgoals

This thesis is composed of four chapters.

Chapter 2 provides a systematic literature review of the existing imaging modalities used for pre-operative visualization of the lymphatic vessels. The most important findings, advantages and disadvantages for each modality in the perspective of (micro)surgical interventions of lymphedema are described.

Chapter 3 begins by laying out the photoacoustic principle and LED-based photoacoustic imaging of lymphatic vessels and veins. Next, phantom experiments are presented to show the effect of several (imaging) parameters on the image quality and demonstrate principle of simultaneous photoacoustic imaging with of ICG and blood.

Chapter 4 describes the preliminary findings of a clinical feasibility study on LED-based photoacoustic imaging of the lymphatic vessels in patients with secondary limb lymphedema.

Chapter 5 provides an overall discussion and conclusion. Lastly, future challenges and research are also discussed. Supporting documents, particularly related to the MREC approval process are included as appendices.

1.3 References

1 Swartz, M. A. The physiology of the lymphatic system. *Adv. Drug Deliv. Rev.* 2001;(50):3-20, doi:10.1016/S0169-409X(01)00150-8.

2 Randolph, G. J., Ivanov, S., Zinselmeyer, B. H. et al. The Lymphatic System: Integral Roles in Immunity. *Annu. Rev. Immunol.* 2017;(35):31-52, doi:10.1146/annurev-immunol-041015-055354.

3 Breslin, J. W., Yang, Y., Scallan, J. P. et al. Lymphatic Vessel Network Structure and Physiology. *Compr. Physiol.* 2018;(9):207-299, doi:10.1002/cphy.c180015.

4 Scallan, J. P., Zawieja, S. D., Castorena-Gonzalez, J. A. et al. Lymphatic pumping: mechanics, mechanisms and malfunction. *J. Physiol.* 2016;(594):5749-5768, doi:10.1113/JP272088.

5 Cormier, J. N., Askew, R. L., Mungovan, K. S. et al. Lymphedema beyond breast cancer. *Cancer.* 2010;(116):5138-5149, doi:10.1002/cncr.25458.

6 DiSipio, T., Rye, S., Newman, B. et al. Incidence of unilateral arm lymphoedema after breast cancer: a systematic review and meta-analysis. *Lancet. Oncol.* 2013;(14):500-515, doi:10.1016/S1470-2045(13)70076-7.

7 Gillespie, T. C., Sayegh, H. E., Brunelle, C. L. et al. Breast cancer-related lymphedema: risk factors, precautionary measures, and treatments. *Gland Surg.* 2018;(7):379-403, doi:10.21037/gs.2017.11.04.

8 Mihara, M., Hara, H., Hayashi, Y. et al. Pathological steps of cancer-related lymphedema: histological changes in the collecting lymphatic vessels after lymphadenectomy. *PLoS One.* 2012;(7):e41126-e41126, doi:10.1371/journal.pone.0041126.

9 Taghian, N. R., Miller, C. L., Jammallo, L. S. et al. Lymphedema following breast cancer treatment and impact on quality of life: A review. *Crit. Rev. Oncol. Hematol.* 2014;(92):227-234, doi:10.1016/j.critrevonc.2014.06.004.

10 Jayaraj, A., Raju, S., May, C. et al. The diagnostic unreliability of classic physical signs of lymphedema. *J. Vasc. Surg. Venous. Lymphat. Disord.* 2019;(7):890-897, doi:10.1016/j.jvsv.2019.04.013.

11 International Society of Lymphology. The diagnosis and treatment of peripheral lymphedema: 2016 consensus document of the International Society of Lymphology. *Lymphology.* 2016;(49):170-184.

12 Chang, D. W., Masia, J., Garza, R. I. I. I. et al. Lymphedema: Surgical and Medical Therapy. *Plast. Reconstr. Surg.* 2016;(138):209S-218S, doi:10.1097/PRS.0000000000002683.

13 Basta, M. N., Gao, L. L. & Wu, L. C. Operative Treatment of Peripheral Lymphedema: A Systematic Meta-Analysis of the Efficacy and Safety of Lymphovenous Microsurgery and Tissue Transplantation. *Plast. Reconstr. Surg.* 2014;(133):905-913, doi:10.1097/PRS.0000000000000010.

14 Chang, D. W., Suami, H. & Skoracki, R. A Prospective Analysis of 100 Consecutive Lymphovenous Bypass Cases for Treatment of Extremity Lymphedema. *Plast. Reconstr. Surg.* 2013;(132):1305-1314, doi:10.1097/PRS.0b013e3182a4d626.

15 Mihara, M., Hara, H., Tange, S. et al. Multisite Lymphaticovenular Bypass Using Supermicrosurgery Technique for Lymphedema Management in Lower Lymphedema Cases. *Plast. Reconstr. Surg.* 2016;(138):262-272, doi:10.1097/PRS.0000000000002254.

16 Rosian, K. & Stanak, M. Efficacy and safety assessment of lymphovenous anastomosis in patients with primary and secondary lymphoedema: A systematic review of prospective evidence. *Microsurgery.* 2019;(39):763-772, doi:10.1002/micr.30514.

17 Allen Jr., R. J. & Cheng, M.-H. Lymphedema surgery: Patient selection and an overview of surgical techniques. *J. Surg. Oncol.* 2016;(113):923-931, doi:10.1002/jso.24170.

18 Cheng, M.-H., Huang, J.-J., Wu, C.-W. et al. The Mechanism of Vascularized Lymph Node Transfer for Lymphedema: Natural Lymphaticovenous Drainage. *Plast. Reconstr. Surg.* 2014;(133).

19 Yamamoto, T., Yamamoto, N., Yoshimatsu, H. et al. Factors Associated with Lymphosclerosis: An Analysis on 962 Lymphatic Vessels. *Plast. Reconstr. Surg.* 2017;(140).

20 Desmettre, T., Devoisselle, J. M. & Mordon, S. Fluorescence Properties and Metabolic Features of Indocyanine Green (ICG) as Related to Angiography. *Surv. Ophthalmol.* 2000;(45):15-27, doi:10.1016/S0039-6257(00)00123-5.
21 Landsman, M. L., Kwant, G., Mook, G. A. et al. Light-absorbing properties, stability, and spectral stabilization of indocyanine green. *J. Appl. Physiol.* 1976;(40):575-583, doi:10.1152/jappl.1976.40.4.575.
22 Shikayama, T. in *ICG Fluorescence Imaging and Navigation Surgery* (eds Mitsuo Kusano, Norihiro Kokudo, Masakazu Toi, & Masaki Kaibori) 21-27 (Springer Japan, 2016).
23 Nguyen, A. T., Suami, H., Hanasono, M. M. et al. Long-term outcomes of the minimally invasive free vascularized omental lymphatic flap for the treatment of lymphedema. *J. Surg. Oncol.* 2017;(115):84-89, doi:10.1002/jso.24379.
24 Suami, H., Heydon-White, A., Mackie, H. et al. A new indocyanine green fluorescence lymphography protocol for identification of the lymphatic drainage pathway for patients with breast cancer-related lymphoedema. *BMC Cancer.* 2019;(19), doi:10.1186/s12885-019-6192-1.
25 Unno, N., Inuzuka, K., Suzuki, M. et al. Preliminary experience with a novel fluorescence lymphography using indocyanine green in patients with secondary lymphedema. *J. Vasc. Surg.* 2007;(45):1016-1021, doi:10.1016/j.jvs.2007.01.023.
26 Yamamoto, T., Matsuda, N., Doi, K. et al. The earliest finding of indocyanine green lymphography in asymptomatic limbs of lower extremity lymphedema patients secondary to cancer treatment: the modified dermal backflow stage and concept of subclinical lymphedema. *Plast. Reconstr. Surg.* 2011;(128):314e-321e.
27 Yamamoto, T., Narushima, M., Doi, K. et al. Characteristic indocyanine green lymphography findings in lower extremity lymphedema: the generation of a novel lymphedema severity staging system using dermal backflow patterns. *Plast. Reconstr. Surg.* 2011;(127):1979-1986.
28 Yamamoto, T., Yamamoto, N., Doi, K. et al. Indocyanine green-enhanced lymphography for upper extremity lymphedema: a novel severity staging system using dermal backflow patterns. *Plast. Reconstr. Surg.* 2011;(128):941-947.
29 Yoon, J. A., Shin, M. J. & Kim, J. H. Indocyanine green lymphography and lymphoscintigraphy severity stage showed strong correlation in lower limb lymphedema. *Lymphatic. Res. Biol.* 2021;(19):80-85, doi:10.1089/lrb.2020.0043.
30 Murawa, D., Hirche, C., Dresel, S. et al. Sentinel lymph node biopsy in breast cancer guided by indocyanine green fluorescence. *Br. J. Surg.* 2009;(96):1289-1294, doi:10.1002/bjs.6721.
31 Cornelissen, A. J. M., van Mulken, T. J. M., Graupner, C. et al. Near-infrared fluorescence image-guidance in plastic surgery: A systematic review. *Eur. J. Plast. Surg.* 2018;(41):269-278, doi:10.1007/s00238-018-1404-5.
32 Wang, L. V. Tutorial on Photoacoustic Microscopy and Computed Tomography. *IEEE J. Sel. Top. Quant. Elec.* 2008;(14):171-179, doi:10.1109/JSTQE.2007.913398.
33 Attia, A. B. E., Balasundaram, G., Moothanchery, M. et al. A review of clinical photoacoustic imaging: Current and future trends. *Photoacoustics.* 2019;(16):100144-100144, doi:10.1016/j.pacs.2019.100144.
34 Zhao, T., Desjardins, A. E., Ourselin, S. et al. Minimally invasive photoacoustic imaging: Current status and future perspectives. *Photoacoustics.* 2019;(16):100146-100146, doi:10.1016/j.pacs.2019.100146.
35 Kajita, H., Suzuki, Y., Sakuma, H. et al. Visualization of Lymphatic Vessels Using Photoacoustic Imaging. *Keio. J. Med.* 2020:1-11, doi:10.2302/kjm.2020-0010-oa.
36 Zhong, H., Duan, T., Lan, H. et al. Review of Low-Cost Photoacoustic Sensing and Imaging Based on Laser Diode and Light-Emitting Diode. *Sensors (Basel).* 2018;(18):2264, doi:10.3390/s18072264.
37 Zhu, Y., Feng, T., Cheng, Q. et al. Towards Clinical Translation of LED-Based Photoacoustic Imaging: A Review. *Sensors (Basel).* 2020;(20):2484, doi:10.3390/s20092484.
38 Zhu, Y., Xu, G., Yuan, J. et al. Light Emitting Diodes based Photoacoustic Imaging and Potential Clinical Applications. *Sci. Rep.* 2018;(8):9885-9885, doi:10.1038/s41598-018-28131-4.
39 Agano, T., Sato, N. & Awazu, K. *LED-based photoacoustic imaging system: why it achieves the same signal to noise ratio as solid-state-laser-based system: a review*. Vol. 11240 PWB (SPIE, 2020).
40 Agrawal, S., Kuniyil Ajith Singh, M., Johnstonbaugh, K. et al. Photoacoustic Imaging of Human Vasculature Using LED versus Laser Illumination: A Comparison Study on Tissue Phantoms and In Vivo Humans. *Sensors.* 2021;(21):424.

2

Imaging of the lymphatic vessels for surgical planning: a systematic review

Saskia van Heumen, Jonas J.M. Riksen, Wichor M. Bramer, Gijs van Soest, Dalibor Vasilic

The content of this chapter has been submitted as an original article and is currently under review.

(Visual) Abstract

Background: Secondary limb lymphedema is a common complication after surgical or radiotherapeutic cancer treatment. (Micro)surgical intervention such as lympho-venous bypass and vascularized lymph node transfer can be a solution in patients who are refractory to conventional treatment. Adequate imaging is needed to identify functional lymphatic vessels and nearby veins for surgical planning.

Methods: A systematic literature search was conducted in March 2021. Studies reporting on lymphatic vessel detection in healthy subjects or secondary lymphedema of the limbs or head and neck were analyzed.

Results: 106 lymphatic vessel imaging studies were included. Six imaging modalities were identified. The aim of the studies was diagnosis, severity staging and/or surgical planning.

Discussion: Due to its utility in surgical planning, near-infrared fluorescence lymphangiography (NIRF-L) has gained prominence in recent years, relative to lymphoscintigraphy, the current gold standard for diagnosis and severity staging. Magnetic resonance lymphography gives 3D detailed information on the location of both lymphatic vessels and veins and the extent of fat hypertrophy. However, MRL is less practical for routine pre-surgical implementation due to its limited availability and high cost. High frequency ultrasound imaging can provide high resolution imaging of lymphatic vessels but is highly operator dependent and accurate identification of lymphatic vessels is difficult. Finally, photoacoustic imaging is a novel technique for visualization of functional lymphatic vessels and veins. More evidence is needed to evaluate the utility of PAI in surgical planning.

Figure 2.1 shows the visual abstract of this chapter.

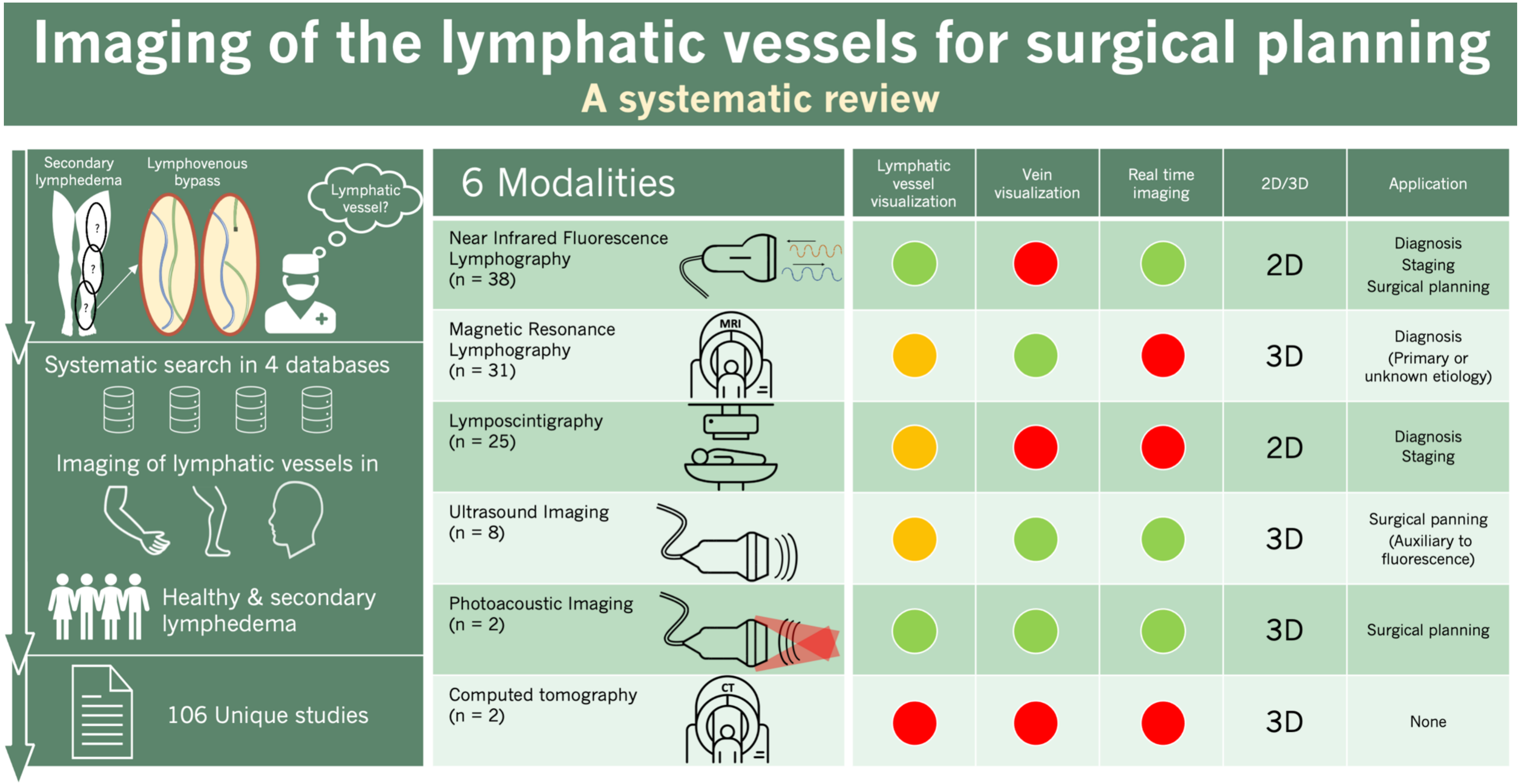

Figure 2.1: Visual abstract on imaging of the lymphatic vessels: a systematic review

2.1 Introduction

The lymphatic system fulfils several functions in the body: primarily, it drains interstitial fluid, transports lipids and proteins and is an important conduit for mediating the immune response.[1,2] Lymphedema is the accumulation of lymph fluid in the interstitium, causing swelling of the affected area.[3] Patients experience discomfort, fatigue, diminished strength and sometimes recurrent cellulitis leading to compromised functioning and in grave cases irreversible fibrosis. Not surprisingly, a severe negative impact on a person's quality of life is often reported.[4]

The cause can be either a hereditary or congenital condition (primary lymphedema) or a result from damage to the lymphatic system (secondary lymphedema). The latter is far more common than primary lymphedema and often caused by cancer treatment. Even though treatments have become less invasive over the years[5], approximately 1 in 5 breast cancer patients will develop lymphedema[6] with lymph node dissection, mastectomy and radiation therapy as risk factors.[5,7,8]

Primary diagnosis is based on the clinical presentation and the medical history of a patient. Clinical severity is often assessed with the International Society of Lymphology (ISL)[9] or Campisi Clinical scale.[10] Clinical signs are however subjective and not always accurate.[11]

Early diagnosis and therapy are essential for patient comfort and preventing loss of function.[12] Complete decongestive therapy (CDT) is deployed as the first step for conservative treatment. Lympho-venous bypass (LVB) and, in severe cases, vascularized lymph node transfers (VLNT) are (micro)surgical interventions gaining a momentum and forming an important treatment alternative.[13-15] Reductive procedures (excision or liposuction) are sometimes done in severe cases.[16] An important aspect of surgical decision making is the detection of functional, non-sclerotic[17] lymphatic vessels and the presence of a nearby suitable receiving vein.[18,19] Therefore, appropriate pre-operative imaging is of great importance to substantiate treatment choice.

This systematic review presents an overview of the existing imaging modalities used for pre-operative visualization of the lymphatic vessels in patients with secondary lymphedema of the extremities or head and neck. We describe the most important findings, advantages and disadvantages for each modality and discuss it in the perspective of surgical interventions. This means that ideally, an imaging modality detects lymphatic functionality, shows its locations in three dimensions and displays the venous network that will function as an anastomotic acceptor site.

2.2 Methods

2.2.1 Search strategy

A systematic literature was conducted in Embase.com, Medline ALL via Ovid, Web of Science Core Collection and the Cochrane CENTRAL register of Trials on 30 March 2021. The search query was developed by an experienced medical information specialist (WMB) and consisted of synonyms and thesaurus terms of 4 concepts: (1) lymphatic vessel or lymphography, (2) imaging or different imaging modalities (magnetic resonance, scintigraphy, ultrasound, photoacoustic, fluorescence) (3) lymphedema and (4) head and neck or extremities. For full details of the search queries, see Supplementary table 1. The search results of all databased were imported in EndNote and deduplicated with the method described by Bramer et al.[20]

2.2.2 Inclusion and exclusion criteria

Studies were included if they described imaging of the lymphatic vessels in healthy participants or in patients with secondary lymphedema affecting the upper or lower extremities or the head and neck. Studies including both primary and secondary lymphedema patients were also included. If a study only investigated primary lymphedema patients, it was excluded. Only studies that primarily analyzed one or more imaging modalities for visualization of the lymphatic system and specifically mentioned visualization of the lymphatic vessels were included. Therefore, studies reporting on the lymph nodes only were not included. Studies about intra- or post-surgical imaging were not included. Studies involving animals or cadavers, case reports (1 patient), reviews, conference proceedings and commentaries were also excluded. Furthermore, articles published before 2000 were excluded, because imaging modalities and devices used before this time were considered obsolete and are often not used in clinical practice anymore. Studies available in English and full text were assessed for eligibility.

2.2.3 Study selection and data extraction

Search results from all databased were collected and duplicates removed. All titles and abstract were retrieved and assessed for eligibility. Subsequently the remaining records were assessed based on full text. Eligibility was discussed between two reviewers (SvH, JR) and consensus was reached. The following information was extracted from each study: year of publication, author identification, study population, cause of lymphedema, clinical staging, contrast agent administration information (type, dose, injection site and injection type) and the imaging device used. Furthermore, outcomes regarding imaging quality of the lymphatic vessels or diagnostic performance were also extracted.

2.3 Results

2.3.1 Studies included

Literature search, after removal of duplicates and studies published before 2000, resulted in 806 records. Screening resulted in exclusion of 694 records, leaving 106 records for inclusion. Figure 2.2 gives an overview of the study inclusion process. Six different imaging modalities were identified, namely lymphoscintigraphy, near-infrared fluorescence lymphangiography (NIRF-L), computed tomography (CT), magnetic resonance lymphography (MRL), ultrasound imaging (US) and photoacoustic imaging (PAI). The included studies had different aims and methods and heterogeneous study populations. All results are therefore described narratively. Figure 2.3 gives an overview of the relative contribution of the imaging modalities and the most important subjects discussed.

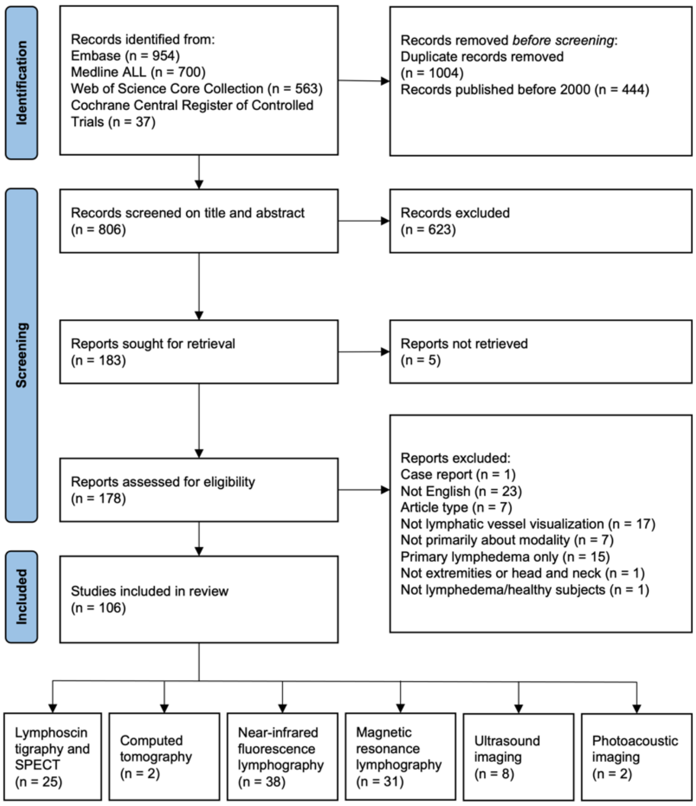

Figure 2.2: PRISMA flow diagram on study inclusion

Figure 2.3: Overview of included studies and their contribution to the lymphatic vessel imaging field. LSG: lymphoscintigraphy; US: ultrasound; PAI: photoacoustic imaging; CT: computed tomography; NIRF-L: near-infrared fluorescence lymphography; MRL: magnetic resonance lymphography; CEMRL: contrast enhanced MRL; NCMRL: non-contrast MRL; PET: positron emission tomography; SPECT: single-photon emission computed tomography

2.3.2 Lymphoscintigraphy

Out of all imaging modalities, lymphoscintigraphy has been used the longest. With a gamma camera, whole body images are obtained to get a gross overview of the lymphatic uptake of a 99m-Technetium labeled contrast agent.[21] Most studies described methods for lymphedema diagnosis and severity staging. One study reported on visualization of head and neck drainage pathways.[22] Supplementary table 2 gives an overview of the included lymphoscintigraphy studies.

Parameters for diagnosis and severity staging systems

There is an abundance of qualitative and quantitative parameters used to categorize patients into severity types. Figure 2.4 shows lymphoscintigraphy images. There was a clear agreement between studies on several factors that contribute to adequate diagnosis and staging, namely visualization of inguinal or axillary lymph nodes, the lymphatic vessels (normal, dilated or collaterals), lymphatic fluid leakage into the subcutaneous tissue (i.e., dermal backflow (DBF)) and uptake in popliteal or antecubital lymph nodes. Studies typically evaluated different factors, with variable weighting.

Quantitative scintigraphy parameters reflect the overall functionality of the lymphatics and were primarily derived from the arrival time in the proximal lymph nodes (transit time; TT, or tracer appearance time; TAT)[23-28] or clearance rate from the injection site (Depot Disappearance Rate Constant) and the subsequent uptake in the blood.[29-33]

The severity of lymphedema was graded based (a selection of) the above mentioned characteristics and differentiated patients into 4[25,34], 5[28,35,36] or 6 (Taiwan Lymphoscintigraphy Staging, TLS)[37,38] different stages. Lymphoscintigraphy findings have been combined with clinical symptoms and circumference measurements in Cheng's Lymphedema Grade (CLG) system and earlier scales.[37-39] Lastly, the transport index (TI[40]) is a scoring of several subjective observations indicating either normal or abnormal lymphatics. Correlations between clinical parameters and lymphoscintigraphy staging systems have been reported[35-38,41], but were not always significant.[35,36]

Diagnostic performance

Evaluation of both qualitative and quantitative parameters was highly reproducible[32], but the diagnostic performance differed. High sensitivities (92.3-96%) and specificities (92.9-100%) of lymphedema diagnosis based on only qualitative parameters were reported.[27,42] On the other hand, a lower sensitivity and specificity of 51% and 89% based solely on quantitative parameters were found. Combining quantitative findings with qualitative findings caused a moderate increase of the sensitivity, while specificity remained the same.[23] For this reason, diagnosis based on quantitative parameters only is ambiguous. Qualitative and quantitative scintigraphy parameters correlated variably with limb circumference differences.[26,43] It was even proposed that lymphoscintigraphy does not give additional information beyond abnormal or normal lymphatics.[26]

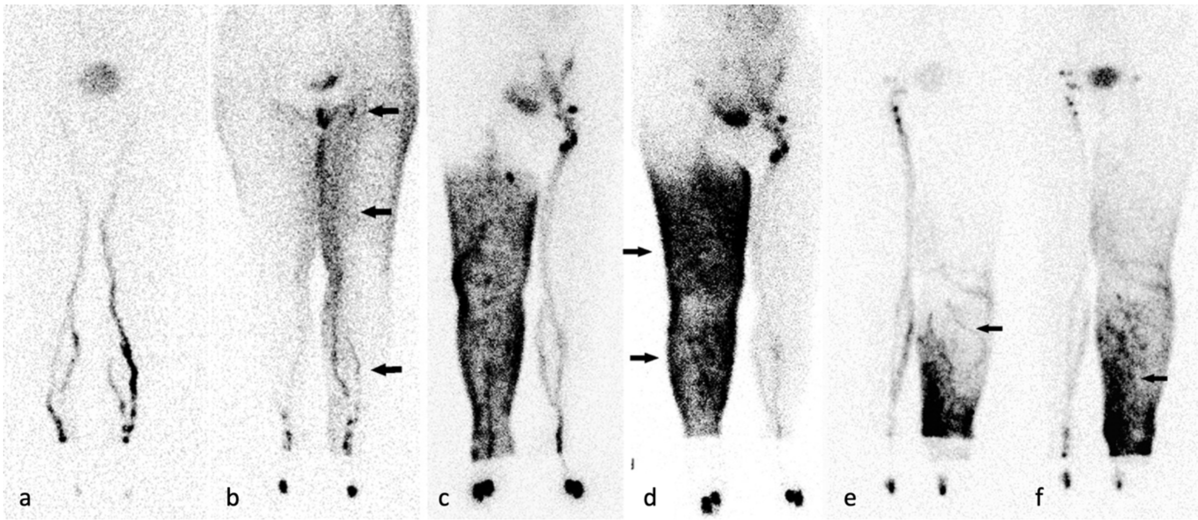

Figure 2.4: Lymphoscintigraphy imaging of the lymphatics. (a, b) Images of type II in a patient with left lymphedema 30 (a) and 120 minutes (b) after injection of contrast medium. Lymph stasis in the lymphatics (arrow) and visible dermal backflow (arrow) on the left thigh can be seen. The inguinal lymph nodes are reduced in number (arrow). (c, d) Images of type III in a patient with right lymphedema 30 (c) and 120 (d) minutes after injection of contrast medium. Dermal backflow (arrows) in the leg and thigh can be seen. (e, f) Images of type IV in a patient with left lymphedema 30 (e) and 120 (f) minutes after injection of contrast medium. Dermal backflow (arrow in e) and lymph stasis in the lymph vessels (arrow in f) in the leg can be seen and remains in the leg 120 minutes later. Reprinted from Microsurgery, Ref [35], with permission from John Wiley & Sons, Inc.

Treatment decision making and surgical planning

Different treatment regimens based on a patient's lymphoscintigraphy stage were proposed.[25,36-38,41] Overall, CDT was indicated in less severe cases, LVB in patients with partially obstructed lymphatics with some patent lymphatic vessels[36] and VLNT for patients sometimes combined with debulking surgery with severely obstructed lymphatics.[37,38] However, LVB surgery has been performed in almost all stages[35,36], with better results in the partially obstructed patients. Differentiation between deep and superficial vessels may also be beneficial for treating multiple levels of the lymphatic system.[41] Other methods were used for intraoperative vessel identification after lymphoscintigraphy based diagnosis[35,36], because lymphoscintigraphy was not sufficient for precise selection of the anastomosis site.

Two studies investigated the predictive value of qualitative lymphoscintigraphy findings and treatment success. No clear relation between lymph vessel visualization and CDT treatment success was found.[33] However, visible dilated lymph vessels and the presence of DBF was significantly related to better LVB surgery outcomes.[44]

Injection and imaging protocols

Contrast agents were generally injected subcutaneously, but intradermal injections were also used (Supplementary table 3). Findings pointed towards better image quality of the superficial lymphatics and therefore assessment of lymphatic vessels with intradermal injections. Subsequently, a more rapid uptake of the radiotracer was observed, allowing for shorter imaging durations.[24,28,30,31] Subfascial tracer injection was not suitable for lymphatic vessel visualization.[29,41]

Imaging protocols (stress versus rest protocols) differed substantially. The increase in muscle activity in stress-based protocols may facilitate tracer uptake in the lymphatics, which increases the likelihood of successful visualization.[28] These protocols may therefore distinguish whether compensatory mechanisms involve the deep or superficial system, which can affect treatment choice.[24]

Single photon emission computed tomography

Single photon emission computed tomography (SPECT) combined with CT imaging has widely been used for identification of sentinel lymph nodes, but the application for visualizing lymphatic vessels is limited. In contrast to scintigraphy, SPECT-CT could provide three-dimensional and depth information.[45]. SPECT-CT also gave additional information about lymphostasis in patients with early lymphedema, while this was detected less often with planar scintigraphy. SPECT-CT mostly confirmed and better localized findings from planar scintigraphy and soft tissue changes could be assessed.[46,47]

2.3.3 Computed tomography

One study investigated Iopamidol contrast enhanced CT imaging for lymphatic vessels with the potential benefit of three-dimensional information, relatively high resolution and short imaging time.[48] In terms of resolution, CT was better than lymphoscintigraphy but worse than NIRF-L. Lymphatic vessels were hardly visible above the knee and classification of lymphedema severity based on DBF was not possible.[48] Moreover, additional information such as presence of fibrosis or fluid retention in the subcutaneous fat layer was not suitable for accurate diagnosis. The diagnostic sensitivity of CT (33%) was inferior to those of NIRF-L (100%), lymphoscintigraphy (66%) or MRI (100%).[49]

2.3.4 Near-Infrared Fluorescence Lymphangiography

NIRF-L uses the fluorescence properties of indocyanine green (ICG)[50] for real-time visualization of the lymphatic vessels. It is applied for identifying normal and altered drainage pathways[51-56] and gives information about vessel functionality by visualizing pulsatile behavior.[55] It also provides more insight into anatomical variations between patients and the possible relation between the development of lymphedema after cancer treatment and the formation of accessory pathways.[55,57-59] Supplementary table 4 gives an overview of the included NIRF-L studies.

Parameters for diagnosis and severity staging systems

Diagnosis and severity staging were most often based on either the MD Anderson Cancer Center (MDACC) scale[55,60-63] or the dermal backflow scale (DBS).[57,62,64-73] The MDACC scale focusses on the visualization of patent lymphatic vessels in combination with the presence of DBF. In contrast, the DBS focusses on the proximal to distal extension of different DBF patterns[64,68,71] (in order of severity: normal, splash, stardust and diffuse, see Figure 2.5). The more distal the pattern, the higher the severity. Both scales have been validated and are reproducible. The DBS however tends to systematically overestimate severity in the early stages of lymphedema.[62]

The DBS is based on the hypothesis that DBF in secondary limb lymphedema starts proximally and extends distally with lymphedema severity. However, there have been cases where DBF seemed to originate distally, suggesting the presence of latent primary hypoplasia, where symptoms were triggered by lymph node dissection.[74]

Both systems look at each limb separately. An approach where laterality (i.e., unilateral or bilateral lymphedema) is taken into account, has also been proposed for lower limb lymphedema.[75] Lastly, a quantitative approach has also been used where the lower extremity is divided into ten consecutive areas and the most proximal anatomical area the ICG dye reaches after a set amount of time is determined.[76,77]

Multiple studies also looked at the relationship between clinical severity and NIRF-L patterns. The DBS had a significant positive correlation with the Campisi clinical scale and the duration of lymphedema and indicates which treatment option is appropriate.[64,71] However, very weak correlations between the MDACC scale and the ISL clinical scale were reported, suggesting that both clinical and NIRF-L assessments are needed for surgical decision making.[60,62]

Circumference differences on multiple sites of the arm, especially the forearm, can also be indicative for abnormal DBF patterns.[66,78] In addition, a lack of increased water content or pitting edema was related to the absence of DBF.[66] On the other hand, correlations between NIRF-L stages and volumetric limb differences were absent[60] or weak[62] in other studies.

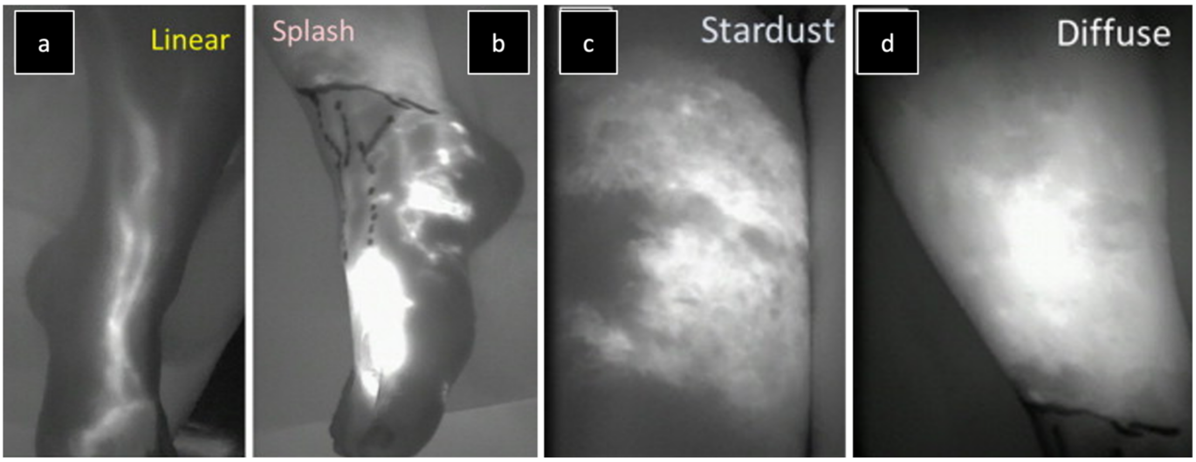

Figure 2.5: Near-infrared fluorescence lymphography images. The images represent normal and abnormal lymphatic drainage patterns in order of severity (left is normal and right is the most severe dermal backflow pattern). Reprinted from Journal of Vascular Surgery: Venous and Lymphatic Disorders, Ref [79], with permission from Elsevier.

Early diagnosis

NIRF-L can also be used for regular follow-up after cancer surgery. Detection of early abnormal flow is indicative of subclinical lymphedema and is a key point for early intervention, which might mitigate deterioration of lymphatic flow.[68] Advanced DBF patterns have been related to longer lymphedema duration, higher age and longer time until lymphedema diagnosis, suggesting that early detection is of imminent importance.[62] Abnormal patterns can even be detected before clinical symptoms are present.[57,69] One study reported increased flow in early-stage patients compared to higher stage and control subjects, which might be useful for effective drainage after LVB surgery.[76]

Quantitative parameters

In studies investigating quantitative parameters related to lymphatic pump function, similar quantitative parameters to scintigraphy were obtained, such as the TT. Significant correlations between the NIRF-L and scintigraphy values were reported.[80] There also was a correlation between increase in TT and NIRF-L staging systems.[67,70] Furthermore, the lymph flow velocity and the number of contractions/minute have been obtained using different methods[51,67,70,81-83] (numerical values are included in Supplementary table 6). Some studies found a significant decrease in flow velocity with the increase of disease severity[67,70], while others reported high variability and poor repeatability of the values and no significant correlation between disease severity and flow velocity.[51,83] This renders clinical decision making based on quantitative parameters difficult. Moreover, both velocity and contractility were influenced by increased temperature and exercise, indicating the need for uniform methodology.[81,83]

Surgical planning

Most studies suggested that NIRF-L is useful surgical planning but DBF might mask some lymphatic vessels. However potential functional lymphatic vessels might be masked by DBF. Predictive lymphatic mapping was proposed as a potential solution in these cases, which is based on the assumption that the lymphatic anatomy is symmetrical between limbs. Relative distances between lymphatic vessels and pre-defined anatomic landmarks from the healthy limb were mapped to the affected limb to identify potential anastomosis locations, with success.[84,85]

Comparison with lymphoscintigraphy

Significant correlation between NIRF-L and lymphoscintigraphy staging systems have been reported.[61,63,86] DBF patterns were consistent between the techniques, but NIRF-L allowed for more precise demarcation of lymphatic vessels.[55] The overall sensitivity was higher for NIRF-L (89%) compared to lymphoscintigraphy (45%) with as slightly lower specificity (NIRF-L: 90%; lymphoscintigraphy: 100%).[79] NIRF-L also is superior to lymphoscintigraphy for early lymphedema diagnosis with a sensitivity and specificity of 76% and 80% for NIRF-L and 11% and 0% for lymphoscintigraphy.[79,86]

Injection and imaging protocols

Generally, ICG was injected in the interdigital spaces (Supplementary table 5). However, some studies investigated the advantages of multi-lymphosome injections.[65,72,73] Multiple ICG injections are possible due to the low risk, limited toxicity and absence of radiation exposure concerns. The added value of multi-lymphosome injection lies within the pre-operative selection for LVB sites, yielding significantly better postoperative results because more functional lymphatic vessels were detected.[72] Functional vessels were more often seen around linear, splash and stardust patterns.[65] Vessel detection in the most severe lymphedema cases was also feasible. One injection is sufficient for DBF evaluation.[73]

2.3.5 Magnetic Resonance Lymphography

MRL provides high-resolution imaging of large body surface areas. It facilitates in choosing the appropriate surgical or conservative treatment is also used during follow-up for the evaluation of outcome after therapy.[87] Supplementary table 7 gives an overview of the MRL study characteristics.

Because of the versatility of MRI, multiple sequences were deployed to assess different lymphedema properties. Heavily T2-weighted images were acquired before contrast agent injection to assess soft tissue changes and fluid accumulation in the subcutaneous tissue.[87-99]

Subsequently, T1-weighted sequences with fat suppression were used to visualize the contrast agent uptake in the lymphatic vessels. Maximum intensity projections from any arbitrary plane were obtained for image assessment (see Figure 2.6 for MRL images). Supplementary table 8 shows the imaging protocol information of the MRL studies.

Contrast enhanced MRL – parameters for diagnosis

Contrast enhanced MRL (CEMRL) uses intracutaneous injection of a gadolinium-based contrast agent and makes visualization of lymphatic vessels[89-91,93,96], lymphatic collaterals, dermal backflow and lymphorrhea possible.[89-91,93,95,96,100,101] Higher resolution, better fat suppression and signal to noise ratio for the lymphatic vessels can be obtained with higher field strengths.[99]

Gadolinium based contrast agents are not specifically lymphotropic and therefore simultaneously enhance the lymphatic vessels and veins.[97,99] Studies distinguished these by their morphological or contrast agent uptake and clearance differences. Affected vessels had a beaded and tortuous appearance in contrast to the smooth blood vessels.[87,89-91,93,95,96,102] Moreover, blood had a significantly faster uptake and clearance rate leading to earlier enhancement and faster decreases of image intensity compared to lymphatic vessels.[91,96,102,103] Lymphatic vessels in the lymphedematous limb also tended to have an increased diameter compared to healthy ones but were smaller than the subcutaneous veins. Morphological features of the lymphatic vessels identified with MRL also correlated significantly with immunohistological findings of the corresponding vessels.[102,104] However, it was not always possible to differentiate lymphatic vessels based on their morphological features[89] and there was a low agreement on judgement of the level of venous contamination between different observers.[92] Enhancement kinetics was especially important in these cases.[102] Subcutaneous injection can even lead to solely venous enhancement, rendering lymphedema diagnosis impossible.[88,99] Dual-agent relaxation (DARC) MRL uses intravenous administration of ferumoxytol prior to imaging to null the venous signal and eliminated venous enhancement in the vast majority of cases.[92] However, the downside of this technique is subsequent signal suppression in the lymphatic channels as well, leading to a decreased contrast to noise ratio.

The T1-weighted MRL sequences also suffer from T2* susceptibility artifacts in locations of high gadolinium concentrations such as the injection sites but are minimal outside the injection sites.[90,91,99,103] Using Fast spin echo (FSE) instead of gradient-recalled echo (GRE) sequences can also reduce vulnerability to susceptibility artefacts and field inhomogeneities.[105]

Lymphatic vessel diameter and diagnosis

Correlations between MRL findings and the clinical severity in secondary lower limb lymphedema have been reported. The number of visualized lymphatic vessels in the calf and their diameter was indicative of the clinical severity. This was not the case for the lymphatic vessels in the thigh.[106] However, lymphatic vessel diameters in the calf and thigh were significantly higher in the affected limb compared to the healthy limb.[102,106,107] Multiple studies failed to visualize healthy lymphatic vessels, because of their small diameter and reported that only dilated lymph vessels could be clearly depicted on the images.[87,95,102,107,108] Vessels were also more easily depicted in the lower leg compared to the thigh.[89,91,96]

Comparison with NIRF-L

Multiple studies showed the potential of MRL in surgical planning in comparison to NIRF-L. MRL was a reliable tool for identifying potential anastomosis locations with a sensitivity and specificity of 90% and 100%. In some cases, the treatment plan was altered (e.g., additional liposuction) due to findings (e.g. fat hypertrophy), not detected with NIRF-L.[98] More lymphatic vessels were detected with MRL, probably because MRL can also visualize deeper vessels and does not suffer from DBF coverage making it more sensitive for lymphatic vessel detection.[109,110] However, only 57.1% of the anastomosis sites located solely with MRL were successful. This percentage was substantially higher when lymphatic vessels were identified with both NIRF-L and MRL, namely 91.4%.[109] Lastly, MRL can visualize communicating lymphatic perforators between the deep and superficial lymphatics[111] and collateral pathways[101], which might influence surgical planning.

Comparison with lymphoscintigraphy

Multiple studies investigated the differences between MRL and lymphoscintigraphy. MRL was better at depicting lymphatic vessels due to the substantially better resolution and the ability to look past dermal backflow.[88,97] In line with these results, very poor correlation was reported for lymph vessels depiction between these techniques, while excellent correlation was found for observation of drainage delay and drainage patterns.[88,97] MRL seemed less suitable for abnormal lymph node detection.[97] Lastly, MRL was inferior to scintigraphy as a diagnostic method based on DBF visualization.[94]

Non-contrast MRL – parameters for diagnosis

Non-contrast magnetic resonance lymphangiography (NCMRL) uses T2-weighted sequences to visualize slow-moving fluid combined with suppression of signal from other tissues. Multiple studies used changes of the dermis and subcutaneous tissue such as presence of a honeycomb pattern, dermal thickening and reduction of muscular trophism for diagnosis and severity assessment.[112-114] Visualization of the lymphatic vessels was unsuccessful or played a minimal role in NCMRL assessment of lymphedema.[113,115] In some studies dilated lymphatic vessels were detected in the affected limb[114] and indeed the presence of dilated vessels was related to clinical severity.[112] However, lymphatic vessel detection was limited due to the relatively low resolution of NCMRL.[112,114]

PET/MR

Two studies reported on combined positron emission tomography-MR (PET-MR) combined imaging for lymphedema diagnosis and surgical planning. Subcutaneous injection of ^{68}Ga-NOTA-Evans Blue (NEB) allows for visualization of the lymphatic vessels with relatively fast uptake speeds. Both studies reported that combined PET and MR assessment allows for both quantitative (standard uptake value, tracer transport delays) and qualitative assessment of the lymphedema severity in three dimensions (dermal backflow, subcutaneous layer thickness)[116,117] as well as its potential for surgical planning.[116]

Figure 2.6: (a) Coronal T2-weighted 2D-TSE image with fat suppression shows an extensive reticular pattern of dilated lymphatic vessels indicating neovascularization due to obstruction in the right lower leg (arrowheads). (b) Frontal 3D heavy T2-weighted MIP image demonstrates the same changes in the right lower leg (arrowheads). (c) Frontal 3D spoiled gradient-echo T1-weighted MRL MIP image obtained 35min after Gd-BOPTA injection.Two slightly enlarged lymphatic vessels are visualized in the affected right lower leg (small arrows). The concomitantly enhanced veins (large arrows) show lower signal intensity. Furthermore, areas of accumulated lymph fluid are detected in three modalities image (asterisk). No lymphedema is seen in the left lower leg. Reprinted from European Journal of Radiology, Ref [118]*, with permission from Elsevier.*

2.3.6 Ultrasound

High frequency ultrasound devices facilitate detailed real-time visualization of lymphatic vessels and veins. Conventional high frequencies (CHFUS) between 15 and 24 MHz[119-124] and/or ultra-high frequencies (UHFUS) of 48 and 70 MHz was used.[125,126] Supplementary table 9 gives an overview of the study characteristics.

Parameters for lymphatic vessel detection, diagnosis and severity staging

Lymphatic vessels were detected based on their appearance on the ultrasound image and identified after a process of eliminating veins and nerves. Differentiation of lymphatic vessels from other structures was based on shape[119-121,123,125,126], echogenic texture[119-121,123,125,126], Doppler colour[119-121,123-126], collapsibility[120,124-126], convergence[124-126] and location[124]. The findings of the first four criteria differed depending on the severity of sclerosis.[120,125]

Lymphatic vessels were also classified into different types based on the degree of degradation. Namely normal, ectasis, contraction or sclerosis type[120] or type I (normal + ectasis) and type II (contraction + sclerosis).[126] The goal of differentiating between these types was optimal vessel selection for LVB surgery (i.e., ectasis type vessels)[120] or diagnosis.[124] Vessels with a dilated lumen (ectasis type) or the presence of sclerosis (contraction and sclerosis type) were diagnosed as lymphedema with a sensitivity, specificity and accuracy of 95.0%, 100% and 94.6% respectively.[124] Figure 2.7 shows example ultrasound images.

Lymphatic vessel detection performance

The majority of the studies reported on vessel detection performance with different gold standards (Supplementary table 10). Overall, sensitivities ranged from 66.3-95.5% for lymphatic vessel detection were reported[119-121,125], with higher sensitivities for ectasis (82.9%), contraction (85.7%) and sclerosis (85.7%) type vessels in contrast to normal type (66.7%) vessels.[120] Overall detection sensitivity was also higher with UHFUS (94.9%) compared to CHFUS (66.3%).[125] However, the accuracy of the vessel classification was below 50% for normal, contraction and sclerosis type vessels and was 62.9% for ectasis type vessels. Specificities ranged between 91.3% and 100%, with a higher specificity for UHFUS (98.8%) compared to CHFUS (91.3%).[125] Sometimes more suitable lymphatic vessels for anastomosis were detected with ultrasound compared to NIRF-L.[123,124]

Vessel diameter and depth

Lymphatic vessel diameters were mostly reported in the leg ranging from 0.417 to 1.15 mm. Lymphatic vessels of the arm were smaller.[125] Changing body position from supine to sitting or standing also caused a decrease in diameter.[122] Vessel diameters found with CHFUS were significantly larger than with UHFUS.[125] Moreover, larger vessels were detected with ultrasound compared to NIRF-L. Post-surgery circumference reduction was significantly higher in this group.[121] Lastly, vessel measurements significantly correlated between ultrasound and histology measurements.[126]

The maximum depth of lymphatic vessels found depended on the location[121,123] and frequency used.[125] Lymphatic vessels run more deeply in the upper arm and thigh were more difficult to visualize, especially with UHFUS. Lower frequencies (CHFUS) are therefore recommended for visualization of deeper vessels.[126]

2.3.7 Photoacoustic imaging

Photoacoustic imaging (PAI) is a new modality not yet used in clinical practice. It also uses ICG but depends on its optical absorption (not fluorescence) properties. Light of specific wavelength is absorbed by chromophores such as melanin, hemoglobin or ICG causing thermoelastic expansion, generating acoustic waves detected with an ultrasound transducer. Studies showed that three-dimensional high resolution imaging and differentiation of lymphatic and blood vessels is possible along with DBF characterisation.[127,128] Lastly, more lymphatic vessels were identified using PAI compared to NIRF-L and PAI seemed to be less affected by thicker subcutaneous tissue.[128] Figure 2.8 shows example PAI images.

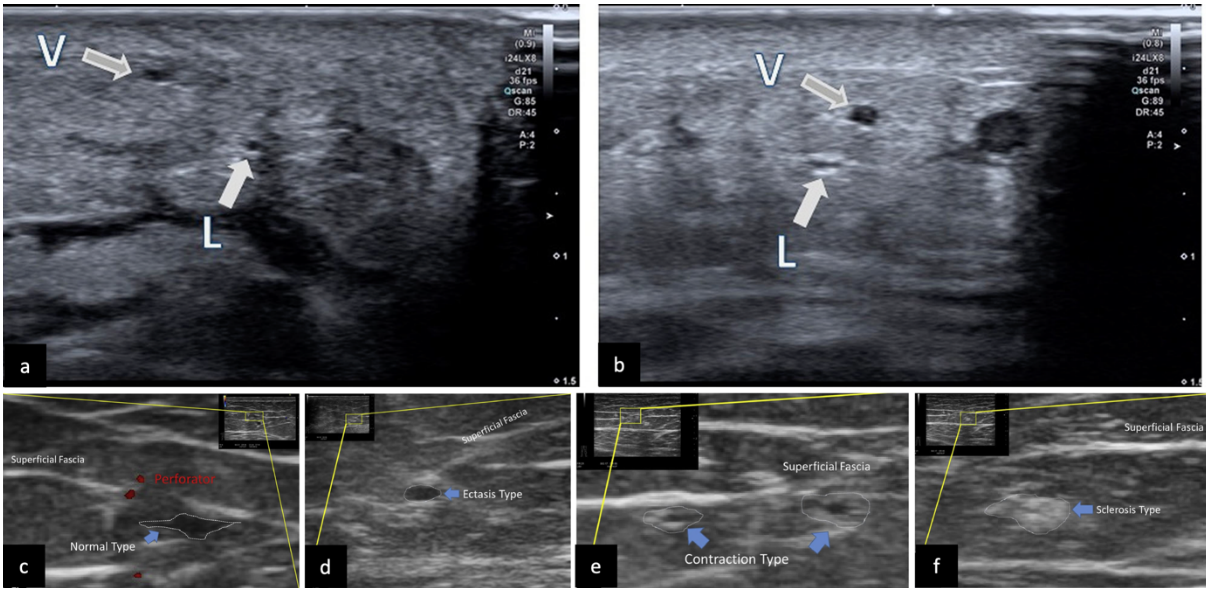

Figure 2.7: (a, b) Ultrasonographic images of veins (V) and lymphatic vessels (L). Reprinted from Journal of Surgical Oncology, Ref [123]*, with permission from John Wiley & Sons, Inc. (c, d, e, f) Ultrasonographic images of different lymphatic vessel types according to the NECST classification. Reprinted from Journal or Plastic, Reconstructive & Aesthetic Surgery, Ref* [120]*, with permission from Elsevier.*

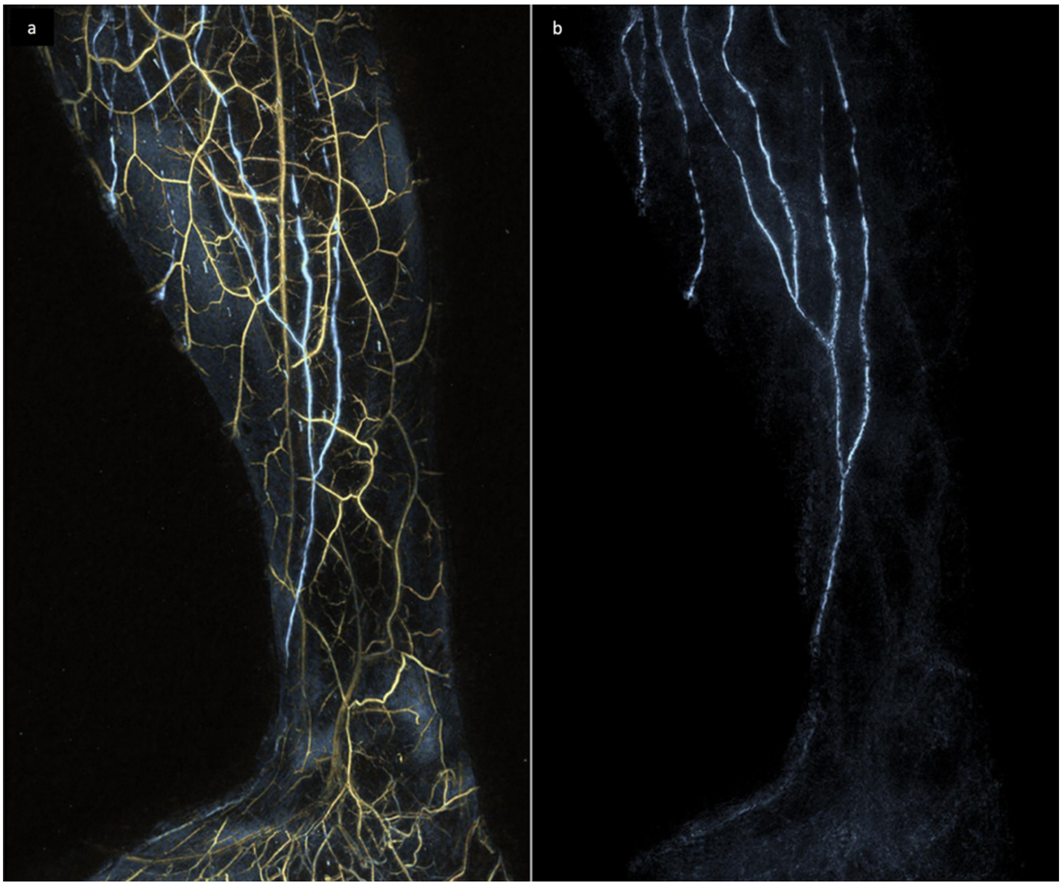

Figure 2.8: Photoacoustic images. The medial-side view of the photoacoustic lymphangiography of the right lower leg of a woman in her thirties without any past medical history. (a) Lymphatic vessels are shown in blue and venules are shown in yellow. (b) Only lymphatic vessels are shown. Reprinted from Journal of Surgical Oncology, Ref [127]*, with permission from John Wiley & Sons, Inc.*

2.4 Discussion

(Super)microsurgical treatment planning of lymphedema critically depends on the imaging technique. The ideal imaging modality can detect functional lymphatic vessels, shows their location in three dimensions and displays the venous network. With this systematic review we provide an overview of the existing imaging modalities used for pre-operative visualization of the lymphatic vessels.

A wide variety of imaging modalities are available for lymphedema diagnosis, severity staging and surgical planning. NIRF-L is superior to lymphoscintigraphy in lymphatic vessel depiction for surgical planning. Lymphoscintigraphy provides 2D visualization in a large field of view, but the wide variety in imaging protocols suggest that there is no consensus on the optimal method.[129] The main disadvantage is the low resolution, which makes clear depiction of lymphatic vessels and therefore precisely locating anastomosis sites unreliable.[25,36-38,41] Other disadvantages are the lack of depth information and the long acquisition duration. SPECT-CT could offer a significant advantage for 3D localization but remains understudied and is not routinely used in practice. Lymphoscintigraphy and SPECT-CT impose radiation exposure, while NIRF-L is not associated with ionizing radiation and ICG has an excellent safety profile.[50] Moreover, NIRF-L has superior image resolution, provides real time imaging of lymphatic vessels and vessel contractions.[52,55] Imaging assessment methods also are more uniform and suitable for (early) diagnosis.[57,62,68,69] The downside of NIRF is the absence of depth information on lymphatic vessels and the limited depth penetration (~1-2 cm).[130,131] The appearance of lymphatic vessels changes due to optical scattering and saturation of the camera for superficially pooled ICG, possibly masking deeper targets.[63,71] Lastly, visualization of the acceptor veins is not possible.

MRL provides 3D high-resolution simultaneous lymphatic vessel and vein enhancement, which has the advantage that LVB sites can be selected but it can also lead to misidentification and thus inaccurate surgical planning.[89,92] Moreover, non-dilated vessels are often not visible, limiting early diagnosis based on MRL findings.[87,95,108,132] MRL also is less practical for routine implementation in secondary lymphedema due to the limited availability and high costs, which leads to logistical challenges to do surgical planning with up-to-date images and makes regular follow-up with MRL unrealistic. When a more detailed overview of the entire lymphatic system is needed such as in primary lymphedema cases, MRL is indicated.[133-135]

Contrarily, clinical implementation of HFUS is less tedious due to its portability. HFUS also is complemented by the ability to make accurate diameter measurements. Additionally, the technique is label-free and is not influenced by DBF.[119,121,126] The major downside is the high operator dependency and the demanding learning curve. Implementation of this technique is therefore not straightforward.[119,121,123,125]

Finally, the properties of PAI make simultaneous visualization and differentiation of the lymphatic vessels and veins with a high 3D spatial and temporal resolution possible.[136] This might overcome problems with misidentification of structures and the lack of depth information. PAI thus fulfills many of the criteria for an ideal imaging modality for surgical planning. The downside of the photoacoustic devices in the current studies is the large size of the imaging system and the use of high-power lasers. Portable and LED-based systems have been developed, making clinical implementation safer and easier[137,138], although the lower optical power limits penetration depth to about 1 cm.

Clinical use of the acquired images pivots on the definition of disease scales, which rely on counting or scoring of image parameters. A common aspect of all modalities included here, is that interpretation, annotation and measurement of the images by a human expert is critical. This manual process is time consuming and prone to individual variability, undermining the robustness of scoring systems. Another limitation that is shared between all imaging techniques except ultrasound is the use of exogenous contrast, which must be injected prior to imaging.

This systematic review has some limitations. Due to the wide scope of this review, a heterogeneous group of studies and study populations was included. Very few articles directly compared imaging modalities quantitatively but mostly describe their findings narratively. However, the emphasis of this review was to highlight the imaging techniques and their applications. Secondly, the search term was truncated to only find studies limited to imaging of the extremities or head and neck region. Relevant studies may have been missed if they did not mention one of these terms in their keywords, title or abstract. Lastly, systematic reviews are subject to publication and selection bias, as studies with negative or undesirable results might not be published. We expect that our systematic approach minimized this bias.

2.5 Conclusion

We reviewed six imaging techniques for mapping secondary lymphedema. A wide variety of modality-specific parameters and staging systems is in use. NIRF-L has gained popularity in recent years, in comparison to lymphoscintigraphy due to its superior image quality and ease of use. It can be usefully compounded with high frequency ultrasound, which also characterizes vessel condition. MRL has been intensely researched for its 3D imaging capability but exhibits limited sensitivity for small structures and remains expensive. Lastly, PAI is a novel technique that capitalizes on a combination of optical and acoustic contrast, visualizing both lymphatic vessels and veins in 3D. More evidence is needed to evaluate the utility of PAI in surgical planning.

References

1 Scallan, J. P., Zawieja, S. D., Castorena-Gonzalez, J. A. et al. Lymphatic pumping: mechanics, mechanisms and malfunction. *J. Physiol.* 2016;(594):5749-5768, doi:10.1113/JP272088.

2 Randolph, G. J., Ivanov, S., Zinselmeyer, B. H. et al. The Lymphatic System: Integral Roles in Immunity. *Annu. Rev. Immunol.* 2017;(35):31-52, doi:10.1146/annurev-immunol-041015-055354.

3 Swartz, M. A. The physiology of the lymphatic system. *Adv. Drug Deliv. Rev.* 2001;(50):3-20, doi:10.1016/S0169-409X(01)00150-8.

4 Taghian, N. R., Miller, C. L., Jammallo, L. S. et al. Lymphedema following breast cancer treatment and impact on quality of life: A review. *Crit. Rev. Oncol. Hematol.* 2014;(92):227-234, doi:10.1016/j.critrevonc.2014.06.004.

5 Gillespie, T. C., Sayegh, H. E., Brunelle, C. L. et al. Breast cancer-related lymphedema: risk factors, precautionary measures, and treatments. *Gland Surg.* 2018;(7):379-403, doi:10.21037/gs.2017.11.04.

6 DiSipio, T., Rye, S., Newman, B. et al. Incidence of unilateral arm lymphoedema after breast cancer: a systematic review and meta-analysis. *Lancet. Oncol.* 2013;(14):500-515, doi:10.1016/S1470-2045(13)70076-7.

7 Erickson, V. S., Pearson, M. L., Ganz, P. A. et al. Arm Edema in Breast Cancer Patients. *J. Natl. Cancer. Inst.* 2001;(93):96-111, doi:10.1093/jnci/93.2.96.

8 Cormier, J. N., Askew, R. L., Mungovan, K. S. et al. Lymphedema beyond breast cancer. *Cancer.* 2010;(116):5138-5149, doi:10.1002/cncr.25458.

9 International Society of Lymphology. The diagnosis and treatment of peripheral lymphedema: 2016 consensus document of the International Society of Lymphology. *Lymphology.* 2016;(49):170-184.

10 Campisi, C. & Boccardo, F. Microsurgical Techniques for Lymphedema Treatment: Derivative Lymphatic-Venous Microsurgery. *World J. Surg.* 2004;(28):609-613, doi:10.1007/s00268-004-7252-4.

11 Jayaraj, A., Raju, S., May, C. et al. The diagnostic unreliability of classic physical signs of lymphedema. *J. Vasc. Surg. Venous. Lymphat. Disord.* 2019;(7):890-897, doi:10.1016/j.jvsv.2019.04.013.

12 Mihara, M., Hara, H., Hayashi, Y. et al. Pathological steps of cancer-related lymphedema: histological changes in the collecting lymphatic vessels after lymphadenectomy. *PLoS One.* 2012;(7):e41126-e41126, doi:10.1371/journal.pone.0041126.

13 Chang, D. W., Suami, H. & Skoracki, R. A Prospective Analysis of 100 Consecutive Lymphovenous Bypass Cases for Treatment of Extremity Lymphedema. *Plast. Reconstr. Surg.* 2013;(132):1305-1314, doi:10.1097/PRS.0b013e3182a4d626.

14 Basta, M. N., Gao, L. L. & Wu, L. C. Operative Treatment of Peripheral Lymphedema: A Systematic Meta-Analysis of the Efficacy and Safety of Lymphovenous Microsurgery and Tissue Transplantation. *Plast. Reconstr. Surg.* 2014;(133):905-913, doi:10.1097/PRS.0000000000000010.

15 Chang, D. W., Masia, J., Garza, R. I. I. I. et al. Lymphedema: Surgical and Medical Therapy. *Plast. Reconstr. Surg.* 2016;(138):209S-218S, doi:10.1097/PRS.0000000000002683.

16 Allen Jr., R. J. & Cheng, M.-H. Lymphedema surgery: Patient selection and an overview of surgical techniques. *J. Surg. Oncol.* 2016;(113):923-931, doi:10.1002/jso.24170.

17 Mihara, M., Hara, H., Tange, S. et al. Multisite Lymphaticovenular Bypass Using Supermicrosurgery Technique for Lymphedema Management in Lower Lymphedema Cases. *Plast. Reconstr. Surg.* 2016;(138):262-272, doi:10.1097/PRS.0000000000002254.

18 Yamamoto, T., Narushima, M., Yoshimatsu, H. et al. Minimally invasive lymphatic supermicrosurgery (MILS): indocyanine green lymphography-guided simultaneous multisite lymphaticovenular anastomoses via millimeter skin incisions. *Ann. Plast. Surg.* 2014;(72):67-70, doi:10.1097/SAP.0b013e3182605580.

19 Yang, J. C., Wu, S. C., Chiang, M. H. et al. Intraoperative identification and definition of "functional" lymphatic collecting vessels for supermicrosurgical lymphatico-venous anastomosis in treating lymphedema patients. *J. Surg. Oncol.* 2018;(117):994-1000, doi:10.1002/jso.25014.

20 Bramer, W. M., Giustini, D., de Jonge, G. B. et al. De-duplication of database search results for systematic reviews in EndNote. *J. Med. Libr. Assoc. : JMLA.* 2016;(104):240-243, doi:10.3163/1536-5050.104.3.014.

21 Williams, W. H., Witte, C. L., Witte, M. H. et al. Radionuclide lymphangioscintigraphy in the evaluation of peripheral lymphedema. *Clin. Nucl. Med.* 2000;(25):451-464, doi:10.1097/00003072-200006000-00013.

22 Bourgeois, P., Peters, E., Van Mieghem, A. et al. Edemas of the face and lymphoscintigraphic examination. *Sci. rep.* 2021;(11):6444.

23 Dabrowski, J., Merkert, R. & Kuśmierek, J. Optimized lymphoscintigraphy and diagnostics of lymphatic oedema of the lower extremities. *Nucl. Med. Rev.* 2008;(11):26-29.

24 Tartaglione, G., Pagan, M., Morese, R. et al. Intradermal lymphoscintigraphy at rest and after exercise: A new technique for the functional assessment of the lymphatic system in patients with lymphoedema. *Nucl. Med. Commun.* 2010;(31):547-551, doi:10.1097/MNM.0b013e328338277d.

25 Kalawat, T. C., Chittoria, R. K., Reddy, P. K. et al. Role of lymphoscintigraphy in diagnosis and management of patients with leg swelling of unclear etiology. *Indian. J. Nucl. Med.* 2012;(27):226-230, doi:10.4103/0972-3919.115392.

26 Maclellan, R. A., Zurakowski, D., Voss, S. et al. Correlation Between Lymphedema Disease Severity and Lymphoscintigraphic Findings: A Clinical-Radiologic Study. *J. Am. Coll. Surg.* 2017;(225):366-370, doi:10.1016/j.jamcollsurg.2017.06.005.

27 Hassanein, A. H., Maclellan, R. A., Grant, F. D. et al. Diagnostic Accuracy of Lymphoscintigraphy for Lymphedema and Analysis of False-Negative Tests. *Plast. reconstr. surg., Glob. open.* 2017;(5).

28 Tartaglione, G., Visconti, G., Bartoletti, R. et al. Stress lymphoscintigraphy for early detection and management of secondary limb lymphedema. *Clin. Nucl. Med.* 2018;(43):155-161, doi:10.1097/rlu.0000000000001963.

29 Stanton, A. W., Mellor, R. H., Cook, G. J. et al. Impairment of lymph drainage in subfascial compartment of forearm in breast cancer-related lymphedema. *Lymphat. Res. Biol.* 2003;(1):121-132, doi:10.1089/153968503321642615.

30 O'Mahony, S., Rose, S. L., Chilvers, A. J. et al. Finding an optimal method for imaging lymphatic vessels of the upper limb. *Eur. J. Nucl. Med. Mol. Imaging.* 2004;(31):555-563, doi:10.1007/s00259-003-1399-3.

31 O'Mahony, S., Solanki, C. K., Barber, R. W. et al. Imaging of lymphatic vessels in breast cancer-related lymphedema: Intradermal versus subcutaneous injection of 99mTc-immunoglobulin. *Am. J. Roentgenol.* 2006;(186):1349-1355, doi:10.2214/ajr.04.1341.

32 Devoogdt, N., Van Den Wyngaert, T., Bourgeois, P. et al. Reproducibility of lymphoscintigraphic evaluation of the upper limb. *Lymphatic. Res. Biol.* 2014;(12):175-184, doi:10.1089/lrb.2013.0034.

33 Kim, Y. H., Hwang, J. H., Bae, J. H. et al. Predictive value of lymphoscintigraphy in patients with breast cancer-related lymphedema undergoing complex decongestive therapy. *Breast. Cancer. Res. Treat.* 2019;(173):735-741, doi:10.1007/s10549-018-5041-2.

34 Lee, B. & Bergan, J. New clinical and laboratory staging systems to improve management of chronic lymphedema. *Lymphology.* 2005;(38):122-129.

35 Maegawa, J., Mikami, T., Yamamoto, Y. et al. Types of lymphoscintigraphy and indications for lymphaticovenous anastomosis. *Microsurgery.* 2010;(30):437-442, doi:10.1002/micr.20772.

36 Mikami, T., Hosono, M., Yabuki, Y. et al. Classification of lymphoscintigraphy and relevance to surgical indication for lymphaticovenous anastomosis in upper limb lymphedema. *Lymphology.* 2011;(44):155-167.

37 Cheng, M. H., Pappalardo, M., Lin, C. et al. Validity of the Novel Taiwan Lymphoscintigraphy Staging and Correlation of Cheng Lymphedema Grading for Unilateral Extremity Lymphedema. *Ann. Surg.* 2018;(268):513-525, doi:10.1097/sla.0000000000002917.

38 Pappalardo, M., Lin, C., Ho, O. A. et al. Staging and clinical correlations of lymphoscintigraphy for unilateral gynecological cancer-related lymphedema. *J. Surg. Oncol.* 2020;(121):422-434.

39 Pecking, A. P., Albérini, J. L., Wartski, M. et al. Relationship between lymphoscintigraphy and clinical findings in lower limb lymphedema (LO): Toward a comprehensive staging. *Lymphology.* 2008;(41):1-10.

40 Kleinhans, E., Baumeister, R. G. H., Hahn, D. et al. Evaluation of transport kinetics in lymphoscintigraphy: Follow-up study in patients with transplanted lymphatic vessels. *Eur. J. Nucl. Med.* 1985;(10):349-352, doi:10.1007/BF00251310.

41 Campisi, C. C., Ryan, M., Villa, G. et al. Rationale for Study of the Deep Subfascial Lymphatic Vessels During Lymphoscintigraphy for the Diagnosis of Peripheral Lymphedema. *Clin. Nucl. Med.* 2019;(44):91-98, doi:10.1097/rlu.0000000000002400.

42 Infante, J. R., García, L., Laguna, P. et al. Lymphoscintigraphy for differential diagnosis of peripheral edema: Diagnostic yield of different scintigraphic patterns. *Rev. Esp. Med. Nucl. Imagen. Mol.* 2012;(31):237-242, doi:10.1016/j.remn.2011.11.011.

43 Yoo, J. N., Cheong, Y. S., Min, Y. S. et al. Validity of Quantitative Lymphoscintigraphy as a Lymphedema Assessment Tool for Patients With Breast Cancer. *Ann. Rehabil. Med.* 2015;(39):931-940.

44 Chiewvit, S. & Kumnerdnakta, S. Lymphoscintigraphic findings that predict favorable outcome after lymphaticovenous anastomosis. *Lymphology.* 2017;(50):1-8.

45 Pecking, A. P., Wartski, M., Cluzan, R. V. et al. SPECT-CT fusion imaging radionuclide lymphoscintigraphy: potential for limb lymphedema assessment and sentinel node detection in breast cancer. *Cancer. Treat. Res.* 2007;(135):79-84.

46 Baulieu, F., Bourgeois, P., Maruani, A. et al. Contributions of SPECT/CT imaging to the lymphoscintigraphy investigations of the lower limb lymphedema. *Lymphology.* 2013;(46):106-119.

47 Baulieu, F., Tauveron, V., Erra, B. et al. Lymphoscintigraphy in limb lymphoedema: Current methodology and interests. *Med Nucl.* 2015;(39):26-42, doi:10.1016/j.mednuc.2015.02.009.

48 Yamada, K., Shinaoka, A. & Kimata, Y. Three-Dimensional Imaging of Lymphatic System in Lymphedema Legs Using Interstitial Computed Tomography-lymphography. *Acta Med.* 2017;(71):171-177, doi:10.18926/amo/54986.

49 Mihara, M., Hara, H., Araki, J. et al. Indocyanine Green (ICG) lymphography is superior to lymphoscintigraphy for diagnostic imaging of early lymphedema of the upper limbs. *PLoS One.* 2012;(7), doi:10.1371/journal.pone.0038182.

50 Unno, N., Inuzuka, K., Suzuki, M. et al. Preliminary experience with a novel fluorescence lymphography using indocyanine green in patients with secondary lymphedema. *J. Vasc. Surg.* 2007;(45):1016-1021, doi:10.1016/j.jvs.2007.01.023.

51 Rasmussen, J. C., Tan, I., Marshall, M. V. et al. Human lymphatic architecture and dynamic transport imaged using near-infrared fluorescence. *Transl. Oncol.* 2010;(3):362-372, doi:10.1593/tlo.10190.

52 Suami, H., Chang, D., Skoracki, R. et al. Using indocyanine green fluorescent lymphography to demonstrate lymphatic architecture. *J. Lymphoedema.* 2012;(7):25-29.

53 Aldrich, M. B., Guilliod, R., Fife, C. E. et al. Lymphatic abnormalities in the normal contralateral arms of subjects with breast cancer-related lymphedema as assessed by near-infrared fluorescent imaging. *Biomed. Opt. Express.* 2012;(3):1256-1265.

54 Lee, Y. W., Lee, S. H., You, H. J. et al. Lymphatic vessel mapping in the upper extremities of a healthy Korean population. *Arch. Plast. Surg.* 2018;(45):152-157, doi:10.5999/aps.2017.00983.

55 Suami, H., Heydon-White, A., Mackie, H. et al. A new indocyanine green fluorescence lymphography protocol for identification of the lymphatic drainage pathway for patients with breast cancer-related lymphoedema. *BMC Cancer.* 2019;(19), doi:10.1186/s12885-019-6192-1.

56 Kinugawa, K., Nuri, T., Iwanaga, H. et al. Lymph Vessel Mapping Using Indocyanine Green Lymphography in the Nonaffected Side of Lower Leg. *Plast. reconstr. surg., Glob. open.* 2020;(8):e2929.

57 Akita, S., Nakamura, R., Yamamoto, N. et al. Early Detection of Lymphatic Disorder and Treatment for Lymphedema following Breast Cancer. *Plast. Reconstr. Surg.* 2016;(138):192e-202e, doi:10.1097/prs.0000000000002337.

58 Tashiro, K., Yamashita, S., Koshima, I. et al. Visualization of Accessory Lymphatic Pathways in Secondary Upper Extremity Lymphedema Using Indocyanine Green Lymphography. *Ann. Plast. Surg.* 2017;(79):393-396, doi:10.1097/sap.0000000000001120.

59 Johnson, A. R., Granoff, M. D., Suami, H. et al. Real-time visualization of the mascagni-sappey pathway utilizing ICG lymphography. *Cancers.* 2020;(12), doi:10.3390/cancers12051195.

60 Garza, R. M., Ooi, A. S. H., Falk, J. et al. The Relationship Between Clinical and Indocyanine Green Staging in Lymphedema. *Lymphat. Res. Biol.* 2019;(17):329-333.

61 Yoon, J. A., Shin, M. J., Shin, Y. B. et al. Correlation of ICG lymphography and lymphoscintigraphy severity stage in secondary upper limb lymphedema. *J. Plast. Reconstr. Aesthetic. Surg.* 2020;(73):1982-1988, doi:10.1016/j.bjps.2020.08.055.

62 Jørgensen, M. G., Toyserkani, N. M., Hansen, F. C. G. et al. Prospective validation of indocyanine green lymphangiography staging of breast cancer-related lymphedema. *Cancers.* 2021;(13), doi:10.3390/cancers13071540.

63 Yoon, J. A., Shin, M. J. & Kim, J. H. Indocyanine green lymphography and lymphoscintigraphy severity stage showed strong correlation in lower limb lymphedema. *Lymphatic. Res. Biol.* 2021;(19):80-85, doi:10.1089/lrb.2020.0043.

64 Yamamoto, T., Narushima, M., Doi, K. et al. Characteristic indocyanine green lymphography findings in lower extremity lymphedema: the generation of a novel lymphedema severity staging system using dermal backflow patterns. *Plast. Reconstr. Surg.* 2011;(127):1979-1986.

65 Hara, H., Mihara, M., Seki, Y. et al. Comparison of indocyanine green lymphographic findings with the conditions of collecting lymphatic vessels of limbs in patients with lymphedema. *Plast. Reconstr. Surg.* 2013;(132):1612-1618.

66 Thomis, S., Dams, L., Fourneau, I. et al. Correlation between Clinical Assessment and Lymphofluoroscopy in Patients with Breast Cancer-Related Lymphedema: A Study of Concurrent Validity. *Lymphatic. Res. Biol.* 2020;(18):539-548, doi:10.1089/lrb.2019.0090.

67 Yamamoto, T., Narushima, M., Yoshimatsu, H. et al. Dynamic Indocyanine Green (ICG) lymphography for breast cancer-related arm lymphedema. *Ann. Plast. Surg.* 2014;(73):706-709, doi:10.1097/SAP.0b013e318285875f.

68 Yamamoto, T., Matsuda, N., Doi, K. et al. The earliest finding of indocyanine green lymphography in asymptomatic limbs of lower extremity lymphedema patients secondary to cancer treatment: the modified dermal backflow stage and concept of subclinical lymphedema. *Plast. Reconstr. Surg.* 2011;(128):314e-321e.

69 Akita, S., Mitsukawa, N., Rikihisa, N. et al. Early diagnosis and risk factors for lymphedema following lymph node dissection for gynecologic cancer. *Plast. Reconstr. Surg.* 2013;(131):283-290.

70 Yamamoto, T., Narushima, M., Yoshimatsu, H. et al. Indocyanine green velocity: lymph transportation capacity deterioration with progression of lymphedema. *Ann. Plast. Surg.* 2013;(71):591-594.

71 Yamamoto, T., Yamamoto, N., Doi, K. et al. Indocyanine green-enhanced lymphography for upper extremity lymphedema: a novel severity staging system using dermal backflow patterns. *Plast. Reconstr. Surg.* 2011;(128):941-947.

72 Hara, H. & Mihara, M. Multi-area lymphaticovenous anastomosis with multi-lymphosome injection in indocyanine green lymphography: A prospective study. *Microsurgery.* 2019;(39):167-173, doi:10.1002/micr.30398.

73 Hara, H. & Mihara, M. Multilymphosome injection indocyanine green lymphography can detect more lymphatic vessels than lymphoscintigraphy in lymphedematous limbs. *J. Plast. Reconstr. Aesthetic. Surg.* 2020;(73):1025-1030, doi:10.1016/j.bjps.2020.01.021.

74 Tashiro, K., Yamashita, S., Saito, T. et al. Proximal and distal patterns: Different spreading patterns of indocyanine green lymphography in secondary lower extremity lymphedema. *J. Plast. Reconstr. Aesthetic. Surg.* 2016;(69):368-375, doi:10.1016/j.bjps.2015.10.042.

75 Mihara, M., Hayashi, Y., Hara, H. et al. High-accuracy diagnosis and regional classification of lymphedema using indocyanine green fluorescent lymphography after gynecologic cancer treatment. *Ann Plast Surg.* 2014;(72):204-208.
76 Shinaoka, A., Koshimune, S., Yamada, K. et al. Accelerated Lymph Flow in Early-Stage Secondary Lymphedema Detected by Indocyanine Green Fluorescence Lymphography. *J. Reconstr. Microsurg.* 2017;(33):596-602, doi:10.1055/s-0037-1603740.
77 Matsumoto, K., Shinaoka, A., Yamada, K. et al. Exercise-Loaded Indocyanine Green Fluorescence Lymphangiography for Diagnosing Lymphedema. *J. Reconstr. Microsurg.* 2019;(35):138-144, doi:10.1055/s-0038-1667366.
78 Medina-Rodríguez, M. E., de-la-Casa-Almeida, M., Mena-Rodríguez, A. et al. Relationship between perimetric increase and fluoroscopic pattern type in secondary upper limb lymphedema observed by Indocyanine green lymphography. *Medicine (Baltimore).* 2020;(99):e20432, doi:10.1097/md.0000000000020432.
79 Mihara, M., Hara, H., Narushima, M. et al. Indocyanine green lymphography is superior to lymphoscintigraphy in imaging diagnosis of secondary lymphedema of the lower limbs. *J. Vasc. Surg. Venous. Lymphatic. Disord.* 2013;(1):194-201, doi:10.1016/j.jvsv.2012.07.011.
80 Unno, N., Nishiyama, M., Suzuki, M. et al. Quantitative lymph imaging for assessment of lymph function using indocyanine green fluorescence lymphography. *Eur. J. Vasc. Endovasc. Surg.* 2008;(36):230-236.
81 Kelly, B., Mohanakumar, S., Telinius, N. et al. Function of Upper Extremity Human Lymphatics Assessed by Near-Infrared Fluorescence Imaging. *Lymphat. Res. Biol.* 2020;(18):226-231.
82 Granoff, M. D., Johnson, A. R., Lee, B. T. et al. A Novel Approach to Quantifying Lymphatic Contractility during Indocyanine Green Lymphangiography. *Plast. Reconstr. Surg.* 2019;(144):1197-1201, doi:10.1097/prs.0000000000006176.
83 Groenlund, J. H., Telinius, N., Skov, S. N. et al. A Validation Study of Near-Infrared Fluorescence Imaging of Lymphatic Vessels in Humans. *Lymphat. Res. Biol.* 2017;(15):227-234.
84 Mihara, M., Seki, Y., Hara, H. et al. Predictive lymphatic mapping: a method for mapping lymphatic channels in patients with advanced unilateral lymphedema using indocyanine green lymphography. *Ann Plast Surg.* 2014;(72):706-710, doi:10.1097/SAP.0b013e31826a18b1.
85 Gentileschi, S., Servillo, M., Albanese, R. et al. Lymphatic mapping of the upper limb with lymphedema before lymphatic supermicrosurgery by mirroring of the healthy limb. *Microsurgery.* 2017;(37):881-889, doi:10.1002/micr.30247.
86 Akita, S., Mitsukawa, N., Kazama, T. et al. Comparison of lymphoscintigraphy and indocyanine green lymphography for the diagnosis of extremity lymphoedema. *J. Plast. Reconstr. Aesthetic. Surg.* 2013;(66):792-798, doi:10.1016/j.bjps.2013.02.023.
87 Liu, N. & Zhang, Y. Magnetic Resonance Lymphangiography for the Study of Lymphatic System in Lymphedema. *J. Reconstr. Microsurg.* 2016;(32):66-71, doi:10.1055/s-0034-1384213.
88 Bae, J. S., Yoo, R. E., Choi, S. H. et al. Evaluation of lymphedema in upper extremities by MR lymphangiography: Comparison with lymphoscintigraphy. *Magn. Reson. Imaging.* 2018;(49):63-70, doi:10.1016/j.mri.2017.12.024.
89 Lohrmann, C., Foeldi, E., Bartholomae, J. P. et al. Gadoteridol for MR imaging of lymphatic vessels in lymphoedematous patients: Initial experience after intracutaneous injection. *Br. J. Radiol.* 2007;(80):569-573, doi:10.1259/bjr/95414884.
90 Lohrmann, C., Foeldi, E., Speck, O. et al. High-resolution MR lymphangiography in patients with primary and secondary lymphedema. *Am. J. Roentgenol.* 2006;(187):556-561.
91 Lohrmann, C., Foeldi, E. & Langer, M. Indirect magnetic resonance lymphangiography in patients with lymphedema. Preliminary results in humans. *Eur. J. Radiol.* 2006;(59):401-406, doi:10.1016/j.ejrad.2006.02.012.
92 Ripley, B., Wilson, G. J., Lalwani, N. et al. Initial clinical experience with dual-agent relaxation contrast for isolated lymphatic channel mapping. *Radiology.* 2018;(286):705-714, doi:10.1148/radiol.2017170241.
93 Lohrmann, C., Foeldi, E., Bartholomä, J. P. et al. Magnetic resonance imaging of lymphatic vessels without image subtraction: A practicable imaging method for routine clinical practice? *J. Comput. Assisted. Tomogr.* 2007;(31):303-308, doi:10.1097/01.rct.0000237814.33925.32.
94 Weiss, M., Burgard, C., Baumeister, R. et al. Magnetic resonance imaging versus lymphoscintigraphy for the assessment of focal lymphatic transport disorders of the lower limb: First experiences. *Nuklearmedizin.* 2014;(53):190-196, doi:10.3413/Nukmed-0649-14-03.
95 Liu, N. F., Yan, Z. X., Wu, X. F. et al. Magnetic resonance lymphography demonstrates spontaneous lymphatic disruption and regeneration in obstructive lymphedema. *Lymphology.* 2013;(46):56-63.
96 Lohrmann, C., Föld, E., Bartholomä, J. P. et al. MR imaging of the lymphatic system: Distribution and contrast enhancement of gadodiamide after intradermal injection. *Lymphology.* 2006;(39):156-163.
97 Notohamiprodjo, M., Weiss, M., Baumeister, R. G. et al. MR lymphangiography at 3.0 T: Correlation with lymphoscintigraphy. *Radiology.* 2012;(264):78-87, doi:10.1148/radiol.12110229.
98 Zeltzer, A. A., Brussaard, C., Koning, M. et al. MR lymphography in patients with upper limb lymphedema: The GPS for feasibility and surgical planning for lympho-venous bypass. *J. Surg. Oncol.* 2018;(118):407-415, doi:10.1002/jso.25145.
99 Notohamiprodjo, M., Baumeister, R. G. H., Jakobs, T. F. et al. MR-lymphangiography at 3.0T - A feasibility study. *Eur. Radiol.* 2009;(19):2771-2778, doi:10.1007/s00330-009-1461-z.
100 Dimakakos, E. P., Koureas, A., Koutoulidis, V. et al. Interstitial magnetic resonance lymphography: The clinical effectiveness of a new method. *Lymphology.* 2008;(41):116-125.
101 Soga, S., Onishi, F., Jinzaki, M. et al. Analysis of collateral lymphatic circulation in patients with lower limb lymphedema using magnetic resonance lymphangiography. *J. Vasc. Surg. Venous. Lymphati.c Disord.* 2021;(9):471-481.e471, doi:10.1016/j.jvsv.2020.04.029.
102 Mazzei, M. A., Gentili, F., Mazzei, F. G. et al. High-resolution MR lymphangiography for planning lymphaticovenous anastomosis treatment: a single-centre experience. *Radiol. Med.* 2017;(122):918-927, doi:10.1007/s11547-017-0795-x.

103 Borri, M., Schmidt, M. A., Gordon, K. D. et al. Quantitative Contrast-Enhanced Magnetic Resonance Lymphangiography of the Upper Limbs in Breast Cancer Related Lymphedema: An Exploratory Study. *Lymphatic. Res. Biol.* 2015;(13):100-106, doi:10.1089/lrb.2014.0039.
104 Gennaro, P., Borghini, A., Chisci, G. et al. Could MRI visualize the invisible? An Italian single center study comparing magnetic resonance lymphography (MRL), super microsurgery and histology in the identification of lymphatic vessels. *Eur. Rev. Med. Pharmacol. Sci.* 2017;(21):687-694.
105 Jeon, J. Y., Lee, S. H., Shin, M. J. et al. Three-dimensional isotropic fast spin-echo MR lymphangiography of T1-weighted and intermediate-weighted pulse sequences in patients with lymphoedema. *Clin. Radiol.* 2016;(71):e56-e63, doi:10.1016/j.crad.2015.10.015.
106 Lu, Q., Delproposto, Z., Hu, A. et al. MR Lymphography of Lymphatic Vessels in Lower Extremity with Gynecologic Oncology-Related Lymphedema. *PLoS One.* 2012;(7), doi:10.1371/journal.pone.0050319.
107 Sheng, L., Zhang, G., Li, S. et al. Magnetic Resonance Lymphography of Lymphatic Vessels in Upper Extremity With Breast Cancer–Related Lymphedema. *Ann. Plast. Surg.* 2020;(84):100-105, doi:10.1097/SAP.0000000000001994.
108 Zhou, G. X., Chen, X., Zhang, J. H. et al. MR lymphangiography at 3.0 Tesla to assess the function of inguinal lymph node in low extremity lymphedema. *J. Magn. Reson. Imaging.* 2014;(40):1430-1436, doi:10.1002/jmri.24499.
109 Pons, G., Clavero, J. A., Alomar, X. et al. Preoperative planning of lymphaticovenous anastomosis: The use of magnetic resonance lymphangiography as a complement to indocyanine green lymphography. *J. Plast. Reconstr. Aesthet. Surg.* 2019;(72):884-891.
110 Yasunaga, Y., Nakajima, Y., Mimura, S. et al. Magnetic resonance lymphography as three-dimensional navigation for lymphaticovenular anastomosis in patients with leg lymphedema. *J. Plast. Reconstr. Aesthetic. Surg.* 2020, doi:10.1016/j.bjps.2020.10.099.
111 Abdelfattah, U., Jaimez, P. M., Clavero, J. A. et al. Correlation between superficial and deep lymphatic systems using magnetic resonance lymphangiography in breast cancer-related lymphedema: Clinical implications. *J. Plast. Reconstr. Aesthetic. Surg.* 2020;(73):1018-1024, doi:10.1016/j.bjps.2019.11.053.
112 Cellina, M., Martinenghi, C., Panzeri, M. et al. Noncontrast MR Lymphography in Secondary Lower Limb Lymphedema. *J. Magn. Reson. Imaging.* 2020, doi:10.1002/jmri.27328.
113 Cellina, M., Gibelli, D., Martinenghi, C. et al. Noncontrast Magnetic Resonance Lymphography in Secondary Lymphedema Due to Prostate Cancer. *Lymphat. Res. Biol.* 2020, doi:10.1089/lrb.2020.0034.
114 Crescenzi, R., Donahue, P. M. C., Hartley, K. G. et al. Lymphedema evaluation using noninvasive 3T MR lymphangiography. *J. Magn. Reson. Imaging.* 2017;(46):1349-1360, doi:10.1002/jmri.25670.
115 Liu, N., Wang, C. & Sun, M. Noncontrast three-dimensional magnetic resonance imaging vs lymphoscintigraphy in the evaluation of lymph circulation disorders: A comparative study. *J. Vasc. Surg.* 2005;(41):65-75, doi:10.1016/j.jvs.2004.11.013.
116 Long, X., Zhang, J., Zhang, D. et al. Microsurgery guided by sequential preoperative lymphography using 68Ga-NEB PET and MRI in patients with lower-limb lymphedema. *Eur. J. Nucl. Med. Mol. Imaging.* 2017;(44):1501-1510, doi:10.1007/s00259-017-3676-6.
117 Hou, G., Hou, B., Jiang, Y. et al. 68Ga-NOTA-Evans Blue TOF PET/MR Lymphoscintigraphy Evaluation of the Severity of Lower Limb Lymphedema. *Clin. Nucl. Med.* 2019;(44):439-445, doi:10.1097/rlu.0000000000002584.
118 Lu, Q., Xu, J. & Liu, N. Chronic lower extremity lymphedema: A comparative study of high-resolution interstitial MR lymphangiography and heavily T2-weighted MRI. *Eur. J. Radiol.* 2010;(73):365-373, doi:10.1016/j.ejrad.2008.10.041.
119 Hayashi, A., Yamamoto, T., Yoshimatsu, H. et al. Ultrasound visualization of the lymphatic vessels in the lower leg. *Microsurgery.* 2016;(36):397-401.
120 Mihara, M., Hara, H. & Kawakami, Y. Ultrasonography for classifying lymphatic sclerosis types and deciding optimal sites for lymphatic-venous anastomosis in patients with lymphoedema. *J. Plast. Reconstr. Aesthet. Surg.* 2018;(71):1274-1281.
121 Hayashi, A., Hayashi, N., Yoshimatsu, H. et al. Effective and efficient lymphaticovenular anastomosis using preoperative ultrasound detection technique of lymphatic vessels in lower extremity lymphedema. *J. Surg. Oncol.* 2018;(117):290-298, doi:10.1002/jso.24812.
122 Hara, H. & Mihara, M. Change of the Lymphatic Diameter in Different Body Positions. *Lymphat. Res. Biol.* 2020, doi:10.1089/lrb.2020.0081.
123 Czedik-Eysenberg, M., Steinbacher, J., Obermayer, B. et al. Exclusive use of ultrasound for locating optimal LVA sites—A descriptive data analysis. *J. Surg. Oncol.* 2020;(121):51-56, doi:10.1002/jso.25728.
124 Hara, H. & Mihara, M. Diagnosis of Lymphatic Dysfunction by Evaluation of Lymphatic Degeneration with Lymphatic Ultrasound. *Lymphat. Res. Biol.* 2021, doi:10.1089/lrb.2019.0071.
125 Hayashi, A., Giacalone, G., Yamamoto, T. et al. Ultra High-frequency Ultrasonographic Imaging with 70 MHz Scanner for Visualization of the Lymphatic Vessels. *Plast. reconstr. surg., Glob. open.* 2019;(7):e2086.
126 Bianchi, A., Visconti, G., Hayashi, A. et al. Ultra-High frequency ultrasound imaging of lymphatic channels correlates with their histological features: A step forward in lymphatic surgery. *J. Plast. Reconstr. Aesthetic. Surg.* 2020;(73):1622-1629, doi:10.1016/j.bjps.2020.05.053.
127 Kajita, H., Oh, A., Urano, M. et al. Photoacoustic lymphangiography. *J. Surg. Oncol.* 2020;(121):48-50.
128 Suzuki, Y., Kajita, H., Konishi, N. et al. Subcutaneous lymphatic vessels in the lower extremities: Comparison between photoacoustic lymphangiography and near-infrared fluorescence lymphangiography. *Radiology.* 2020;(295):469-474, doi:10.1148/radiol.2020191710.
129 Pappalardo, M. & Cheng, M.-H. Lymphoscintigraphy for the diagnosis of extremity lymphedema: Current controversies regarding protocol, interpretation, and clinical application. *J. Surg. Oncol.* 2020;(121):37-47, doi:10.1002/jso.25526.
130 Murawa, D., Hirche, C., Dresel, S. et al. Sentinel lymph node biopsy in breast cancer guided by indocyanine green fluorescence. *Br. J. Surg.* 2009;(96):1289-1294, doi:10.1002/bjs.6721.

131 Cornelissen, A. J. M., van Mulken, T. J. M., Graupner, C. et al. Near-infrared fluorescence image-guidance in plastic surgery: A systematic review. *Eur. J. Plast. Surg.* 2018;(41):269-278, doi:10.1007/s00238-018-1404-5.
132 Sheng, L., Zhang, G., Li, S. et al. Magnetic Resonance Lymphography of Lymphatic Vessels in Upper Extremity With Breast Cancer-Related Lymphedema. *Ann. Plast. Surg.* 2020;(84):100-105, doi:10.1097/sap.0000000000001994.
133 Arrivé, L., Derhy, S., Dahan, B. et al. Primary lower limb lymphoedema: classification with non-contrast MR lymphography. *Eur. Radiol.* 2018;(28):291-300, doi:10.1007/s00330-017-4948-z.
134 Baz, A. A., Hassan, T. A., Atta, A. T. et al. Role of contrast enhanced MRI lymphangiography in evaluation of lower extremity lymphatic vessels for patients with primary lymphedema. *Egypt. J. Rad. NuMed.* 2018;(49):776-781, doi:10.1016/j.ejrnm.2018.06.005.
135 Liu, N. F., Yan, Z. X. & Wu, X. F. Classification of lymphatic-system malformations in primary lymphoedema based on MR lymphangiography. *Eur. J. Vasc. Endovasc. Surg.* 2012;(44):345-349, doi:10.1016/j.ejvs.2012.06.019.
136 Kajita, H., Suzuki, Y., Sakuma, H. et al. Visualization of Lymphatic Vessels Using Photoacoustic Imaging. *Keio. J. Med.* 2020:1-11, doi:10.2302/kjm.2020-0010-oa.
137 Kuniyil Ajith Singh, M., Agano, T., Sato, N. et al. Real-time in vivo imaging of human lymphatic system using an LED-based photoacoustic/ultrasound imaging system. *SPIE BiOS.* 2018:3-3, doi:10.1117/12.2290871.
138 Giacalone, G., Yamamoto, T., Belva, F. et al. Bedside 3D Visualization of Lymphatic Vessels with a Handheld Multispectral Optoacoustic Tomography Device. *J. Clin. Med.* 2020;(9):815-815, doi:10.3390/jcm9030815.

3

Photoacoustic imaging of hemoglobin and indocyanine green: investigations on image quality

Abstract

Photoacoustic imaging (PAI) is a hybrid imaging modality that combines optical imaging contrast and the spatial resolution of ultrasonic (US) imaging. It can visualize exogenous chromophores such as indocyanine green (ICG) and endogenous chromophores such as hemoglobin in blood. Many factors play a role in the obtained image signal strength and resolution.

This chapter describes phantom experiments with a LED-based photoacoustic imaging device (Acoustic X). Three phantom experiments of ICG filled tubes in water were done to show the effect of absorber depth, absorber concentration, number of frame averages and light pulse width on image quality. Additional experiments aimed to demonstrate PAI of ICG and hemoglobin with two wavelengths (820 and 940 nm). Lastly, in-vivo imaging of blood vessels in the wrist was done to illustrate the benefits of skin-melanin surface suppression in the generation of 3D maximum intensity projections (MIP).

The experimental results showed that dual-wavelength PAI makes it possible to differentiate blood from ICG using the ratio between 940 nm and 820 nm PA signal. Additionally, skin-melanin surface suppression improved the quality of MIPs of blood vessels. In term of image parameters, there is a trade-off between the frame rate and the image quality depending on the absorber characteristics and depth, and type of application (e.g., static versus dynamic processes). Finally, 70 ns was the optimal pulse width to capture the PA signal over the entire frequency range of the ultrasound probe used in this study while maintaining sufficient image resolution and signal strength.

3.1 Introduction

3.1.1 Fundamentals of photoacoustic imaging

Photoacoustic (PA) imaging is a hybrid soft tissue imaging modality based on the photoacoustic effect. The technique exploits optical imaging contrast and the spatial resolution of ultrasonic (US) imaging. The principle of photoacoustic imaging can be subdivided into light propagation and acoustic propagation and detection (see Figure 3.1). First, a short light pulse illuminates a region of interest. Photons scatter in the tissue and are absorbed by chromophores which can be endogenous (e.g., melanin, hemoglobin) or exogenous (e.g., indocyanine green (ICG)), resulting in a 3D distribution of absorbed energy. Optical absorption causes a local rise in temperature and thermoelastic expansion, subsequently leading to a pressure rise in the form of acoustic waves. The acoustic wave can then be detected by an ultrasonic detector on the surface of the tissue. The obtained acoustic pressure time series is reconstructed to get an image of the initial acoustic pressure distribution (p_0) (i.e., the photoacoustic image).[1,2]

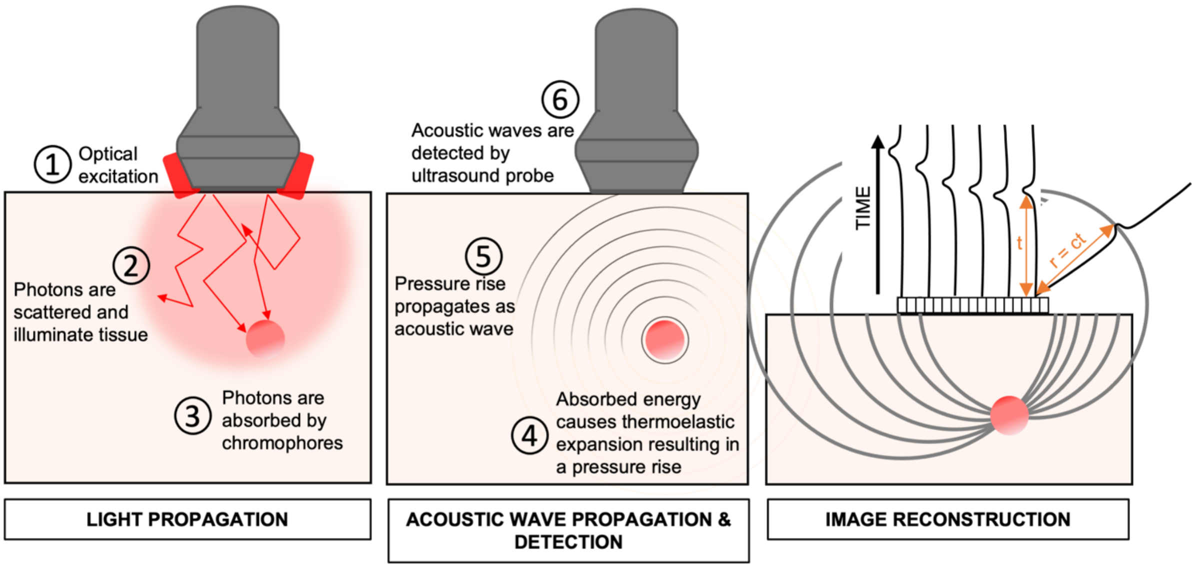

Figure 3.1: Principles of photoacoustic imaging (r: radius; c: speed of sound; t: time). First, a light pulse is sent into a region of interest and photons are scattered and absorbed by the tissue and specific chromophores. Absorbed energy causes thermoelastic expansion in the form of acoustic waves, which are detected by an ultrasound probe at the surface. Acquired pressure time series are then reconstructed to approximate the locations of optical absorption.

The signal strength of the photoacoustic image represented by the initial acoustic pressure distribution (p_0) at location $\boldsymbol{x}$ depends on: (1) the absorbed power density (H), which is proportional to the absorption coefficient (μ_a) of the chromophore and the light fluence (F); and (2) the Grünheisen parameter (Γ), a unitless parameter that represents the efficiency of absorbed energy to pressure (Equation 1).[3]

$$p_0(\boldsymbol{x},\lambda) = \Gamma H(\boldsymbol{x},\lambda) = \Gamma(\boldsymbol{x})\,\mu_a(\boldsymbol{x},\lambda)F(\boldsymbol{x}) \tag{1}$$

The absorption coefficient depends on the molar absorption (α_k) at the used wavelength (λ) and the concentration (C_k) of the chromophores (Equation 2).

$$\mu_a(\boldsymbol{x},\lambda) = \sum_k C_k(\boldsymbol{x})\alpha_k(\lambda) \tag{2}$$

For accurate PA image reconstruction, the thermal and stress confinement should be met. In case of thermal confinement, heat diffusion during the light pulse is neglected (i.e., the light pulse duration is much shorter than the thermal relaxation time of the heated region). In that case, the induced pressure wave $p(\boldsymbol{x}, t)$ obeys Equation 3, where the left hand side represent the acoustic wave equation and the right hand side the initial acoustic pressure distribution, with c as the speed of sound in the propagating medium.[1,2]

$$\frac{1}{c^2}\frac{\partial^2 p(\boldsymbol{x},t)}{\partial t^2} - \nabla^2 p(\boldsymbol{x},t) = \Gamma\frac{\partial H(\boldsymbol{x},t)}{\partial t} \qquad [3]$$

Stress confinement assumes that acoustic propagation is negligible during the optical pulse due to its relatively short duration. The light pulse (t_{pulse}) needs to the shorter than the acoustic transit across the scale of the absorber $(d_{absorber})$ to satisfy stress confinement (Equation 4).[4]

$$t_{pulse} < \frac{d_{absorber}}{c_{absorber}} \qquad [4]$$

The absorbed energy density can then be approximated by the Dirac delta function and $H(\boldsymbol{x}, t)$ is reduced to $H(\boldsymbol{x}, t) = H(\boldsymbol{x})\delta(t)$, leading to the following initial value problem[1-3]:

$$\frac{1}{c^2}\frac{\partial^2 p(\boldsymbol{x},t)}{\partial t^2} - \nabla^2 p(\boldsymbol{x},t) = 0 \qquad [5]$$

$$p_0(\boldsymbol{x}) = p(\boldsymbol{x}, t=0) = \Gamma H(\boldsymbol{x}) \qquad [6]$$

$$\left.\frac{\partial p(\boldsymbol{x},t)}{\partial t}\right|_{t=0} = 0 \qquad [7]$$

$$p(\boldsymbol{x}_d, t) = p_d(\boldsymbol{x}_d, t) \qquad [8]$$

Equation 6 represents the initial acoustic pressure distribution and equation 7 states that the initial particle velocity is zero (i.e., stress confinement). To reconstruct to PA image $p_0(\boldsymbol{x})$ from the detected acoustic time series at the detector surface $p_d(\boldsymbol{x}_d, t)$ an inverse problem must be solved. Several reconstruction algorithms can be applied to solve this inverse problem with each its advantages and disadvantages.[5] Fourier-based reconstruction methods are computationally efficient and suitable for real-time imaging.[3] The reconstruction is based on the decomposition of the pressure waves into plane waves. Fourier domain reconstruction for planar geometry transforms the time-dependent pressure data from space-time domain $\left(p_d(x, y, t)\right)$ into the frequency domain using the Fourier transform $\left(p_d\left(k_x, k_y, \omega\right)\right)$. Secondly, the temporal component (ω) is mapped to the corresponding spatial coordinate, resulting in the initial pressure distribution in Fourier space $\left(p_0\left(k_x, k_y, k_z\right)\right)$. The inverse Fourier transform is applied to obtain the reconstructed image, resulting in an image of the initial pressure distribution.[6-8]

3.1.2 Light absorption properties of indocyanine green and hemoglobin

ICG has been used as an exogenous contrast agent for a wide variety of imaging purposes due to its specific metabolic, fluorescence and light absorption features. It is also used for lymphatic vessel imaging.[9] The absorption spectrum depends on the nature of the solvent and the concentration. ICG is only stable for a couple of hours in water and the absorption peak significantly changes with different concentrations due to aggregation at higher concentrations. In human plasma, ICG binds to albumin proteins and the absorption peak shifts to a higher wavelength (~810 nm).[10,11]

ICG shows no absorption at wavelengths higher than 900 nm, while both oxygenated and deoxygenated hemoglobin have limited variability in optical absorption coefficients in the range of 800 – 950 nm. Figure 3.2 shows the relative absorption spectra of blood and ICG together with the absorption spectra of ICG in water and plasma at different concentrations.[10,11]

The pronounced differences of the ICG and blood absorption spectra can be exploited for dual-wavelength PAI.

PA signals from wavelengths near the absorption peak of ICG produce a high signal, while the produced PA is signal low at wavelengths > 900 nm. The signal magnitude from hemoglobin in blood is approximately the same at both these wavelengths. Computation of the (pulse energy corrected) intensity ratio $\frac{signal\ intensity\ at\ \lambda > 900\ nm}{signal\ intensity\ at\ \lambda \sim 800\ nm}$ should therefore result in low ratio values for ICG and high values for blood.

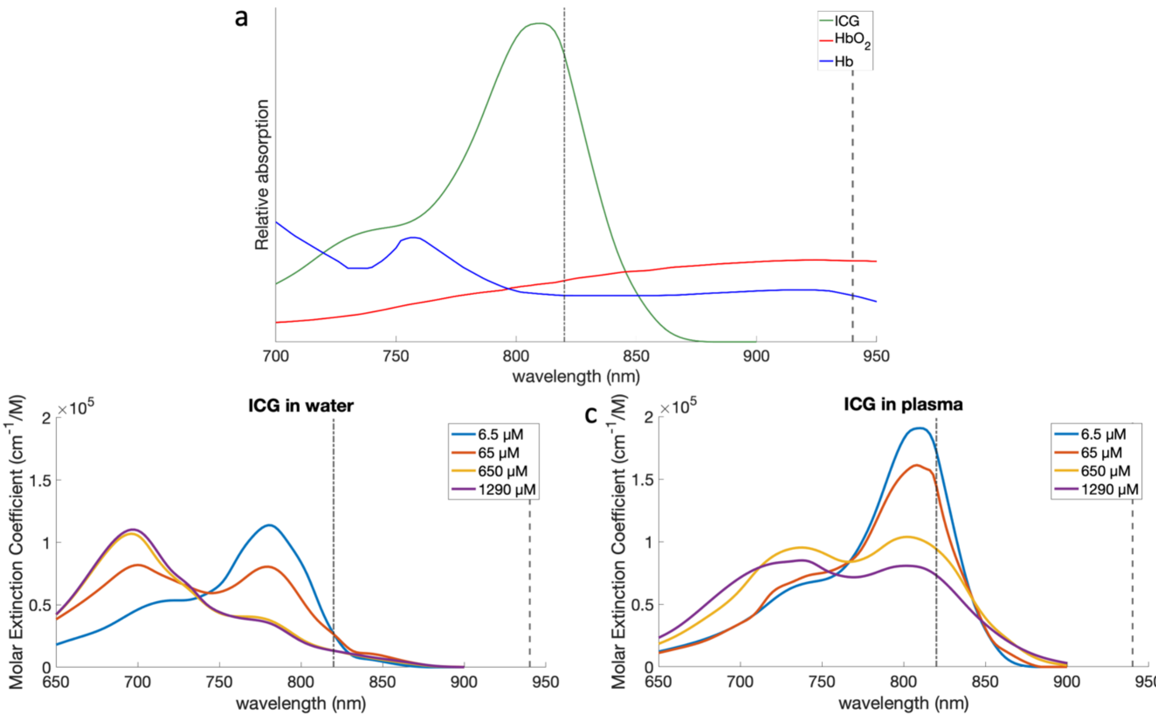

*Figure 3.2: **(a)** Relative absorption spectra of indocyanine green (ICG), oxygenated hemoglobin (Hb02) and deoxygenated hemoglobin (Hb). **(b)** Absorption spectra of ICG in water at different concentrations. **(c)** Absorption spectra of ICG in plasma at different concentrations. Dotted lines represent wavelengths 820 and 940 nm. Graphs reproduced from original data by ref [11] and digitized data from ref [12].*

3.1.3 LED-based photoacoustic imaging

Most PAI techniques use high-power laser-based systems, which provide pulse excitation power in the mJ range with tunable wavelengths. Although laser-based systems work well in pre-clinical settings, clinical use is not as straightforward. These systems are bulky, complex, expensive and require additional safety measures such as eye safety goggles, hindering the clinical translation of PAI.[13]

Light-emitting diode (LED) based systems are inexpensive, portable and safe alternatives. The downside is the limited pulse energy output (μJ range), leading to lower signal-to-noise ratios (SNR) of the acquired images and the need for averaging frames.[14,15] However, since the pulse repetition frequency (PRF) is much higher (in the kHz range), real-time imaging with comparable SNR to laser-based PAI is feasible.[16]

LED-based PAI has been demonstrated for several clinical implementations such as imaging of port-wine stains[17], inflammatory arthritis in the finger[18,19] and enthesitis[20] or guidance of minimally invasive procedures.[14] As described in Chapter 2, photoacoustic imaging is also interesting for lymphatic vessel imaging, but current laser-based systems make direct clinical implementation tedious. Thus, LED-based photoacoustic imaging is also interesting in the field of lymphatic surgery.[21]

3.1.4 Objectives

In this study, we investigated the influence of several parameters on image quality in phantom experiments using a LED-based PAI system (Acoustic X, Cyberdyne Inc., Tsukuba, Japan). We looked at the influence of optical absorber concentration and depth, light pulse width and the number of frame averages on imaging performance with this system. We also aimed to demonstrate the principle of dual-wavelength photoacoustic imaging of hemoglobin and ICG along with in-vivo skin-melanin surface suppression functionalities. These findings aimed to improve the understanding of what can be expected with in-vivo imaging and choose the optimal imaging parameters.

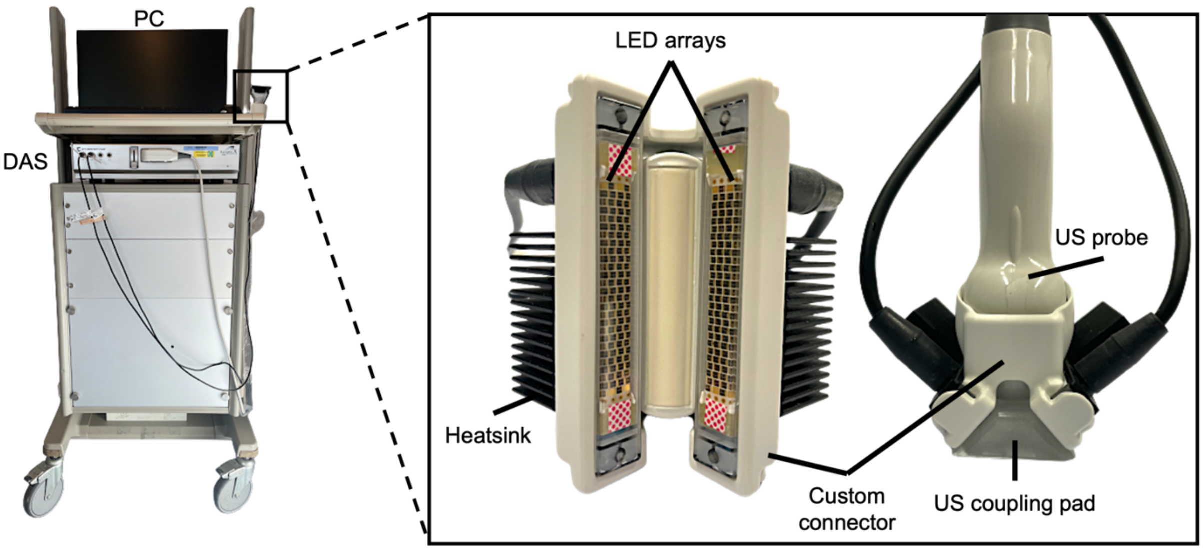

Figure 3.3: The Acoustic X system on a medical trolley. The system consists of a PC, data acquisition system (DAS), the ultrasound (US) probe and the light-emitting diode arrays (LED). The US probe and LEDs are connected to the DAS. The LEDs are attached to the US probe with a custom connector. A custom US coupling pad is used for acoustic coupling with the imaged surface.

3.2 Methods

3.2.1 LED-based PAI system

In this work, a LED-based PA/US system (Acoustic X, Cyberdyne Inc., Tsukuba, Japan) was used. Figure 3.3 shows images of the device and its components. It performs interleaved PA and US measurements at video frame rate. LED arrays with wavelengths of 820 and 940 nm were used to deliver PA excitation light pulses from two sides of the probe. Each LED consists of 144 elements arranged in four rows, where the first and third row are embedded with 820 nm LEDs and the second and fourth row consist of 940 nm elements. At a pulse width of 70 ns, the optical energy is 128 µJ and 114 µJ per pulse for 820 and 940 nm, respectively.[22] The PRF is tunable between 1 - 4 kHz with increments of 1 kHz and the light pulse duration is tunable between 30 ns and 150 ns with a 5 ns step size. The LED arrays were fixed to the ultrasound probe using a custom connector. The linear handheld ultrasound probe (PZT-based) consists of 128 channels with a pitch of 0.3 mm with a central frequency of 7 MHz, 80% fractional bandwidth and an elevation focus at 15 mm. The system provides a sampling rate of 20 and 40 MHz for US and PA acquisition, respectively. Both PA and US image reconstruction is done with a built-in GPU-based Fourier-domain reconstruction algorithm.[6] Online averaging is possible from 128 to 2560 frame averages leading to frame rates between 1.5 – 30 Hz at a PRF of 4 kHz.

3.2.2 Phantom and experiment set-up

Here we describe the set-up of five experiments investigating the influence of several parameters and settings on PA image quality. The first three experiments looked at the influence of several imaging parameters such as absorber concentration and depth (experiment 1), the number of frame averages (experiment 2) and the light pulse width (experiment 3) on image quality. Further, we aimed to demonstrate simultaneous imaging of blood and ICG (experiment 4) and the surface suppression functionalities for improving 3D image quality (experiment 5).

For all experiments, 820 and 940 nm LEDs were used with a PRF of 4 kHz. A schematic overview of all experiments is shown in Figure 3.4 and are experimental set-ups are described below. Experiments 1 – 4 were done in water for acoustic coupling and the obtained PA and US images were analyzed offline in MATLAB 2021b using a Fourier-based image reconstruction algorithm[6], assuming a constant speed of sound of 1480 m/s. In experiment 5, imaging was done directly on the arm with a custom acoustic coupling pad (Cyberdyne Inc., Tsukuba, Japan).

Experiment 1 – Absorber concentration and depth effects

The first set-up investigated the influence of absorber depth and concentration. A fluoropolymer tube (Ø 3.2 mm) filled with ICG (Verdye) was placed in water with a distance from the US probe of 10, 15, 20, 25, 30 and 35 mm. PA images were obtained with a pulse width of 70 ns at all depths for four different ICG concentrations (3200, 320, 32, and 3.2 µmol/L).

Raw PA image data were reconstructed offline and 5120 frames were averaged for the analysis. The average PA signal ($\overline{m}$) and SNR (see Equation 9) were extracted for every measurement obtained with 820 nm light pulses. First, a region of interest (ROI) around the signal maximum was selected. Then, pixels representing the ICG signal were differentiated from the background using histogram thresholding (Otsu thresholding). A noise ROI was delineated adjacent to the signal ROI to get the standard deviation of the noise (σ) at the same distance from the signal at every depth. The size of the background and signal ROI were identical for all depths and concentrations. Average PA signal values were calculated for both 820 and 940 nm. Lastly, the ratio between the average PA signal strength at 940 and 820 nm was computed (see Equation 10).

$$SNR_{dB} = 10 * \log_{10}\left(\frac{\overline{m}_{signal}}{\sigma_{noise}}\right) \qquad [9]$$

$$Ratio_{940/820} = \frac{\overline{m}_{940nm}}{\overline{m}_{820nm}} \qquad [10]$$

Experiment 2 – Effect of frame averaging on image quality

With the second set-up, we studied the effect of averaging on the imaging performance in terms of SNR. Again, a tube filled with ICG (3200 μmol/L) was imaged at six depths. Frames were averaged 128, 256, 384, 640, 1280 and 2560 times and the SNR was computed for all frame averages at all depths. This leads to images with frame rates of 31.2, 15.6, 10.4, 6.3, 3.1, 1.6 Hz respectively using a PRF of 4 kHz.

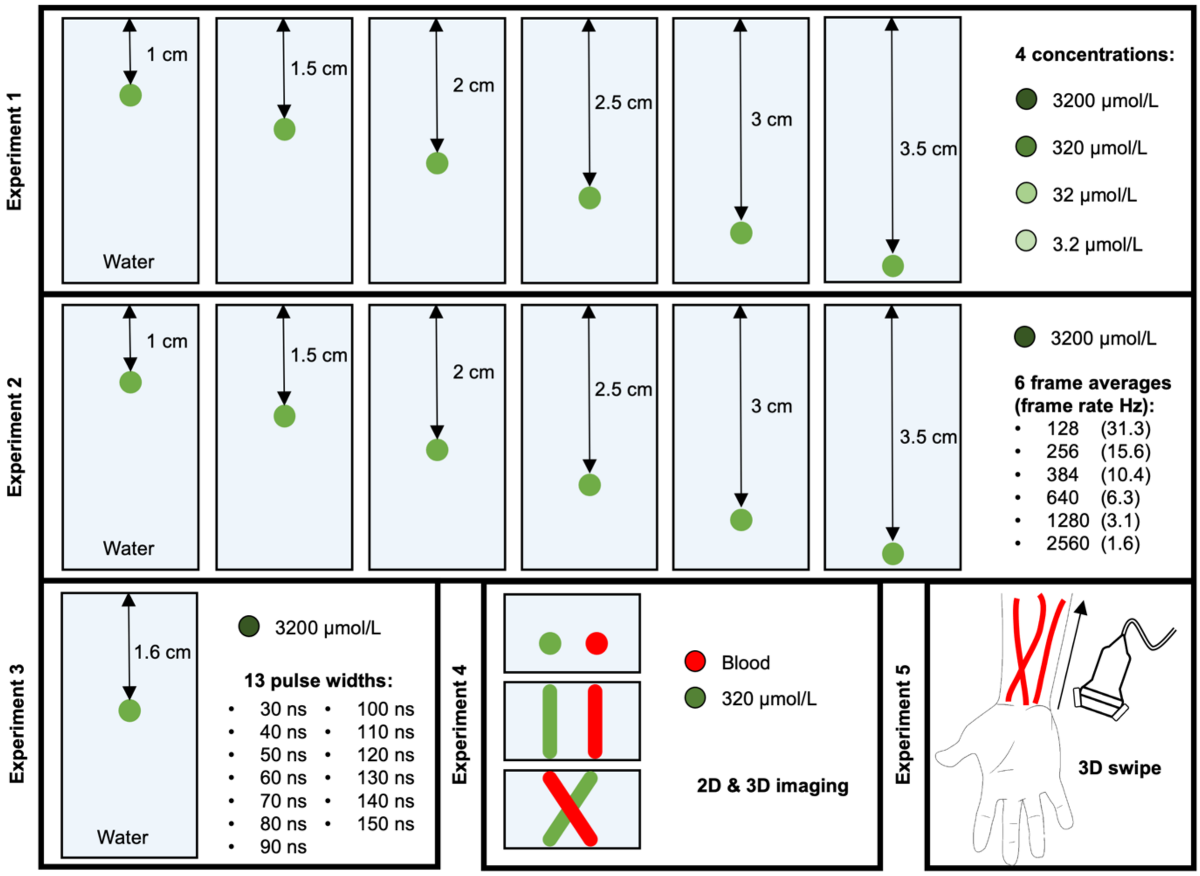

*Figure 3.4: Overview of the experimental set-ups. ICG is represented in green and blood in red. (**Experiment 1)** photoacoustic (PA) and ultrasonic (US) images were acquired of ICG filled tubes at six depths and with four concentrations. (**Experiment 2)** PA and US images were acquired of ICG filled tubes at six depths with six different frame rates. (**Experiment 3)** An ICG filled tube was imaged (PA + US) at a depth of 1.6 cm with thirteen different pulse widths. (**Experiment 4)** Two tubes, one filled with ICG and one with porcine blood, were images (PA + US) in 2D imaging mode (axial and parallel) and in 3D imaging mode with different configurations (tubes in parallel or crossed). (**Experiment 5)** In-vivo 3D imaging of the blood vessels of the volar forearm with and without skin-melanin surface suppression reconstruction.*

Experiment 3 – Effect of pulse width on image quality

The third experimental set-up consisted of one tube filled with ICG (3200 μmol/L) at 16.5 mm from the ultrasound probe surface. The middle element of the US probe was aligned to the tube. PA and US images were obtained with pulse widths ranging from 30 ns to 150 ns with increments of 10 ns. The obtained PA image frames were averaged 5120 times and average signal values were extracted from the PA image according to the methods described in experiment 1.

The raw PA signal at the element above the center of the tube was extracted and the fast Fourier transform was applied to the raw signal to investigate its frequency characteristics.

Experiment 4 – Proof of principle of simultaneous blood and ICG visualization

For the fourth experiment, one tube filled with ICG (320 µmol/L) and one tube with porcine arterial blood (Hb of 7.0 mmol/L) were imaged simultaneously running in parallel and crossed using 2D and 3D imaging mode. In 3D mode, sequential 2D imaging frames are acquired while sweeping the probe with a constant speed over the region of interest. This way a maximum intensity (MIP) projection image can be computed. The MIP is computed along the z-axis of the image by displaying the maximum pixel intensity along one line (e.g., per transducer element). The depth range was altered dynamically to select a depth region of interest between two z-planes and eliminate the influence of PA signals outside this region. A MIP can be computed for each wavelength separately and for the 940/820 ratio.

Experiment 5 – Surface suppression functionality

It is well known that melanin shows substantial light absorption in the near-infrared region and therefore results in a PA signal.[23] In 2D images, melanin in the skin can be distinguished from underlying superficial structures. However, a MIP of convex surfaces such as the arm, skin melanin signal can lead to contamination of the MIP, especially at the outer regions of the image. The Acoustic X has a built-in surface suppression functionality, where the surface in the image is detected based on the ultrasound image. A coupling gel to skin interface is easily distinguishable on US imaging. The user can dynamically suppress the PA signal from a set distance of the detected surface.[24]

This is also applicable for the MIP generation, where the surface suppressed data is not used for MIP computation. In this experiment, we obtained a handheld linear 3D scan of the volar forearm of a healthy volunteer. The blood vessels were visualized using a combined signal from 820 and 940 nm. MIPs were computed with and without surface suppression. For in-vivo image reconstruction, the speed of sound was set to 1540 m/s.

3.3 Results

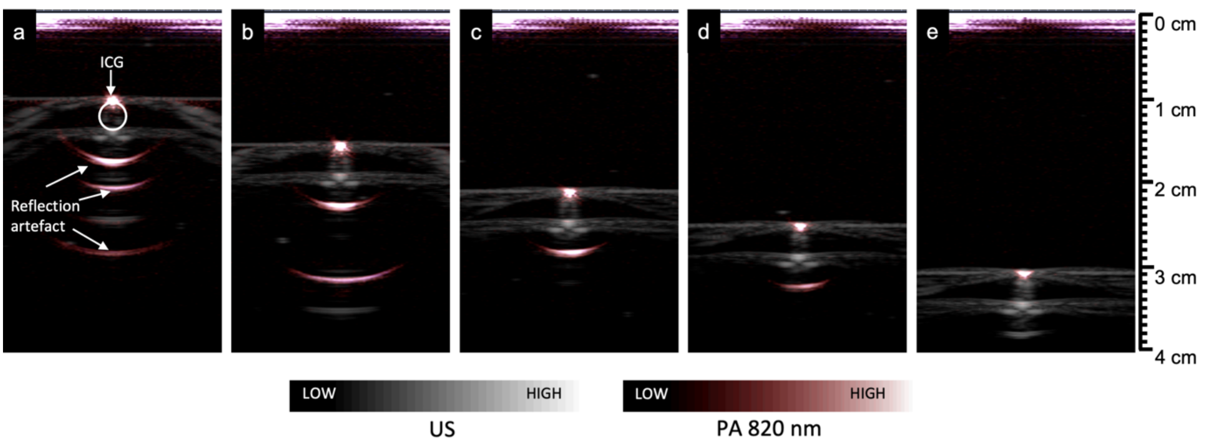

Figure 3.5: Combined photoacoustic (PA) and ultrasonic (US) images of ICG (320 µmol/L) at 10 mm (a), 15 mm (b), 20 mm (c), 25 mm (d) and 30 (mm) distance from the ultrasound probe surface (PA dynamic range: 25 dB and gain: 60 dB for all images).

Experiment 1 – Signal strength and SNR decrease with depth and absorber concentration

Figure 3.5 shows ultrasonic (grayscale) and photoacoustic (red) images of the ICG (320 µmol/L) filled tubes at different depths and Figure 3.6 shows the average PA signal and SNR dependence on depth for four different ICG concentrations. The average PA signal decreased exponentially with depth for all concentrations. Lower concentrations of ICG also produced lower PA signals, to the point where no signal could be distinguished from the background beyond 25 mm depth for a concentration of 3.2 µmol/L. The same effect was observed for the SNR, which is in line with the decrease of the PA signal, while the standard deviation of the noise remained constant. Table 3.1 shows the average PA signal values at both 820 and 940 nm and the corresponding ratio. The ratio ranged between 0.01 and 0.14 across all depths and concentrations.

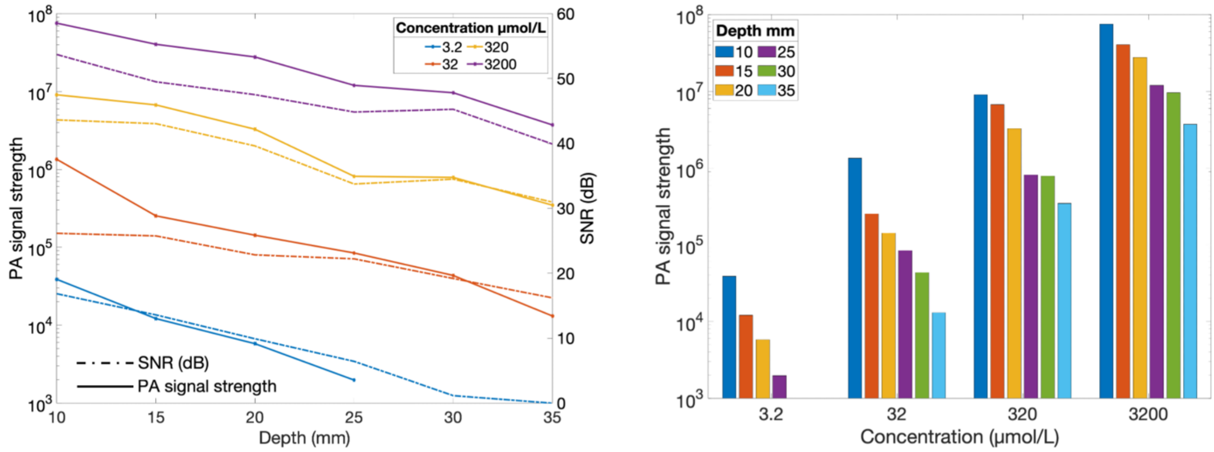

*Figure 3.6: **(left)** The photoacoustic signal strength and SNR$_{dB}$ at different depths and ICG concentrations @820 nm **(right)** bar plot of average PA signal strength at different depths and ICG concentrations.*

Table 3.1: Photoacoustic signal strength of ICG at 820 and 940 nm, and the 940/820 ratio for different ICG concentrations at different depths.

Concentration (µmol/L)	**Depth (mm)**	**Signal strength ($\overline{m}$) * 10^4**		**Ratio $\overline{m}_{940nm}$ / $\overline{m}_{820nm}$**
		820nm	940nm	
3.2	10	3.89	0.10	0.03
	15	1.22	0.05	0.04
	20	0.58	0.03	0.04
	25	0.20	0.02	0.10
	30	-	-	-
	35	-	-	-
32	10	134.71	1.22	0.01
	15	25.35	0.89	0.03
	20	14.29	0.72	0.05
	25	8.45	0.43	0.05
	30	4.35	0.23	0.05
	35	1.31	0.07	0.05
320	10	907.94	55.69	0.06
	15	673.52	49.79	0.07
	20	327.88	25.54	0.08
	25	81.59	6.58	0.08
	30	78.98	5.38	0.07
	35	34.74	2.50	0.07
3200	10	7549.30	1072.36	0.14
	15	4040.37	501.70	0.12
	20	2776.67	285.25	0.10
	25	1200.65	104.24	0.09
	30	964.90	68.86	0.07
	35	372.02	24.00	0.06

Experiment 2 – Image quality (SNR) improves with averaging

Figure 3.7 shows the SNR for different frame rates at six absorber depths. In concordance with results from experiment 1, the overall SNR decreased with depth, independent of the number of frame averages. The observed effect of the number of frame averages is the same at all depths, namely the SNR increased with higher number of frame averages. The pattern of SNR increase follows the theoretical pattern (black dotted line) given as a reference in the figure, where SNR improves with the square root of the number of frame averages.

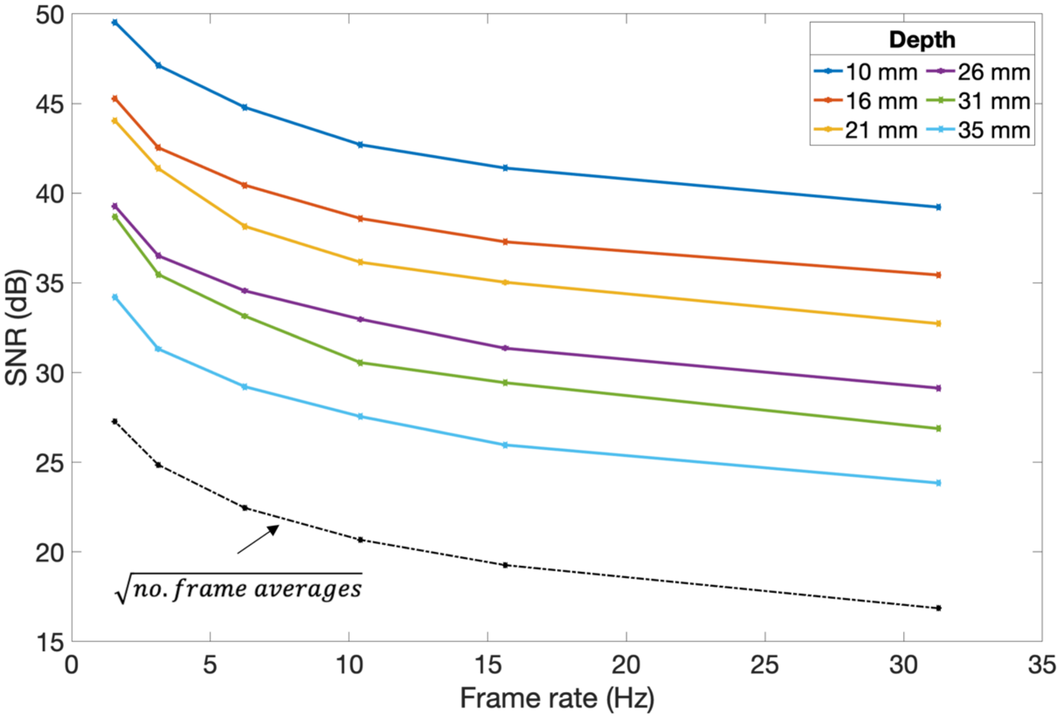

Figure 3.7: SNR dependence on frame rate for different depths. Black dotted line represents the square root of the number of frame averages.

Experiment 3 – Pulse width influences signal strength and spatial resolution

Figure 3.8 shows the average and maximum PA signal strength from the ICG absorber resulting from different light pulse widths. The magnitude of the PA signal initially increased with longer light pulses up to 70 ns. After that, PA signal strength stagnated and even decreased with pulse widths >110 ns.

Figure 3.9 shows the reconstructed PA signal at ultrasound probe element 64 (i.e., the element that detected the maximum signal). The PA signal shows a Gaussian-like shape that becomes wider with increased pulse width (i.e, larger full width half maximum (FWHM)). From 110 ns onwards, the signal starts to display two peaks instead of one, which results in two separable photoacoustic signals in the reconstructed image, even though there is a single absorber. The distance between the peaks also increased with pulse width, where the magnitude of the second peak was higher than the first peak. Lastly, Figure 3.10 displays the raw PA signal from ultrasound probe element 64 along with the corresponding frequency spectrum for different pulse widths. Indeed, the signal strength increased and widened with higher pulse widths, while the average signal strength decreased for pulse widths >110 ns. Apart from a slight decrease in high frequency content and the overall increase in spectrum magnitude, no substantial changes were observed in the frequency spectra from 30 – 70 ns. From 80 ns onwards, the contribution of higher frequencies starts to decrease even more with increased pulse widths. A significant change was observed between 100 and 110 ns, where the magnitude of the spectrum decreased strongly and two frequency peaks were visible instead of one. Both peaks shifted towards lower frequencies with higher pulse widths.

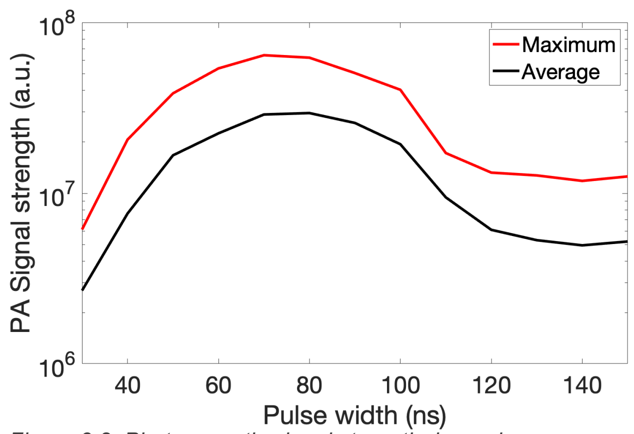

Figure 3.8: Photoacoustic signal strength dependence on pulse width

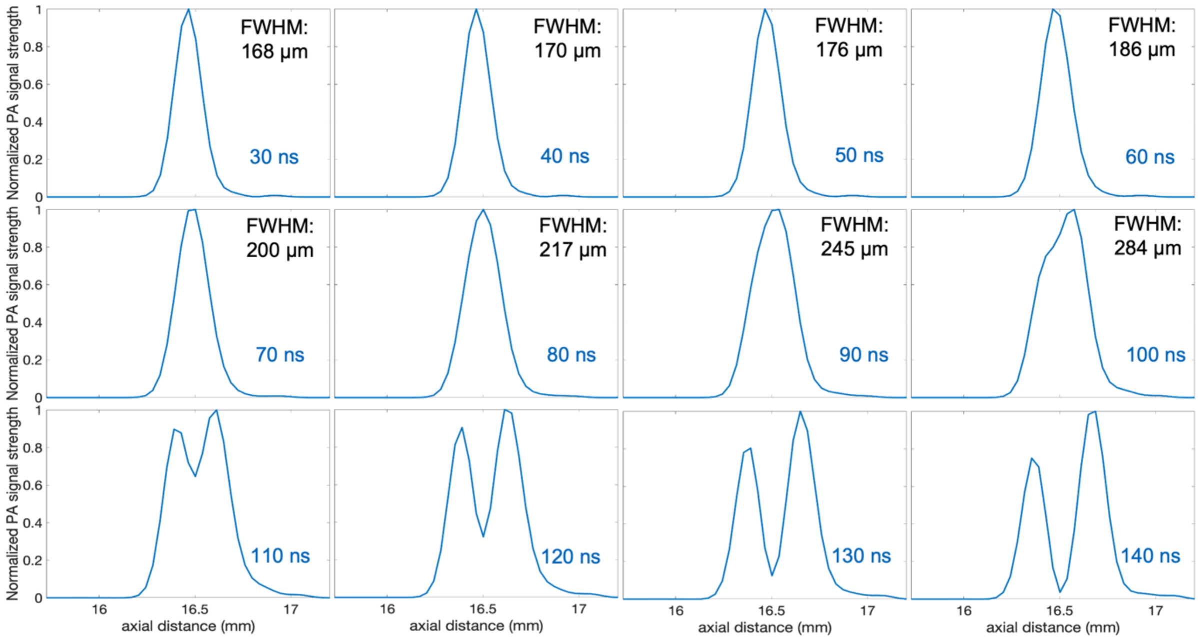

Figure 3.9: Reconstructed normalized photoacoustic signal at ultrasound probe element 64 for different pulse widths. FWHM: full width half maximum.

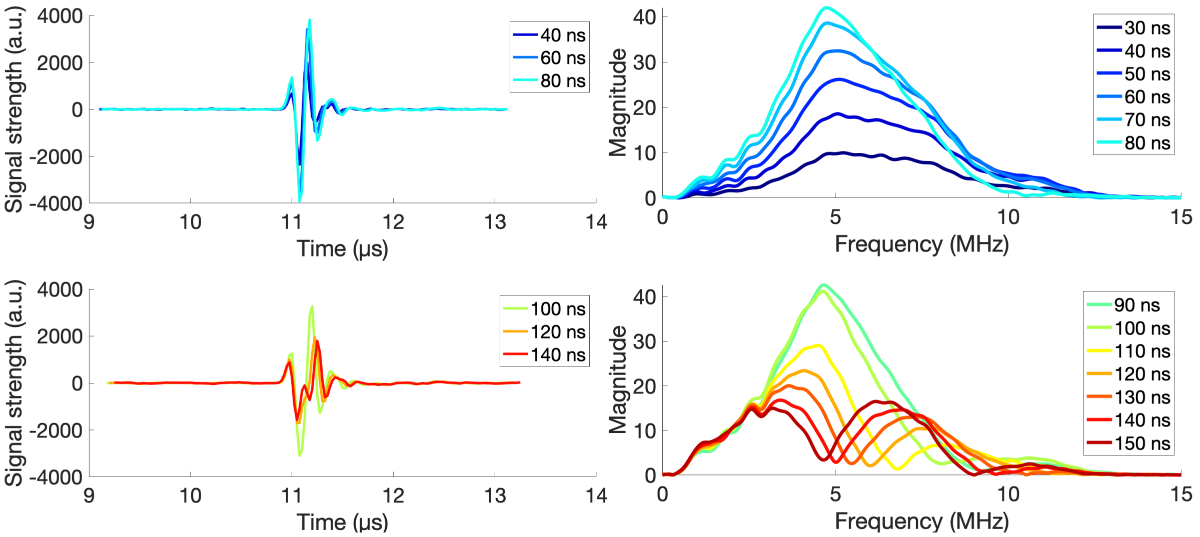

Figure 3.10: Raw temporal waveforms at ultrasound probe element 64 (left) and the corresponding magnitude of the Fourier transformation of the detected (right) for different pulse widths.

Experiment 4 – Proof of principle of simultaneous blood and ICG visualization

Figure 3.11 a-c shows 2D renderings of the PA image presented in a pseudo-color overlain on the US image in grayscale of an ICG filled channel in an ultrasound gel pad. The PA signal is visible at 820 nm and not at 940 nm, leading to a low 940/820 nm ratio clearly seen in blue in the image in panel c.

Figure 3.11 d shows the 940/820 nm ratio photoacoustic signal of blood and ICG in a tube. As expected, the blood signal resulted in a high ratio of ~1.3 (red) and a low ratio of ~0.05 (blue) for ICG. Reflection artefacts were observed below the tubes due to acoustic reflections at the tube surface interface.

Lastly, Figure 3.11 f-i shows MIP images obtained using the 3D mode of the device with two different configurations of blood and ICG filled tubes. The MIPs give a general overview of the relative locations of the absorbers. The images are displayed as the combined signal from 820 nm and 940 nm light pulses (e and f) and the 940/820 ratio (g and h). Blood and ICG are distinguishable in both images, where blood shows in purple and ICG in red in the 820 + 940 nm image. A more obvious difference was observed in the ratio image.

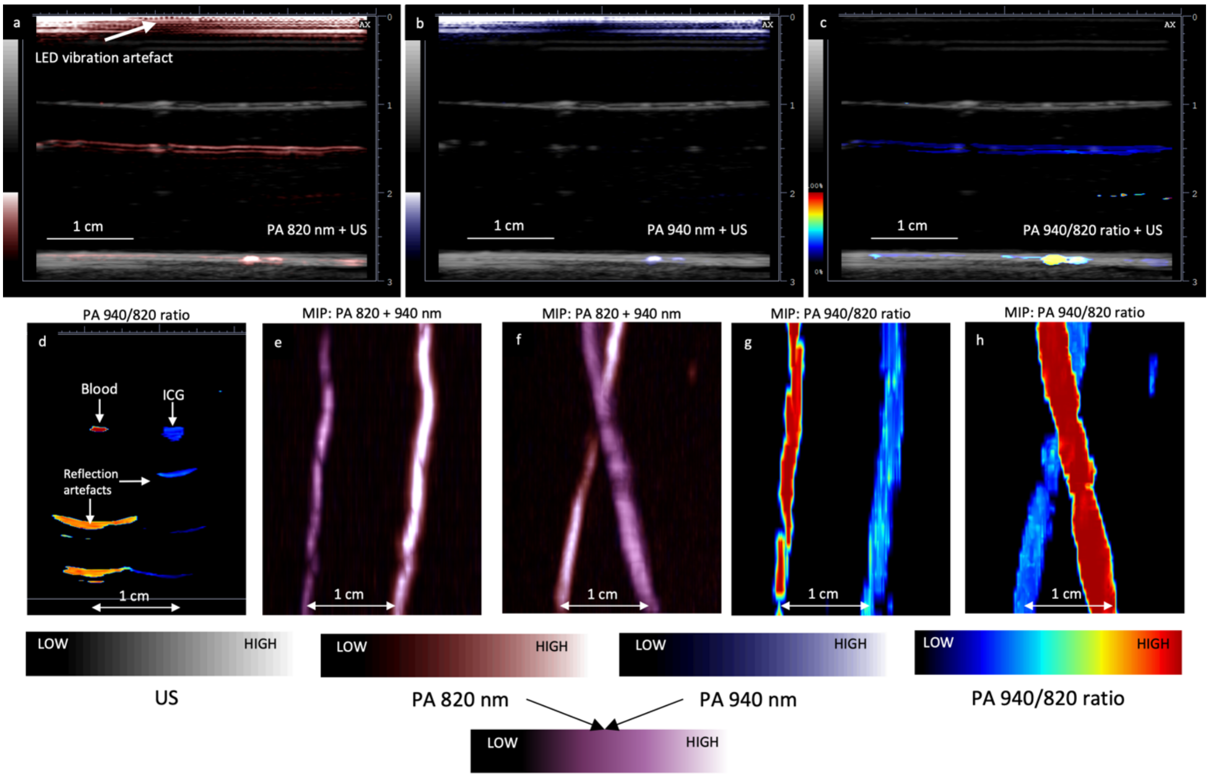

*Figure 3.11: Photoacoustic images of ICG and blood in a phantom. **(a, b, c)** Photoacoustic signal of a channel filled with 320 µmol/L ICG in an ultrasonic gel pad at 820 nm (a), 940 nm (b) and the 940/820 nm ratio (c). **(d)** Photoacoustic image of the 940/820 nm ratio of the cross section of one tube filled with porcine blood and one tube filled with 320 µmol/L ICG. **(e, f, g, h)** Maximum intensity projections of blood and ICG. e and f show the signal from 820 nm (red) and 940 nm (blue). Signal from both wavelengths shows in purple (red + blue). g and h show the 940/820 ratio with blood in red (high ratio) and ICG in blue (low ratio).*

Experiment 5 – Surface suppression

Figure 3.12 shows 2D renderings of one axial frame of a 3D swipe of superficial blood vessels in the volar forearm (a – c) and a MIP before (d) and after (e) skin-melanin surface suppression. In each 2D image frame, the PA image resulting from both 820 and 940 nm light pulses is presented in pseudo-color and superimposed on the background grayscale US image. The complete image (a) shows a clear signal from the skin surface (white arrow) and superficial blood vessels (red arrow). In the corresponding MIP the blood vessels can be depicted. However, skin signal shows up as a 'smeared' signal at several locations potentially covering signal from blood vessels directly underneath.

Surface suppression was done based on the detection of the skin surface in ultrasound (red line in panel b) and signal above the detected surface was removed (c), eliminating the skin surface signal as well as artefacts at the top of the image. Surface suppression eradicated the smeared appearance of the skin signal in the MIP image and more blood vessels were visible.

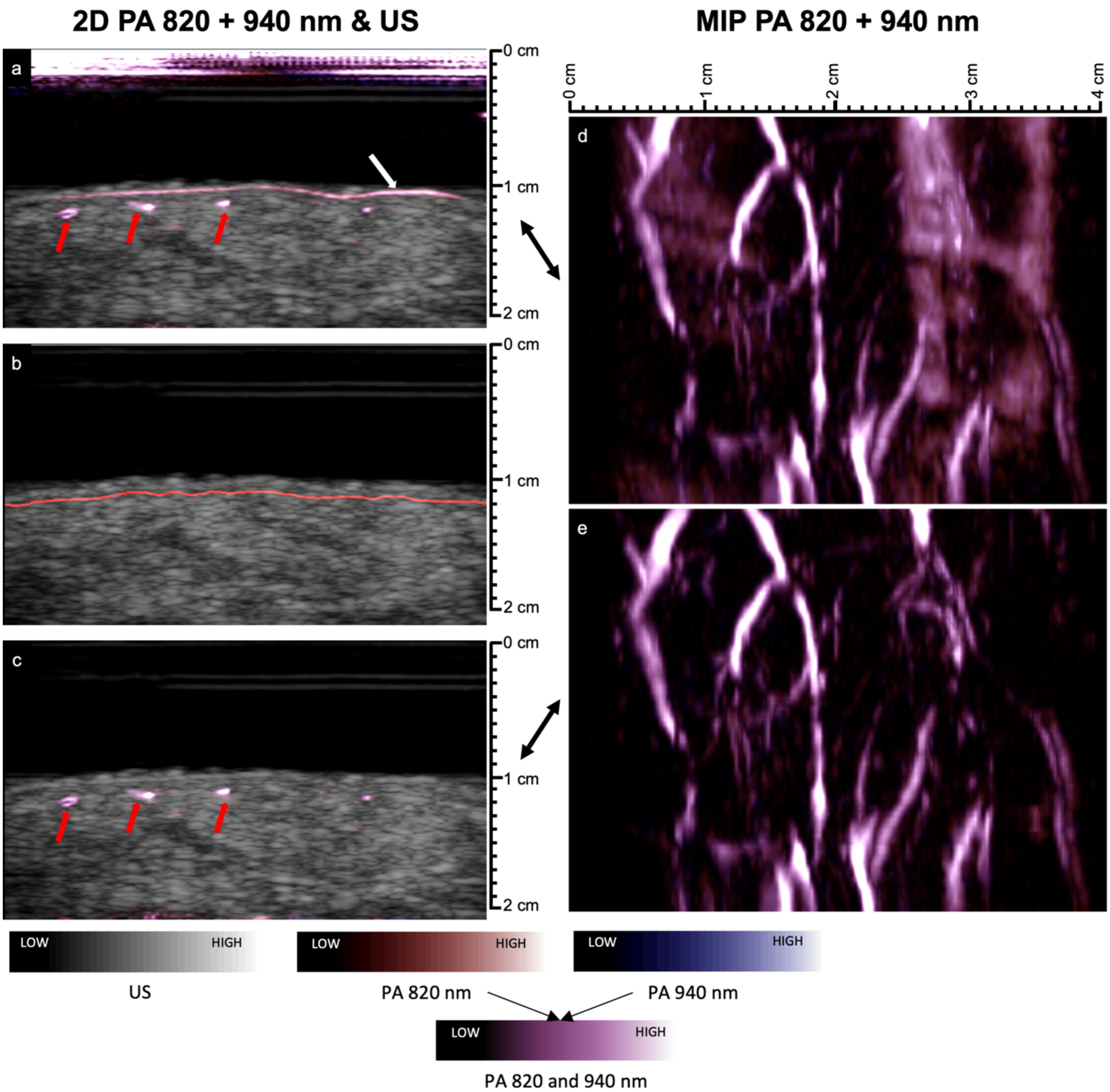

Figure 3.12: Photoacoustic (PA) and ultrasound (US) images of blood vessels in the volar forearm. ***(a)*** *Combined 2D axial photoacoustic and ultrasound image without surface suppression. Red arrows point to blood vessels and white arrows to the skin melanin signal.* ***(b)*** *Demonstration of the detected skin surface (red line) above which all photoacoustic signal is suppressed.* ***(c)*** *Combined 2D and photoacoustic image with surface suppression. Red arrows point to blood vessels.* ***(d)*** *Maximum intensity projection (MIP) without surface suppression corresponding to the 2D image in panel a.* ***(e)*** *Maximum intensity projection with surface suppression corresponding to the 2D image in panel c.*

3.4 Discussion

The experimental results in this chapter demonstrated the effect of several parameters on the magnitude and SNR of the obtained photoacoustic signal. We also demonstrated simultaneous ICG and blood visualization using dual-wavelength photoacoustic imaging. Lastly, we illustrated the advantages of skin surface signal suppression for the generation of MIPs.

Image quality decreases with absorber depth and concentration

Sufficient light depth penetration is important for medical applications and to visualize structures at greater depths. Results of the first experiment showed an exponential decrease of the photoacoustic signal amplitude with increased depth of the absorber along with the decrease in SNR (Figure 3.6). As stated in Equation 2, the magnitude of the photoacoustic signal is proportional to the product of the optical absorption coefficient and the light fluence. Indeed, the photoacoustic signal increases with higher ICG concentrations, but not completely linearly. This could be attributed to the nonlinear absorption behavior of ICG. The decrease of PA signal strength can be expected due to the decrease of light fluence with depth in combination with a decrease of the detected ultrasonic wave power with depth. Water is a homogeneous non-scattering medium with low optical absorption at the used wavelengths.[25] However, optical scattering will contribute significantly to the decrease in fluence with depth in-vivo and the optical penetration depth will therefore be limited in human tissues. Previous studies have imaged blood samples using LED light sources up to 2.2 cm in depth in chicken tissue at frame rates of 0.6 Hz and found that the detection limit of ICG is suitable for in-vivo imaging.[26,27]

The trade-off between SNR and real-time imaging

The main disadvantage of LED-based PAI is the substantially lower energy per pulse compared to laser-based systems. Previous research has shown that similar SNR is feasible with LED-based systems compared to laser-based systems if sufficient frame averaging is applied. The SNR generally increases with the square root of the number of frame averages, which is also the case in the present study independent of the depth.[16,27] However, there is a trade-off between the number of frame averages and the total frame rate. For clinical purposes, real-time image is often desired and a compromise between SNR and frame rate must be made. The final choice depends on the purpose of the imaging, whether a dynamic process is imaged, the strength of the absorber and the desired image depth. At greater depths, more averaging is needed to detect an object.[16]

Excitation light pulse width must be tuned to absorber size and US probe characteristics

The frequency response of detected PA signal is mostly a result of the frequency content of the light pulse, the bandwidth of the ultrasound probe and absorber size.[28,29] Short light pulses result in a wide range of frequency components in the acquired signal and lead to high resolution images. Although a wide band of frequencies is present, the signal is detected by a relatively narrow band ultrasound probe omitting the high frequencies in the detected signal. For this reason, the frequency spectrum does not change much in the range of 30 – 70 ns apart from the overall magnitude due to the higher fluence that is delivered per pulse leading to a higher signal.[26] It can therefore be argued that the shortest light pulse is not a necessity for good image resolution and one can opt for a higher pulse width to obtain a stronger signal. For pulse widths above 80 ns, the signal strength did not increase anymore and from 110 ns seconds two separable image peaks arose. This could be the result of the stress confinement not being met. The signal resulting from subsequent expansion and contraction become separable in time and create two signals in the photoacoustic image.[30] When this effect arises, depends on the size and acoustic properties of the absorber, which was constant during this experiment.

Against the expectation that fluence increases linearly with pulse width, the actual fluence decreased after 100 ns when using a PRF of 4 kHz due to electrical current capacities of the system, explaining the decrease in average signal intensity with pulse widths > 100 ns. It was also previously demonstrated that light pulses longer than 110 ns generate a non-Gaussian-like pulse shape, influencing the frequency content in the light pulse spectrum and therefore the detected signal.[28]

The final pulse width must therefore be tuned based on the properties of the ultrasound probe, imaging target, the desired resolution and signal strength. Corresponding to earlier studies, 70 ns seems the optimal pulse width for this device configuration[28,29], making imaging of absorbers > 108 μm possible.

Dual-wavelength photoacoustic imaging distinguishes between ICG and blood

Our phantom study demonstrated that simultaneous imaging of blood and ICG and that both absorbers are distinguishable based on the 940/820 ratio of the PA signal strength. It can be expected that the signal from both blood and ICG is higher in vivo due to changes in the absorption spectrum of ICG in human tissue due to binding to plasma proteins, leading to higher absorption at 820 nm.[10,11] Furthermore, the hemoglobin and hematocrit values are higher in humans than in pigs leading to a higher absorption coefficient.[31] The possibility of in-vivo LED-based imaging of the lymphatic vessels has already been demonstrated in a healthy volunteer.[22]

Reflection artefacts were observed due to large impedance differences at the tube wall interfaces. The generated photoacoustic wave is partially reflected, sometimes multiple times, leading to multiple artefacts. These artefacts arise at twice the distance of the location of the acoustic reflector since it is resolved as if the wavefront was formed during the initial light pulse.[32] The possibility of combined PA and US imaging aids in identifying reflection artefacts and its source.

It must be noted that distance measurements in the 3D swipe axis are not reliable since reconstruction is done based on the assumption that the US probe moved with a constant speed, which is not possible with handheld sweeps.

Surface suppression improves the quality of MIPs

MIPs provide a general overview of the absorber over a larger field of view compared to solely 2D images. We demonstrated the added value of (skin) surface suppression to generate better quality MIPs. This feature also holds potential for suppression of other interfering superficial signals such as dermal backflow signal in lymphedema imaging.

3.5 Conclusion

The experimental results in this chapter showed that dual-wavelength photoacoustic imaging at 820 and 940 nm makes it possible to distinguish between blood and ICG. Additionally, surface suppression features of the Acoustic X improved the quality of MIPs of blood vessels by removing the skin-melanin signal. With regards to imaging parameters, there is a trade-off between the frame rate and the image quality depending on the application and absorber characteristics and depth. Finally, 70 ns seems the optimal pulse width to capture the PA signal over the entire frequency range of the ultrasound probe used in this study while maintaining good image resolution and signal strength.

References

1 Kruger, R. A., Liu, P., Fang, Y. R. et al. Photoacoustic ultrasound (PAUS)—Reconstruction tomography. *Med. Phys.* 1995;(22):1605-1609, doi:10.1118/1.597429.

2 Wang, L. V. Tutorial on Photoacoustic Microscopy and Computed Tomography. *IEEE J. Sel. Top. Quant. Elec.* 2008;(14):171-179, doi:10.1109/JSTQE.2007.913398.

3 Lutzweiler, C. & Razansky, D. Optoacoustic imaging and tomography: reconstruction approaches and outstanding challenges in image performance and quantification. *Sensors (Basel).* 2013;(13):7345-7384, doi:10.3390/s130607345.

4 Yao, J. & Wang, L. V. Sensitivity of photoacoustic microscopy. *Photoacoustics.* 2014;(2):87-101, doi:10.1016/j.pacs.2014.04.002.

5 Rosenthal, A., Ntziachristos, V. & Razansky, D. Acoustic Inversion in Optoacoustic Tomography: A Review. *Curr. Med. Imaging Rev.* 2013;(9):318-336, doi:10.2174/15734056113096660006.

6 Jaeger, M., Schüpbach, S., Gertsch, A. et al. Fourier reconstruction in optoacoustic imaging using truncated regularized inverse k -space interpolation. *Inverse Probl.* 2007;(23):S51-S63, doi:10.1088/0266-5611/23/6/s05.

7 Köstli, K. P. & Beard, P. C. Two-dimensional photoacoustic imaging by use of Fourier-transform image reconstruction and a detector with an anisotropic response. *Applied Optics.* 2003;(42):1899-1908, doi:10.1364/AO.42.001899.

8 Kostli, K. P., Frauchiger, D., Niederhauser, J. J. et al. Optoacoustic imaging using a three-dimensional reconstruction algorithm. *IEEE J. Sel. Top. Quant. Elec.* 2001;(7):918-923, doi:10.1109/2944.983294.

9 Alander, J. T., Kaartinen, I., Laakso, A. et al. A Review of Indocyanine Green Fluorescent Imaging in Surgery. *Int. J. Biomed.* 2012;(2012):940585, doi:10.1155/2012/940585.

10 Desmettre, T., Devoisselle, J. M. & Mordon, S. Fluorescence Properties and Metabolic Features of Indocyanine Green (ICG) as Related to Angiography. *Surv. Ophthalmol.* 2000;(45):15-27, doi:10.1016/S0039-6257(00)00123-5.

11 Landsman, M. L., Kwant, G., Mook, G. A. et al. Light-absorbing properties, stability, and spectral stabilization of indocyanine green. *J. Appl. Physiol.* 1976;(40):575-583, doi:10.1152/jappl.1976.40.4.575.

12 Prahl, S. *Optical Absorption of Indocyanine Green (ICG)*, <https://omlc.org/spectra/icg/> (2018) Accessed 20-08-2021.

13 Zhong, H., Duan, T., Lan, H. et al. Review of Low-Cost Photoacoustic Sensing and Imaging Based on Laser Diode and Light-Emitting Diode. *Sensors (Basel).* 2018;(18):2264, doi:10.3390/s18072264.

14 Xia, W., Kuniyil Ajith Singh, M., Maneas, E. et al. Handheld Real-Time LED-Based Photoacoustic and Ultrasound Imaging System for Accurate Visualization of Clinical Metal Needles and Superficial Vasculature to Guide Minimally Invasive Procedures. *Sensors (Basel).* 2018;(18):1394, doi:10.3390/s18051394.

15 Sivasubramanian, K. & Pramanik, M. High frame rate photoacoustic imaging at 7000 frames per second using clinical ultrasound system. *Biomed. Opt. Express.* 2016;(7):312-323, doi:10.1364/BOE.7.000312.

16 Agrawal, S., Kuniyil Ajith Singh, M., Johnstonbaugh, K. et al. Photoacoustic Imaging of Human Vasculature Using LED versus Laser Illumination: A Comparison Study on Tissue Phantoms and In Vivo Humans. *Sensors.* 2021;(21):424.

17 Zhang, H., Zhang, G., Zhang, Y. et al. Quantitatively assessing port-wine stains using a photoacoustic imaging method: A pilot study. *J. Am. Acad. Dermatol.* 2021;(S0190-9622):33183-33182, doi:10.1016/j.jaad.2020.12.024.

18 Jo, J., Xu, G., Zhu, Y. et al. Detecting joint inflammation by an LED-based photoacoustic imaging system: a feasibility study. *J. Biomed. Opt.* 2018;(23):110501.

19 Zhu, Y., Xu, G., Yuan, J. et al. Light Emitting Diodes based Photoacoustic Imaging and Potential Clinical Applications. *Sci. Rep.* 2018;(8):9885, doi:10.1038/s41598-018-28131-4.

20 Jo, J., Xu, G., Schiopu, E. et al. Imaging of enthesitis by an LED-based photoacoustic system. *J. Biomed. Opt.* 2020;(25):126005.

21 Lillis, A. P. & Krishnamurthy, R. Photoacoustic Imaging Addresses a Long-standing Challenge in Lymphedema. *Radiology.* 2020;(295):475-477, doi:10.1148/radiol.2020192824.

22 Kuniyil Ajith Singh, M., Agano, T., Sato, N. et al. Real-time in vivo imaging of human lymphatic system using an LED-based photoacoustic/ultrasound imaging system. *SPIE BiOS.* 2018:3-3, doi:10.1117/12.2290871.

23 Jacques, S. *Melanosome Absorption Coefficient*, <https://omlc.org/spectra/melanin/mua.html> (1998) Accessed June 2021.

24 Kuniyil Ajith Singh, M., Sato, N., Ichihashi, F. et al. Real-time improvement of LED-based photoacoustic image quality using intermittent pulse echo acquisitions. *SPIE BiOS.* 2020;(11240).

25 Li, M., Tang, Y. & Yao, J. Photoacoustic tomography of blood oxygenation: A mini review. *Photoacoustics.* 2018;(10):65-73, doi:10.1016/j.pacs.2018.05.001.

26 Hariri, A., Lemaster, J., Wang, J. et al. The characterization of an economic and portable LED-based photoacoustic imaging system to facilitate molecular imaging. *Photoacoustics.* 2018;(9):10-20, doi:10.1016/j.pacs.2017.11.001.

27 Joseph, J., Ajith Singh, M. K., Sato, N. et al. Technical validation studies of a dual-wavelength LED-based photoacoustic and ultrasound imaging system. *Photoacoustics.* 2021;(22):100267, doi:10.1016/j.pacs.2021.100267.

28 Agano, T., Kuniyil Ajith Singh, M., Nagaoka, R. et al. Effect of light pulse width on frequency characteristics of photoacoustic signal-an experimental study using a pulse-width tunable LED-based photoacoustic imaging system. *Int. J. Eng. Technol.* 2018;(7):4300-4303, doi:10.14419/ijet.v7i4.19907.

29 Sato, N. & Agano, T. Comparative experiments of photoacoustic system using laser light source and LED array light source. *Proc. SPIE.* 2015, doi:10.1117/12.2077357.

30 Gao, F., Feng, X., Zhang, R. et al. Single laser pulse generates dual photoacoustic signals for differential contrast photoacoustic imaging. *Sci. Rep.* 2017;(7):626, doi:10.1038/s41598-017-00725-4.

31 Nederlandse Vereniging voor Klinische Chemie en Laboratoriumgeneeskunde. *Algemeen overzicht referentiewaarden*, <https://www.nvkc.nl/algemeen-overzicht-referentiewaarden> (Accessed June 2021.

32 Kuniyil Ajith Singh, M., Jaeger, M., Frenz, M. et al. Photoacoustic reflection artifact reduction using photoacoustic-guided focused ultrasound: Comparison between plane-wave and element-by-element synthetic backpropagation approach. *Biomed. Opt. Express.* 2017;(8):2245-2260, doi:10.1364/BOE.8.002245.

4

Preliminary experience with LED-based photoacoustic imaging of the lymphatic vessels in patients with secondary lymphedema

Abstract

This chapter describes the preliminary findings of a clinical feasibility study on LED-based photoacoustic imaging (PAI) of the lymphatic vessels in patients with secondary limb lymphedema. The purpose of this study was to explore visualization of the lymphatic vessels and veins with LED-based PAI in secondary limb lymphedema. We also investigated if lymphatic vessel contractions could be seen and if lymphatic vessels could be depicted behind dermal backflow (DBF) patterns.

Near-infrared fluorescence lymphography (NIRF-L) was done according to the standard imaging protocol using subcutaneous injections of indocyanine green (ICG). Based on NIRF-L findings, we indicated multiple locations of lymphatic vessels on the healthy and affected limb, with and without the presence DBF. Subsequently, PAI was done in these locations and successful vessel depiction was determined.

Three patients with breast-cancer related arm lymphedema were included in the study to date. Patients presented with variable clinical and NIRF-L severity stages. We showed that this novel technique of handheld dual-wavelength PAI is not more invasive than NIRF-L. We demonstrated that dual-wavelength, LED-based PAI can visualize lymphatic and blood vessels even in the presence of DBF. These findings suggest that PAI has potential for pre-operative lymphedema assessment, especially in cases with extensive DBF pattern hindering assessment with NIRF-L. Further research is needed to confirm these preliminary findings and demonstrate if handheld LED-based PAI can visualize lymphatic vessel contractions.

4.1 Introduction

As described in Chapter 1, secondary lymphedema is a common complication after surgical and radiotherapeutic treatment of cancer. It is associated with severe discomfort and has a major impact on the quality of life of patients.[1] Microsurgical lymphovenous bypass (LVB) surgery is increasingly used when conventional treatments such as manual lymphatic drainage and compression garment therapy are not sufficient.[2-5] Surgeons need pre-operative visualization of the lymphatic vessels to determine potential anastomosis sites.

The systematic literature review in Chapter 2 emphasized the importance of adequate imaging for surgical decision making and showed the heterogeneity of imaging modalities used for lymphatic vessel imaging. Near-infrared fluorescence lymphography (NIRF-L) has become popular for pre-operative evaluation and facilitates visualization of the lymphatic tracts and dermal backflow (DBF) in real-time using indocyanine green (ICG) contrast.[6-8] Functional lymphatic vessels, which are suitable anastomosis sites, would appear as linear structures, preferentially with visible pulsatility. However, NIRF-L has low resolution and cannot provide depth information, causing suboptimal decision making in case of extensive DBF patterns.[9-13] Photoacoustic imaging (PAI), specifically with LEDs as the light pulse generator, is a novel technique that has properties that may overcome the problems faced with NIRF-L.[14,15]

Findings from phantom experiments in Chapter 3 showed the potential of dual-wavelength LED-based PAI for the differentiation between ICG and hemoglobin in blood using the ratio between the PA signal generated with 940 nm and 820 nm light pulses. This is possible due to the pronounced differences in optical absorption properties of ICG and hemoglobin in blood. The 940/820 nm ratio might therefore be useful for in-vivo imaging of the lymphatic vessels and veins for surgical decision making in the treatment of secondary lymphedema.

The purpose of this study was to explore the feasibility of LED-based PAI for visualization of the lymphatic vessels and veins in secondary lymphedema with the aim of improving pre-operative imaging for LVB surgical planning. This means that if the acquired images are of sufficient quality and contain the information needed to determine the anastomosis sites. This consists of the identification of at least the lymphatic vessels observed with NIRF-L and additionally the identification of veins that can serve as the acceptor site for anastomosis. We also investigated novel features such as visualization of lymphatic vessel contractions and lymphatic vessels depiction in the presence of dermal backflow (DBF).

4.2 Methods

4.2.1 Patient population

A prospective feasibility study of LED-based PAI in patients with secondary limb lymphedema was conducted in November of 2021 at the Erasmus MC, University Medical Hospital Rotterdam. A total of 3 patients referred to the plastic- and reconstructive surgery department for (potential) microsurgical treatment of secondary limb lymphedema as a result of cancer treatment were included in the study to date. Exclusion criteria included iodine allergy, pregnancy, incapacity or bilateral lymphedema. If NIRF-L was not possible or failed, the patient was also excluded. All patients gave their written informed consent before participation.

Patients were assessed in the outpatient clinic, followed by imaging on the same day. Demographics were collected including body mass index (BMI), age, surgical cancer treatment, radiation therapy, (neo)adjuvant chemotherapy, self-reported time since onset of lymphedema and in case of breast cancer, hormonal therapy. Patients were staged according to the international society of lymphedema (ISL) grading system by an experienced plastic surgeon.[16] Circumference differences between the affected and healthy limb were measured on five different levels of the arm: mid of the palm of the hand, wrist, location on the forearm with maximum symptomology, elbow and location on the upper arm with maximum symptomology.

4.2.2 Medical device classification and ethics approval

This study was approved by the medical research ethics committee (MREC) of the Erasmus MC, University Medical Center Rotterdam (NL78365.078.21). The PAI device under investigation in this study (Acoustic X, Cyberdyne Inc., Tsukuba, Japan) falls under the definition of a non-CE marked medical device as stated in Article 2, paragraph 1 of the Medical Device Regulation (MDR) (EU) 2017/745: “Any apparatus intended by the manufacturer to be used, alone or in combination, for human beings for diagnosis, prevention, monitoring, prediction, prognosis, treatment or alleviation of disease.” It also does not achieve its principal intended action by pharmacological, immunological or metabolic means, in or on the human body.[17]

Furthermore, the device was classified according to the MDR (EU) 2017/745, Annex VIII, Chapter I:

(1) the device is intended for transient use (paragraph 1.1) and

(2) the device is not invasive or implantable. It is an active device intended for diagnosis or monitoring, it supplies information for detecting, diagnosing, monitoring or treating physiological conditions, states of health, illnesses or congenital deformities and is powered by electricity.

Further classification of active devices according to the MDR (EU) 2017/745, Annex VIII, Chapter III, paragraph 6 was done. Paragraph 6.2, rule 10 states[17]:

- The device is intended for diagnosis and monitoring and supplies energy which will be absorbed by the human body (optical and acoustic) outside the visible spectrum.
- The device can also image in vivo distribution of radiopharmaceuticals (e.g., indocyanine green).
- It is not intended for diagnosis or monitoring of vital physiological processes.
- It does not emit ionizing radiation

The Acoustic X was therefore classified as a Class IIa medical device. The entire MREC application process is presented in Appendix II. Final approval was received in October of 2021.

4.2.3 Imaging protocol

Anamnesis, physical examination, NIRF-L and PAI took place on the same day in an outpatient clinic setting. First, NIRF-L images were acquired directly after ICG injection for a total duration of approximately 30 minutes followed by PAI. Surgical decision making was based on NIRF-L findings.

Near infrared fluorescence lymphography

NIRF-L images were acquired using the Photodynamic Eye infrared camera system (Hamamatsu Photonics K.K., Hamamatsu, Japan).[8] Prior to imaging ~0.2 mL ICG (0.25% Verdye) was injected subcutaneously into all interdigital spaces of the affected limb and 2nd and 3rd interdigital spaces of the unaffected limb. Injection sites were covered with adhesive bandages to prevent image saturation. Directly after injection, fluorescence videos and images were obtained of the entire limb following the ICG flow and patterns. The images were classified according to the MD Anderson Cancer Center (MDACC) severity scale by the same plastic surgeon that collected the medical background and physical examination data.[18] Locations of observed linear pattern were indicated with a marker on both the healthy and affected limb as a control. Moreover, at least one location where a linear pattern transitioned into dermal backflow was also marked.

Photoacoustic imaging

Combined ultrasound (US) and PAI data were acquired immediately following NIRF-L. This protocol ensured that no additional ICG injections were necessary. Patients were imaged with the LED-based PAI system, Acoustic X (Cyberdyne Inc., Tsukuba, Japan) operating with an ultrasound transducer (7 MHz) and two high-density LED arrays intermittently emitting light at 820 and 940 nm, with a pulse repetition frequency of 4 kHz and a pulse width of 70 ns. We used a custom-made coupling pad spacer for acoustic coupling. Figure 4.1 shows images of the device and the setup. The obtained image frames were averaged 640 times, resulting in a frame rate of 6.25 Hz. We acquired both 2D (axial and parallel) and 3D images at multiple sites on the arm. 3D images were obtained by manually moving the probe with a linear motion over the region of interest. Subsequently we imaged lymphatic vessels continuously for 2 min at same location to potentially observe vessel contractions.

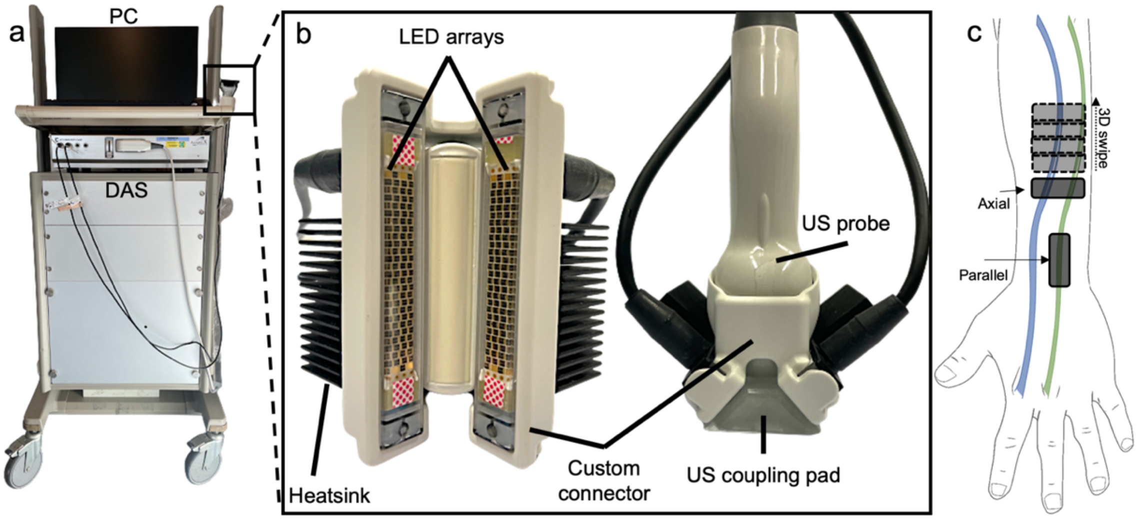

*Figure 4.1: **(a)** The Acoustic X system on a medical trolley. The system consists of a PC, data acquisition system (DAS), the ultrasound (US) probe and the light-emitting diode arrays (LEDs). The US probe and LEDs are connected to the DAS. **(b)** The LEDs are attached to the US probe with a custom connector. The custom US coupling pad is used for acoustic coupling with the imaged surface. **(c)** Schematic of different probe orientation used in this study for 2D and 3D data acquisition.*

4.2.4 Data processing

Patient demographics are reported using means and standard deviation. We analyzed the NIRF-L videos and obtained snapshots of the locations subsequently imaged with PAI. Image findings are reported per patient.

US and PA images were reconstructed using a built-in Fourier based reconstruction software of the device using a sampling rate of 20 and 40 MHz for US and PA, respectively.[19] US images are displayed in grayscale and PA images in a pseudo color displayed superimposed on the US images. The first centimeter from the PA image was suppressed in the final visualization since it only contains artefacts due to PA signal generated by the vibrations of the LEDs. PA images resulting from 820 nm, 940 nm, 820 and 940 nm combined or the 940/820 nm ratio can be displayed. Since the light pulse energy is higher for 820 nm (128 µJ) compared to 940 nm (114 µJ), the PA image signal from 940 is multiplied by a factor 1.12 before the 940/820 nm ratio is calculated to compensate for the pulse energy differences. From the 3D swipes, both the 2D axial slices as well as the maximum intensity projections (MIPs) were generated and assessed. MIPs were created using both the 820 nm (ICG dominant) and 940 nm (blood dominant) signals and displayed superimposed in one image. Vessel detected was considered successful if a lymphatic vessel was visible for a couple of seconds in axial images. Parallel images were considered successful if the path of a vessel could be followed for more than 3 mm. If possible, the depth and diameter of the detected lymphatic vessels and veins were measured using a built-in measurement function of the PA device on the 820 nm PA images.

4.3 Results

4.3.1 Patient characteristics

A total of 3 female subjects with secondary arm lymphedema resulting from breast cancer treatment were included in this study. Clinical severity for the three patient was ISL stage I, stage II and stage II-III lymphedema. Average

age and BMI were 50 ± 3.6 years and 25.7 ± 5.3 kg/m^3, respectively. The mean time since self-reported onset was 55.3 ± 22.3 months before their visit. Table 4.1 provides the detailed patient characteristics.

Table 4.1: Patient characteristics

Patient number	**1**	**2**	**3**
Sex	F	F	F
Age (years)	52	53	45
BMI (kg/m^3)	23.6	32.9	20.5
Cancer type	Breast	Breast	Breast
Duration (months)	80	60	26
Localization	Left arm	Left arm	Left arm
Surgery	Mastectomy ALND	Lumpectomy SLNB	Lumpectomy ALND LVB
LVB indicated?	+	-	-
Radiotherapy	+	+	+
Chemotherapy	Adjuvant	Adjuvant	Adjuvant
ISL stage	II-III	II	I
Limb circumference differences (% (range))	12.0 (6.3 – 15.9)	2.5 (0.0 – 7.1)	2.7 (0.0 – 6.8)

ALND: axillary lymph node dissection; LVB: lymphovenous bypass; SLNB: sentinel lymph node biopsy.

4.3.2 Imaging results

Table 4.2 and Table 4.3 give an overview of the NIRF-L and PAI findings for all patients and findings for each individual patient are discussed below. We acquired NIRF-L images directly after ICG injection for a total duration of ~30 min. PA image acquisition was done 35 – 45 minutes after ICG injection. The entire PAI protocol took between 30 – 40 minutes.

Lymphatic and blood vessels were imaged with axial and parallel orientation of the probe. Both vessel types were observed up to 5 mm depth from the skin surface in at least one location in all patients. Overall, axial orientation of the probe produced more images in which lymphatic and blood vessels were identifiable. Imaging with a parallel orientation resulted in fewer lymphatic vessels observed. In both cases with DBF, lymphatic and blood vessels were successfully depicted.

Table 4.2: MDACC staging of NIRF-L and number of PAI images that resulted in vessel detection

Case number	**NIRF-L stage**	**PAI lymphatic vessel**		**PAI blood vessel**		**PAI vessel observed behind DBF**
		Axial	Parallel	Axial	Parallel	
1	II-III	3/4	1/4	4/4	1/4	+
2	0	3/4*	1/4*	4/4	4/4	No DBF present
3	II	3/3	2/3	3/3	3/3	+
Total		81%	36%	100%	73%	

*NIRF-L: near-infrared fluorescence lymphography; MDACC: MD Anderson Cancer Center; PAI: photoacoustic imaging; DBF: dermal backflow. * In one of the four locations, no ICG signal was seen with NIRF-L.*

Table 4.3: Observed depth of lymphatic and blood vessels

Case	**Lymphatic vessel** *Depth (mm)*	**Blood vessel** *Depth (mm)*
1	1.8 – 3.5	2.0 – 4.9
2	0.7 – 2.2	1.0 – 4.8
3	1.9 – 5.0	1.1 – 4.0
Average	2.2 ± 0.9	2.4 ± 1.2

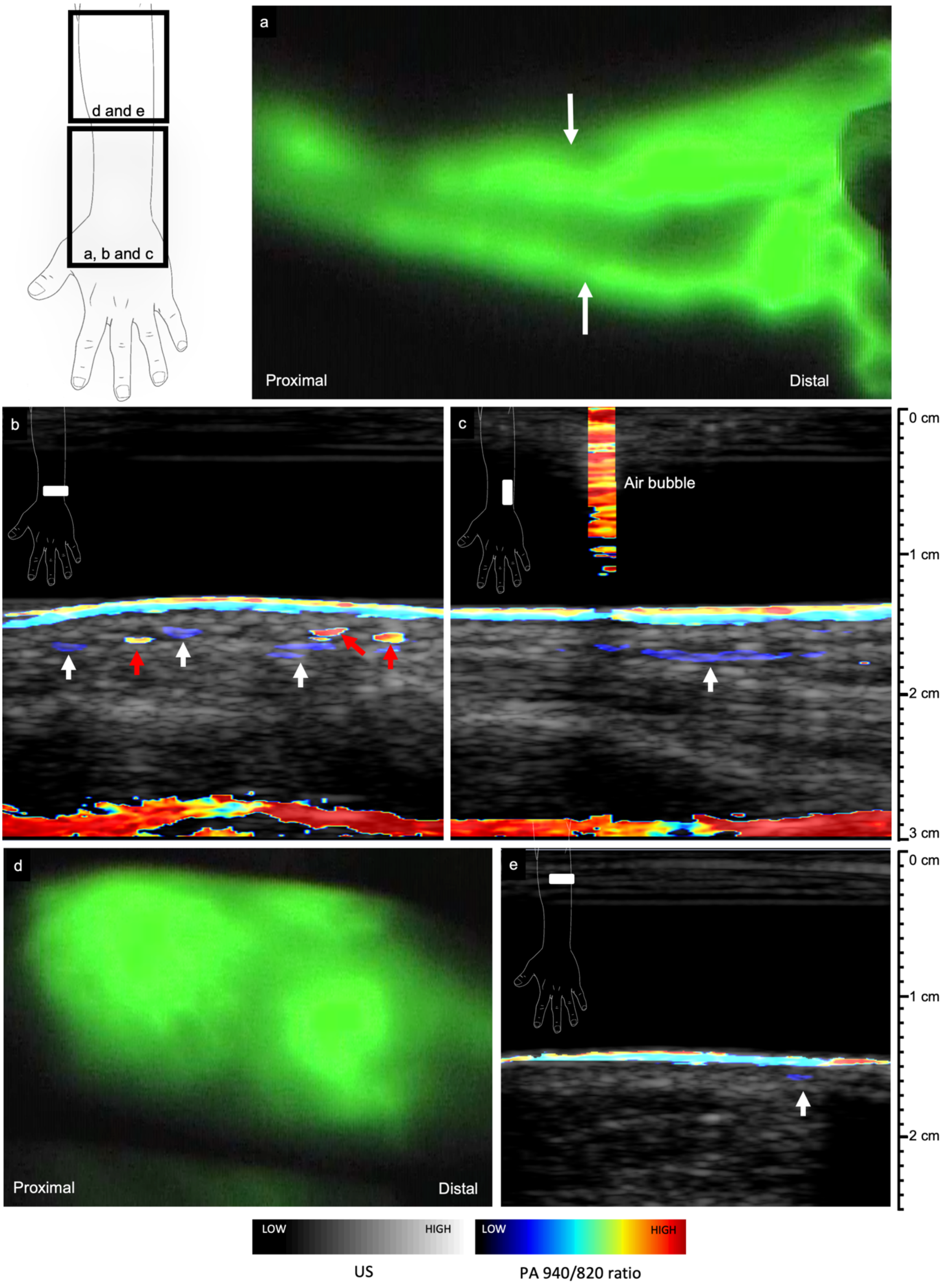

Figure 4.2: Near infrared fluorescence lymphography (NIRF-L) and 940/820 nm ratio photoacoustic (PA) and ultrasound images of a lymphedema arm (patient 1). White arrows indicate lymphatic vessels and red arrows indicate blood vessels. ***(a)*** *NIRF-L image of the dorsal wrist showing two patent lymphatic vessels (linear pattern).* ***(b)*** *Axial PA image slice of the dorsal wrist. Multiple lymphatic vessels (dark blue) and veins (dark red) are visible.* ***(c)*** *Parallel PA image slice of the dorsal wrist. A lymphatic vessel (dark blue) is clearly visible.* ***(d)*** *NIRF-L image of the dorsal forearm showing dermal backflow.* ***(e)*** *Axial PAI image slice of the dorsal forearm at a location with DBF observed with NIRF-L. A lymphatic vessel is visible (white arrow).*

Case 1

The first patient was a 52-year-old female with breast cancer related lymphedema of the left arm. NIRF-L showed clear uptake of ICG in two lymphatic vessels on the dorsal forearm directly after injection. At approximately 4 cm from the wrist a DBF pattern was seen. Another lymphatic vessel was observed on the volar forearm around the elbow, also contributing to DBF. We acquired PA images on the dorsal wrist (ulnar side) where the linear NIRF-L pattern was seen and at the border of the DBF pattern. NIRF-L of the healthy arm showed a clear linear pattern (two lymphatic vessels) over the entire length of the dorsal forearm. We also acquired PA images at the same locations on the affected arm. Based on the NIRF-L findings, the patient was scheduled for LVB surgery.
Figure 4.2 shows the NIRF-L (panel a) and PA images (panel b and c) of the affected arm on the location where a linear pattern was seen with NIRF-L. All PAI images show clear signal at the skin surface from melanin in light blue. In some cases, an additional red layer was seen above the skin melanin layer, originating from the coupling pad to ultrasound gel interface. Axial PA images (panel b) show three lymphatic vessels and multiple blood vessels in one slice, even though only two lymphatic vessels were observed with NIRF-L in this area. We also visualized a lymphatic vessel lengthwise (panel c) but no contractions were observed. Lymphatic vessels could also be depicted with the presence of DBF (panel e).

Case 2

The second patient also suffered from arm lymphedema because of breast cancer treatment. Even though the patient had symptoms, NIRF-L did not show abnormal flow patterns. Multiple lymphatic vessels were seen in both the lymphedema arm as well as the unaffected arm. Based on these findings, LVB was not indicated and the patient continued conventional treatment. We acquired PAI on the dorsal forearm and in the fold of the elbow of both arms (no NIRF-L signal was seen in the elbow fold on the healthy arm). Axial images visualized lymphatic and blood vessels in all locations where lymphatic vessels were also observed with NIRF-L. Again, it was more challenging to obtain images along the length of the vessel. Figure 4.3 shows PA images from these measurements together with a MIP resulting from a 3D swipe of the dorsal forearm.

Case 3

The third patient was a 45-year-old female who had already undergone LVB surgery (3 anastomoses; two in the dorsal wrist and one in the elbow fold) fourteen months before these post-surgical images were obtained. NIRF-L showed patent lymphatic vessels and functioning anastomoses in the dorsal wrist, quickly followed by DBF patterns in the lower arm. At the end of the NIRF-L imaging session the entire limb was covered with DBF and the lymphatic vessels were not visible anymore. No additional lymphatic vessels were observed that could serve as an anastomosis site.
During PAI of the healthy arm, we massaged the hand and arm to stimulate lymphatic flow and potentially increase the chance of finding a lymphatic vessel. Figure 4.4 shows the NIRF-L and PAI images of both the affected an unaffected arm. Lymphatic vessels and veins were visible even though DBF was present over the entire imaging surface (panel b and d). Additionally, we imaged a lymphatic vessel over the entire length of the US probe on the healthy arm for 2 consecutive minutes. No obvious lymphatic vessel contractions were visible in these recordings. In these images, we were not able to identify a contrast that could be assigned to DBF. No differences were seen between the superficial (skin-melanin) signal in locations where DBF was observed with NIRF-L, compared to locations without DBF on the healthy arm.

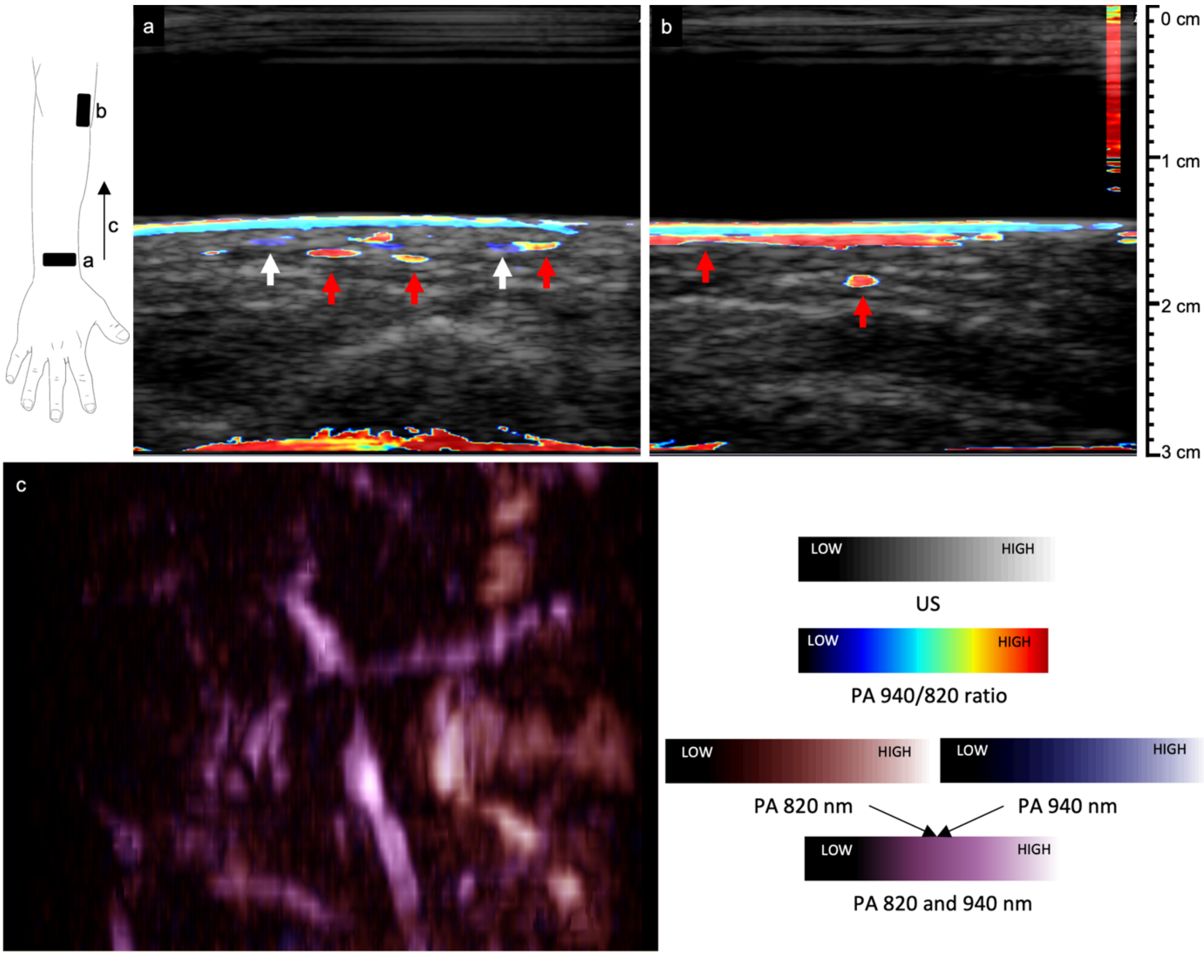

Figure 4.3: Ultrasound and 940/820 nm ratio photoacoustic (PA) images of a healthy arm (patient 2). White arrows indicate lymphatic vessels and red arrows indicate blood vessels. ***(a)*** *Axial PA image slice of the dorsal forearm. Multiple lymphatic vessels (dark blue) and veins (dark red) are visible.* ***(b)*** *Parallel PA image slice of the elbow fold. A vein (dark red) is clearly visible along the length of the image.* ***(c)*** *Maximum intensity projection with skin melanin surface suppression of the dorsal forearm of healthy lymphatic vessels and blood vessels. 820 nm signal is displayed in red and in blue for 940 nm. Signal origination from both wavelengths is displayed in purple (mix of red and blue).*

4.4 Discussion

This study assessed the feasibility of LED-based photoacoustic imaging for visualization of lymphatic and blood vessels for the purpose of LVB surgical planning. We described the first results of handheld LED-based PAI in patients with secondary arm lymphedema.

The Acoustic X facilitated real-time visualization and differentiation of lymphatic and blood vessels using the 940/820 nm ratio functionality. Axial imaging was the easiest way to detect vessels. In most cases, lymphatic and/or blood vessels were visible within a couple of seconds of axial imaging. Contrarily, parallel imaging of especially the lymphatic vessels was less straightforward. Small movements or angulation differences of the probe can cause the image plane to change significantly, leaving a small and sometimes tortuous lymphatic vessel outside the imaging frame. This could also be a reason we did not often see lymphatic vessels and veins in one parallel frame. Subsequently, no lymphatic vessel contractions were observed in the parallel imaging frames because it was hard to distinguish between PA signal changes due to motion or in the actual ICG signal. Axial images generally were too short (<25 seconds) to observe contractions. In the future, longer axial measurements, and parallel measurements with improved stability, might demonstrate vessel contractility, since the number of contractions lies between 0.3 – 1.3 contractions/min depending on the severity of lymphosclerosis.[20-22]

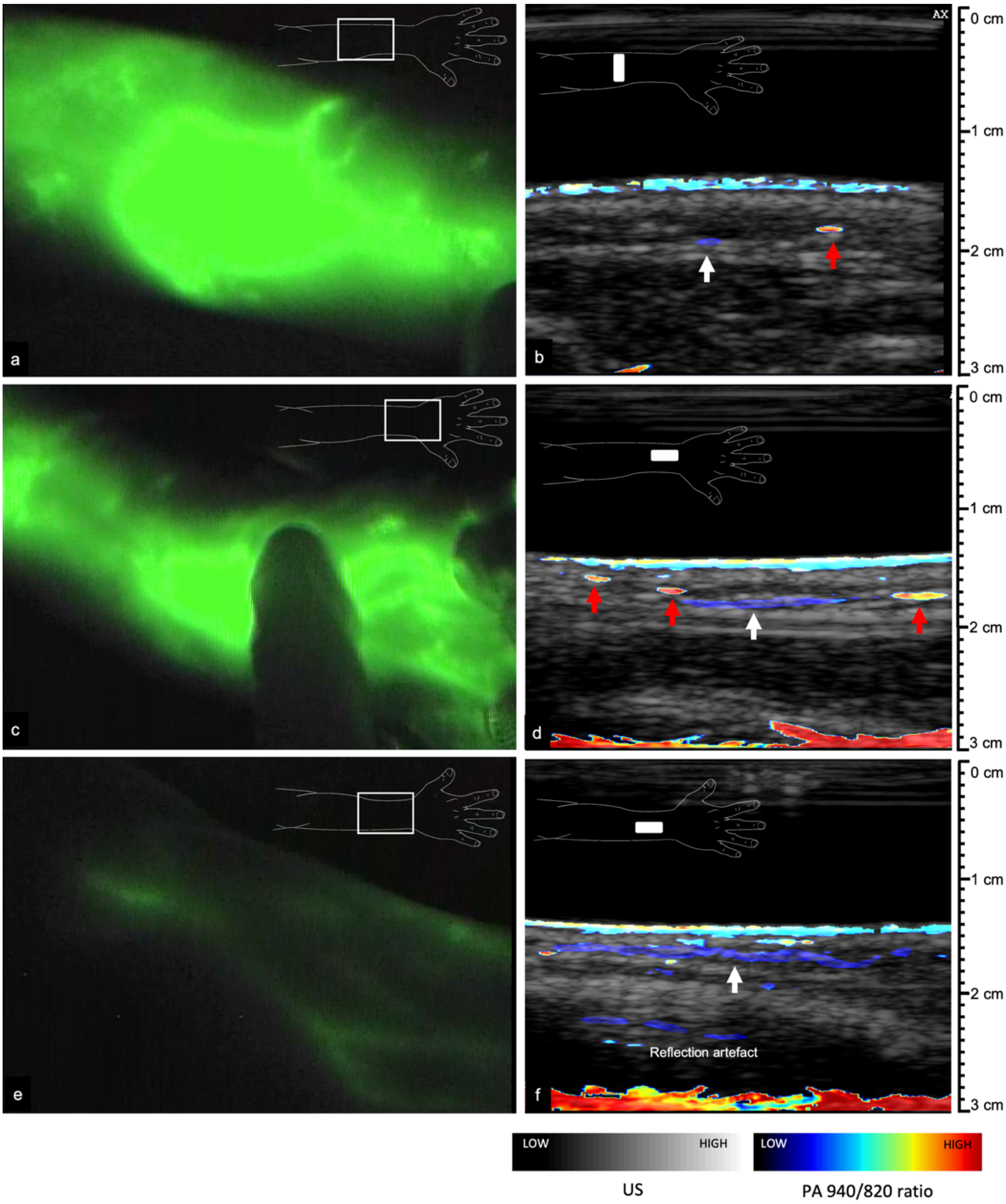

Figure 4.4: Near infrared fluorescence lymphography (NIRF-L) and 940/820 nm ratio photoacoustic (PA) and ultrasound images of patient 3. White arrows indicate lymphatic vessels and red arrows indicate blood vessels. ***(a)*** *NIRF-L image of the dorsal forearm shows two patient lymphatic vessels (linear pattern).* ***(b)*** *Axial PA image slice of the dorsal forearm. One lymphatic vessel (blue) and one blood vessel (red) are visible.* ***(c)*** *NIRF-L image of the dorsal wrist shows two patient lymphatic vessels (linear pattern).* ***(d)*** *Parallel PA image slice of the dorsal forearm. A lymphatic vessel (dark blue) is clearly visible along the length of the image.* ***(e)*** *NIRF-L image of the dorsal of the healthy arm (linear pattern) with a low signal intensity from the lymphatic vessels.* ***(f)*** *Parallel PA image slice of the dorsal forearm of the healthy arm. A lymphatic vessel is visible over the entire length of the image with a reflection artefact at 2.5 cm depth.*

An important clinically relevant finding is, that in all locations where extensive DBF obscured the vessels in NIRF-L images, lymphatic vessels could be imaged with PAI. This demonstrates a clear advantage of the depth resolution offered by PAI, that is not present in NIRF-L images. In the data we acquired so far, we were unable to identify a clear signal that can be attributed to DBF, likely because ICG concentration in the superficial layer is small (yet producing a strong NIRF signal due to minimal optical attenuation). Identification of such pathological patterns is an important diagnostic capability of NIRF-L and further research in PAI is warranted to investigate their appearance in the images in more detail.

Lymphatic and blood vessels were observed up to 5 and 4.9 mm from the skin surface, respectively. Diameter measurements were complicated by the dependence of the vessel appearance on the relative alignment between probe and vessel. Axial image resolution is 210 μm for 70 ns pulse widths, which should be sufficient for the subcutaneous lymphatic vessels.[23] Pressure of the probe on the skin surface may also lead to compression of the vessels, so even if accurate size measurements were possible, it is unclear if they represent the actual vessel size. Annotation was done manually and we did not examine the intra- or inter-rater variability of these measurements.

We also investigated if handheld 3D swipes provide a general overview of the course of lymphatic vessel over a larger surface area. During these swipes it is important that the pressure of the probe on the subject's arm is minimized. Too much pressure can lead to displacement of the ICG from the lymphatic vessels below the probe and leaving the lymphatic vessel 'empty' in the imaging frame. Furthermore, the consistency of the distance axis in the sweep direction (vertical in Figure 4.3c) depends on moving the probe at a constant speed. This was challenging, using manual motion, and changes in speed lead to interpolation artefacts in the MIP.

Lacking a standardized acquisition protocol, handheld PAI is still relatively operator dependent and less intuitive compared to NIRF-L. This could be a reason why the quality of the obtained images was relatively low for the first patient. Compared to (high-frequency) ultrasound, discussed in 2.3.6 the clear optical contrast afforded by PAI makes detection of the lymphatic vessels and veins much more straightforward and less dependent on operator interpretation.[24-27] Since this study expressly aimed at investigating clinical applicability, we designed the imaging protocol to be complete within 30 minutes. We demonstrated that it is possible to obtain extensive PAI images of both arms within this time frame, which is compatible with a diagnostic consultation setting.

A limitation of this study is that we were only able to include three patients. We aim to include more patients to confirm the preliminary findings presented here and extend our experience. PAI has a learning curve, which can already be observed in the image quality and ease of acquisition in the course of this short series of patients. In future imaging sessions, we expect that imaging will become easier and possibly result in better quality images. A potential effect of user experience is better parallel alignment images. We also expect that the addition of manual stimulation of lymphatic fluid flow will improve lymphatic vessel detectability. Furthermore, longer recordings with minimized probe movement can be expected due to the increased awareness of its importance.

PAI suffers from reflection artefacts as result of acoustic reflections of the generated photoacoustic wave.[28,29]

In all images reflection artefacts were observed at around 30 mm from the US probe. A photoacoustic signal is generated due to light absorption in the probe front surface (detected at $t \approx 0\ \mu s$; not shown in the images). These waveforms are also reflected at the skin surface (approximately 15 mm from the probe surface), leading to reflection artefacts at ~30 mm depth. However, these artefacts can easily be cropped from the image by altering the maximum depth that is displayed. This type of reflection artefact is easy to discern and shows up at depths where we know that the light will not reach, and we therefore do not expect any signal. In one case, a reflection artefact of a lymphatic vessel was also seen possibly due to reflection of the generated wave on the bone surface. Reflection artefacts on bone surfaces have previously been demonstrated in imaging of the interphalangeal joints.[30,31] This artefact is more difficult to identify and could easily be confused for an actual lymphatic vessel. This emphasizes that trained users that have knowledge on the principles of photoacoustic imaging, to avoid misinterpretation of artefacts for clinically meaningful signals. However, the combined US-PA imaging does improve the interpretability of the images and can help resolve where certain signals and artefacts originate from.

4.5 Conclusion

For the clinical translation of PAI to guide LVB surgical planning, it is important to have a compact and portable system for compatibility with the current workflow. In this study, we showed that this novel technique of handheld dual-wavelength PAI can be used in a clinical setting, and is not more invasive than NIRF-L which is currently routinely used. We demonstrated that dual-wavelength, LED-based PAI can visualize lymphatic and blood vessels. These findings suggest that PAI has potential for pre-operative lymphedema assessment, especially in cases with extensive DBF pattern hindering adequate assessment with NIRF-L. However, LED-based photoacoustics is still in its early stages of development and our findings need to be confirmed in larger groups of patients. Technological advances are needed to improve image quality and minimize image artefacts.

References

1 Taghian, N. R., Miller, C. L., Jammallo, L. S. et al. Lymphedema following breast cancer treatment and impact on quality of life: A review. *Crit. Rev. Oncol. Hematol.* 2014;(92):227-234, doi:10.1016/j.critrevonc.2014.06.004.

2 Basta, M. N., Gao, L. L. & Wu, L. C. Operative Treatment of Peripheral Lymphedema: A Systematic Meta-Analysis of the Efficacy and Safety of Lymphovenous Microsurgery and Tissue Transplantation. *Plast. Reconstr. Surg.* 2014;(133):905-913, doi:10.1097/PRS.0000000000000010.

3 Chang, D. W., Suami, H. & Skoracki, R. A Prospective Analysis of 100 Consecutive Lymphovenous Bypass Cases for Treatment of Extremity Lymphedema. *Plast. Reconstr. Surg.* 2013;(132):1305-1314, doi:10.1097/PRS.0b013e3182a4d626.

4 Mihara, M., Hara, H., Tange, S. et al. Multisite Lymphaticovenular Bypass Using Supermicrosurgery Technique for Lymphedema Management in Lower Lymphedema Cases. *Plast. Reconstr. Surg.* 2016;(138):262-272, doi:10.1097/PRS.0000000000002254.

5 Rosian, K. & Stanak, M. Efficacy and safety assessment of lymphovenous anastomosis in patients with primary and secondary lymphoedema: A systematic review of prospective evidence. *Microsurgery.* 2019;(39):763-772, doi:10.1002/micr.30514.

6 Desmettre, T., Devoisselle, J. M. & Mordon, S. Fluorescence Properties and Metabolic Features of Indocyanine Green (ICG) as Related to Angiography. *Surv. Ophthalmol.* 2000;(45):15-27, doi:10.1016/S0039-6257(00)00123-5.

7 Landsman, M. L., Kwant, G., Mook, G. A. et al. Light-absorbing properties, stability, and spectral stabilization of indocyanine green. *J. Appl. Physiol.* 1976;(40):575-583, doi:10.1152/jappl.1976.40.4.575.

8 Shikayama, T. in *ICG Fluorescence Imaging and Navigation Surgery* (eds Mitsuo Kusano, Norihiro Kokudo, Masakazu Toi, & Masaki Kaibori) 21-27 (Springer Japan, 2016).

9 Suami, H., Heydon-White, A., Mackie, H. et al. A new indocyanine green fluorescence lymphography protocol for identification of the lymphatic drainage pathway for patients with breast cancer-related lymphoedema. *BMC Cancer.* 2019;(19), doi:10.1186/s12885-019-6192-1.

10 Unno, N., Inuzuka, K., Suzuki, M. et al. Preliminary experience with a novel fluorescence lymphography using indocyanine green in patients with secondary lymphedema. *J. Vasc. Surg.* 2007;(45):1016-1021, doi:10.1016/j.jvs.2007.01.023.

11 Yamamoto, T., Matsuda, N., Doi, K. et al. The earliest finding of indocyanine green lymphography in asymptomatic limbs of lower extremity lymphedema patients secondary to cancer treatment: the modified dermal backflow stage and concept of subclinical lymphedema. *Plast. Reconstr. Surg.* 2011;(128):314e-321e.

12 Yamamoto, T., Narushima, M., Doi, K. et al. Characteristic indocyanine green lymphography findings in lower extremity lymphedema: the generation of a novel lymphedema severity staging system using dermal backflow patterns. *Plast. Reconstr. Surg.* 2011;(127):1979-1986.

13 Yamamoto, T., Yamamoto, N., Doi, K. et al. Indocyanine green-enhanced lymphography for upper extremity lymphedema: a novel severity staging system using dermal backflow patterns. *Plast. Reconstr. Surg.* 2011;(128):941-947.

14 Kajita, H., Suzuki, Y., Sakuma, H. et al. Visualization of Lymphatic Vessels Using Photoacoustic Imaging. *Keio. J. Med.* 2020:1-11, doi:10.2302/kjm.2020-0010-oa.

15 Lillis, A. P. & Krishnamurthy, R. Photoacoustic Imaging Addresses a Long-standing Challenge in Lymphedema. *Radiology.* 2020;(295):475-477, doi:10.1148/radiol.2020192824.

16 International Society of Lymphology. The diagnosis and treatment of peripheral lymphedema: 2016 consensus document of the International Society of Lymphology. *Lymphology.* 2016;(49):170-184.

17 The european parliament and the council of the european union. *REGULATION (EU) 2017/745 OF THE EUROPEAN PARLIAMENT AND OF THE COUNCIL of 5 April 2017 on medical devices, amending Directive 2001/83/EC, Regulation (EC) No 178/2002 and Regulation (EC) No 1223/2009 and repealing Council Directives 90/385/EEC and 93/42/EEC.* Official Journal of the European Union (2017).

18 Nguyen, A. T., Suami, H., Hanasono, M. M. et al. Long-term outcomes of the minimally invasive free vascularized omental lymphatic flap for the treatment of lymphedema. *J. Surg. Oncol.* 2017;(115):84-89, doi:10.1002/jso.24379.

19 Jaeger, M., Schüpbach, S., Gertsch, A. et al. Fourier reconstruction in optoacoustic imaging using truncated regularized inverse k -space interpolation. *Inverse Probl.* 2007;(23):S51-S63, doi:10.1088/0266-5611/23/6/s05.

20 Kelly, B., Mohanakumar, S., Telinius, N. et al. Function of Upper Extremity Human Lymphatics Assessed by Near-Infrared Fluorescence Imaging. *Lymphat. Res. Biol.* 2020;(18):226-231.
21 Granoff, M. D., Johnson, A. R., Lee, B. T. et al. A Novel Approach to Quantifying Lymphatic Contractility during Indocyanine Green Lymphangiography. *Plast. Reconstr. Surg.* 2019;(144):1197-1201, doi:10.1097/prs.0000000000006176.
22 Rasmussen, J. C., Tan, I., Marshall, M. V. et al. Human lymphatic architecture and dynamic transport imaged using near-infrared fluorescence. *Transl. Oncol.* 2010;(3):362-372, doi:10.1593/tlo.10190.
23 Agrawal, S., Kuniyil Ajith Singh, M., Johnstonbaugh, K. et al. Photoacoustic Imaging of Human Vasculature Using LED versus Laser Illumination: A Comparison Study on Tissue Phantoms and In Vivo Humans. *Sensors.* 2021;(21):424.
24 Czedik-Eysenberg, M., Steinbacher, J., Obermayer, B. et al. Exclusive use of ultrasound for locating optimal LVA sites—A descriptive data analysis. *J. Surg. Oncol.* 2020;(121):51-56, doi:10.1002/jso.25728.
25 Hayashi, A., Hayashi, N., Yoshimatsu, H. et al. Effective and efficient lymphaticovenular anastomosis using preoperative ultrasound detection technique of lymphatic vessels in lower extremity lymphedema. *J. Surg. Oncol.* 2018;(117):290-298, doi:10.1002/jso.24812.
26 Hayashi, A., Yamamoto, T., Yoshimatsu, H. et al. Ultrasound visualization of the lymphatic vessels in the lower leg. *Microsurgery.* 2016;(36):397-401.
27 Mihara, M., Hara, H. & Kawakami, Y. Ultrasonography for classifying lymphatic sclerosis types and deciding optimal sites for lymphatic-venous anastomosis in patients with lymphoedema. *J. Plast. Reconstr. Aesthet. Surg.* 2018;(71):1274-1281.
28 Jaeger, M., Bamber, J. C. & Frenz, M. Clutter elimination for deep clinical optoacoustic imaging using localised vibration tagging (LOVIT). *Photoacoustics.* 2013;(1):19-29, doi:10.1016/j.pacs.2013.07.002.
29 Kuniyil Ajith Singh, M., Jaeger, M., Frenz, M. et al. Photoacoustic reflection artifact reduction using photoacoustic-guided focused ultrasound: Comparison between plane-wave and element-by-element synthetic backpropagation approach. *Biomed. Opt. Express.* 2017;(8):2245-2260, doi:10.1364/BOE.8.002245.
30 Peter van, E., Samir, K. B., Hein, J. B. M. et al. Initial results of finger imaging using photoacoustic computed tomography. *J. Biomed. Opt.* 2014;(19):1-3, doi:10.1117/1.JBO.19.6.060501.
31 Nguyen, H. N. Y., Hussain, A. & Steenbergen, W. Reflection artifact identification in photoacoustic imaging using multi-wavelength excitation. *Biomedical Optics Express.* 2018;(9):4613-4630, doi:10.1364/BOE.9.004613.

5

Discussion and future perspectives

5.1 Overview

The goal of this thesis was to investigate the feasibility of light emitting diode (LED) based photoacoustic imaging (PAI) of lymphatic vessels and the venous network for the purpose pre-operative planning of lympho-venous bypass (LVB) surgery.
The systematic review about lymphatic vessel imaging summarized imaging modalities used for surgical decision making for treatment of lymphedema. Near-infrared fluorescence lymphography (NIRF-L) has become popular in the last decade for severity assessment and can accurately locate potential anastomosis sites. Photoacoustic imaging (PAI), specifically with LEDs as the light pulse generator, is a novel technique that has properties that overcome some of the major downsides of NIRF-L.
We first demonstrated LED-based dual-wavelength PAI for the differentiation between indocyanine green (ICG) and hemoglobin in blood using the 940/820 nm ratio. This functionality was also used for in-vivo measurements in lymphedema patients. Preliminary findings showed that PAI allowed for lymphatic vessel depiction using ICG contrast and blood vessel visualization for depths up to 5 mm, even in the presence of dermal backflow (DBF).

5.2 Feasibility of LED-based PAI for LVB surgical planning

In Chapter 1 of this thesis the following properties of an ideal lymphatic vessel imaging modality were defined. Ideally, an imaging modality:

- Can visualize lymphatic vessels in three dimensions
- Can visualize receiving veins in three dimensions
- Can perform real-time imaging
- Can visualize lymphatic vessel functionality (i.e., contractions)
- Is portable for easy implementation in multiple clinical settings (outpatient clinic & operating room)

Both NIRF-L and PAI meet the minimum requirement to facilitate lymphatic vessel imaging. On top of that, both modalities can image in real-time and are portable making implementation in both outpatient and operating room settings possible. NIRF-L is easy and intuitive to use partly because of the large field of view, while PAI requires experience and can only image a small region of interest. A big advantage of PAI is that it contains high-resolution information in all three dimensions and is therefore able to visualize lymphatic vessels, while NIRF-L does not have any depth information, has low resolution and lymphatic vessels are not visible under DBF patterns. Visualization behind DBF can have major advantages in patients that are considered inoperable (i.e., LVB not possible) due the inability to depict lymphatic vessels behind DBF with NIRF-L. Furthermore, PAI can confirm if there actually is a vein in close proximity to the lymphatic vessel.

5.3 Future perspectives

Even though the first patient measurements presented in chapter 4 of this thesis show the potential of LED-based PAI of the lymphatic vessels, several questions remain unanswered at present and technical challenges lie ahead.

5.3.1 Technical improvements

The PAI device used in this research is designed for preclinical and research related clinical imaging. Distinct advantages of using LEDs as PA excitation sources are the small footprint, relatively low cost, and safe use without the need for additional safety precautions (like laser goggles).

There are several ways the design of the device can be improved to make it more suitable for clinical implementation in lymphatic vessel imaging. The configuration of the ultrasound (US) probe, connector piece and LED arrays in combination with ultrasound gel led to difficulties cleaning the device. All parts had to be disconnected and cleaned separately before they could be assembled again, which is not desirable for clinical practice where easy and quick cleaning is important to not interfere with daily practice. Most importantly, the small spaces between the heat sink elements of the LED arrays were prone to leaving gel residues.

Additionally, the separate ultrasound coupling pad was used to fill the space between the ultrasound probe and the surface of the skin. Lateral movements caused the coupling pad to move out of the imaging plane resulting in artefacts due to the insufficient acoustic coupling. Future designs should consider either securing the coupling pad in place or integration of acoustic coupling in the probe design.

In terms of user friendliness, the graphical user interface was designed in such a way that the user could change a wide variety of parameters and settings. This is incredibly important for preclinical research and phantom studies but for clinical use, the interface must be simplified so that only the essential settings can be changed by the user. For this research, we did not image continuously for more than two minutes to prevent extensive heat buildup in the heat sinks, which can lead to lower LED power output and burn hazards. Future designs of the device should consider mitigating this hazard and extend the duration of imaging possible.

The 3D reconstruction algorithm assumes that the probe moves with a constant speed over a linear path during acquisition. Realistically, during handheld acquisition, the probe moving speeds will vary over the entire course and lateral movements are unavoidable. This leads to low quality maximum intensity projections and unreliable distance information. Techniques such as tracking,[1] tattoo tomography[2] or deep learning methods[3] could potentially improve 3D tomographic reconstructions.

For the clinical study we were limited by the availability of certain LED wavelength combinations that were compatible with the Acoustic X. The 940/820 nm ratio worked well for differentiation between lymphatic and blood vessels, but also reduced the frame rate significantly because additional moving averages were applied to obtain a sufficient signal to noise ratio. Furthermore, skin melanin signal and DBF signal did not seem to be separable using only these two wavelengths. Future research should focus on improving tissue differentiation specificity for skin-melanin and DBF signal from ICG by for example multispectral imaging with more than two wavelengths and spectral unmixing. This has already been demonstrated using phantom experiments using three LED wavelengths[4] and for differentiation between oxygenated hemoglobin, deoxygenated hemoglobin and ICG.[5]

The magnitude and depth of the in-vivo photoacoustic signal depends on two main factors: the light penetration in the tissue and the sensitivity of the ultrasound probe. In case of lymphatic vessel imaging, we are bound to external light delivery and light safety exposure limits for skin and eyes. The PA signal has a wide spectral content and is only partially detected by narrow bandwidth ultrasound probes such as the one used in this thesis.[6] In an ideal situation, the probe provides high resolution imaging and a high detection sensitivity for deep and faint photoacoustic signal over a wide frequency range. There have been many developments in ultrasound probe designs to improve resolution and detection sensitivity such as ultrasound transducers with a broad spectral bandwidth or dual-frequency probe designs.[7,8]

Lastly, a big field of research in PAI is improving image quality and artefact removal.[9-13] PAI is prone to clutter artefacts and most importantly reflection artefacts which can be mistaken for actual meaningful structures.[14] Possible solution such as photoacoustic-guided focused ultrasound (PAFUSion),[15,16] multi-wavelength excitation[17,18] or deep learning techniques[19,20] have been developed for reflection artefact removal and research on improving photoacoustic image quality is ongoing.[9-13]

5.3.2 Clinical research

In this thesis, only preliminary results in three patients were presented. The first step is to include more patients (inclusion of up to ten patients was approved by the medical research ethics committee). Additional measurements with the same research set up as described Chapter 4 will elaborate on our preliminary findings. For future patients, longer axial measurements should be done to potentially detect lymphatic vessel contractions, since this proved to be complicated with parallel probe alignment.

To further demonstrate the potential of PAI as a clinical tool in LVB surgical planning, the added benefits compared to NIRF-L must be demonstrated. It has been observed that suitable lymphatic vessels (normal, ectasis and contraction type) are present in stardust (up to 70%) and to a lesser extent diffuse (up to 50%) DBF patterns.[20] With NIRF-L, these patients would not be considered for LVB, while PAI can potentially detect these vessels. It must be noted that these results are based on static imaging several hours after ICG injections. Similar statistics based on dynamic NIRF-L are unknown. It is also known that LVB is more effective when anastomosis is performed with a functional lymphatic vessel.[21,22] Even in advanced lymphedema, LVB of functional lymphatic vessels can provide sufficient treatment effects (e.g., volume reduction).[23] Therefore, features such as lymphatic vessel detection in the presence of DBF and visualization of lymphatic vessel contractility play a big role in showing the potential of PAI.

In the short term, additional clinical studies should be done to investigate above mentioned features of PAI. These studies should not influence surgical decision making until there is enough evidence for PAI based anastomosis site selection. With this first feasibility study, NIRF-L imaging was used to determine the locations for PAI imaging. A future study on PAI without prior indication of imaging locations is a next step. This research could focus on how many lymphatic vessels were observed with PAI in comparison with NIRF-L in different regions of the limb. The population should encompass patients with different severities of lymphedema and DBF patterns. This way the added value of lymphatic vessel depiction in different types of patients can be tested. In addition, two observers can determine anastomosis sites based on NIRF-L and PAI independently. The number of potential anastomosis sites, location and reasoning of LVB site selection should be noted and compared. The reproducibility of the obtained images should also be investigated. Multiple attempts to visualize the same lymphatic vessel can demonstrate if the same quality image can be obtained in different instances.

Lastly, after adequate lymphatic vessel depiction, adequate anastomosis site selection, and the reproducibility of the technique have been proven, a study with pre-operative PAI with direct intraoperative confirmation of the obtained images would be interesting to further demonstrate its usability for pre-operative assessment. In the long-term, comparative studies between NIRF-L and PAI could also demonstrate if anastomosis sites that are detected with PAI lead to better post-operative outcomes than those detected with NIRF-L. However, for this type of research, PAI must also facilitate detection of pathological aspects of lymphedema such as DBF to prevent surgery in healthy lymphatic vessels and determine which lymphatic vessels contribute most to DBF. Furthermore, larger number of patients are needed for this type of research to obtain sufficient statistical evidence.

References

1 Sun, S. & Anthony, B. W. Freehand 3D ultrasound volume imaging using a miniature-mobile 6-DOF camera tracking system in *IEEE ISBI.* 1084-1087 (2012), doi:10.1109/ISBI.2012.6235747.

2 Holzwarth, N., Schellenberg, M., Gröhl, J. et al. Tattoo tomography: Freehand 3D photoacoustic image reconstruction with an optical pattern. *Int. J. Comput. Assist. Radiol. Surg.* 2021;(16):1101-1110, doi:10.1007/s11548-021-02399-w.

3 Prevost, R., Salehi, M., Jagoda, S. et al. 3D freehand ultrasound without external tracking using deep learning. *Med. Image Anal.* 2018;(48):187-202, doi:10.1016/j.media.2018.06.003.

4 Agrawal, S., Fadden, C., Dangi, A. et al. Light-Emitting-Diode-Based Multispectral Photoacoustic Computed Tomography System. *Sensors.* 2019;(19), doi:10.3390/s19224861.

5 Grasso, V., Holthof, J. & Jose, J. An Automatic Unmixing Approach to Detect Tissue Chromophores from Multispectral Photoacoustic Imaging. *Sensors.* 2020;(20), doi:10.3390/s20113235.

6 Allen, T. J. & Beard, P. C. Optimising the detection parameters for deep-tissue photoacoustic imaging in *Proc.SPIE.* (2012), doi:10.1117/12.908813.
7 Manwar, R., Kratkiewicz, K. & Avanaki, K. Overview of Ultrasound Detection Technologies for Photoacoustic Imaging. *Micromachines (Basel).* 2020;(11):692, doi:10.3390/mi11070692.
8 Miri Rostami, S. R., Mozaffarzadeh, M., Ghaffari-Miab, M. et al. GPU-accelerated Double-stage Delay-multiply-and-sum Algorithm for Fast Photoacoustic Tomography Using LED Excitation and Linear Arrays. *Ultrason. Imaging.* 2019;(41):301-316, doi:10.1177/0161734619862488.
9 Mozaffarzadeh, M., Hariri, A., Moore, C. et al. The double-stage delay-multiply-and-sum image reconstruction method improves imaging quality in a LED-based photoacoustic array scanner. *Photoacoustics.* 2018;(12):22-29, doi:10.1016/j.pacs.2018.09.001.
10 Farnia, P., Najafzadeh, E., Hariri, A. et al. Dictionary learning technique enhances signal in LED-based photoacoustic imaging. *Biomed. Opt. Express.* 2020;(11):2533-2547, doi:10.1364/BOE.387364.
11 Hariri, A., Alipour, K., Mantri, Y. et al. Deep learning improves contrast in low-fluence photoacoustic imaging. *Biomed. Opt. Express.* 2020;(11):3360-3373, doi:10.1364/BOE.395683.
12 Allen, T. J. & Beard, P. C. High power visible light emitting diodes as pulsed excitation sources for biomedical photoacoustics. *Biomed. Opt. Express.* 2016;(7):1260-1270, doi:10.1364/BOE.7.001260.
13 Jaeger, M., Bamber, J. C. & Frenz, M. Clutter elimination for deep clinical optoacoustic imaging using localised vibration tagging (LOVIT). *Photoacoustics.* 2013;(1):19-29, doi:10.1016/j.pacs.2013.07.002.
14 Kuniyil Ajith Singh, M. & Steenbergen, W. Photoacoustic-guided focused ultrasound (PAFUSion) for identifying reflection artifacts in photoacoustic imaging. *Photoacoustics.* 2015;(3):123-131, doi:10.1016/j.pacs.2015.09.001.
15 Kuniyil Ajith Singh, M., Jaeger, M., Frenz, M. et al. Photoacoustic reflection artifact reduction using photoacoustic-guided focused ultrasound: Comparison between plane-wave and element-by-element synthetic backpropagation approach. *Biomed. Opt. Express.* 2017;(8):2245-2260, doi:10.1364/BOE.8.002245.
16 Nguyen, H. N. Y., Hussain, A. & Steenbergen, W. Reflection artifact identification in photoacoustic imaging using multi-wavelength excitation. *Biomedical Optics Express.* 2018;(9):4613-4630, doi:10.1364/BOE.9.004613.
17 Nguyen, H. N. Y. & Steenbergen, W. Feasibility of identifying reflection artifacts in photoacoustic imaging using two-wavelength excitation. *Biomedical Optics Express.* 2020;(11):5745-5759, doi:10.1364/BOE.401375.
18 Agrawal, S., Johnstonbaugh, K., Suresh, T. et al. In vivo demonstration of reflection artifact reduction in LED-based photoacoustic imaging using deep learning. *SPIE BiOS.* 2021;(11642), doi:10.1117/12.2579082.
19 Allman, D., Reiter, A. & Bell, M. A. L. Photoacoustic Source Detection and Reflection Artifact Removal Enabled by Deep Learning. *IEEE Trans. Med. Imaging.* 2018;(37):1464-1477, doi:10.1109/TMI.2018.2829662.
20 Hara, H., Mihara, M., Seki, Y. et al. Comparison of indocyanine green lymphographic findings with the conditions of collecting lymphatic vessels of limbs in patients with lymphedema. *Plast. Reconstr. Surg.* 2013;(132):1612-1618.
21 Visconti, G., Salgarello, M. & Hayashi, A. The Recipient Venule in Supermicrosurgical Lymphaticovenular Anastomosis: Flow Dynamic Classification and Correlation with Surgical Outcomes. *J. Reconstr. Microsur.g.* 2018;(34):581-589, doi:10.1055/s-0038-1649518.
22 Mihara, M., Hara, H., Tange, S. et al. Multisite Lymphaticovenular Bypass Using Supermicrosurgery Technique for Lymphedema Management in Lower Lymphedema Cases. *Plast. Reconstr. Surg.* 2016;(138):262-272, doi:10.1097/PRS.0000000000002254.
23 Cha, H. G., Oh, T. M., Cho, M.-J. et al. Changing the Paradigm: Lymphovenous Anastomosis in Advanced Stage Lower Extremity Lymphedema. *Plast. Reconstr. Surg.* 2021;(147).

6
Appendices

Appendix I: Supplementary file Systematic Review

This appendix contains all the supplementary information tables of the systematic literature review on lymphatic vessel imaging from Chapter 2 of this thesis.

Supplementary table 1: Search query

Embase	Records
('lymph vessel'/exp OR 'lymph flow'/de OR lymphography/de OR 'lymphatic system'/de OR lymphangiography/exp OR lymphoscintigraphy/exp OR ((lymph* NEAR/3 (vessel* OR venule* OR flow* OR function* OR pump* OR vascul* OR channel* OR contractil* OR transport* OR system*)) OR lymphogra* OR lymphangiogra* OR lymphoscintigra*):Ab,ti) AND (imaging/mj/de OR 'diagnostic imaging'/mj/exp OR 'diagnostic imaging equipment'/mj/exp OR 'nuclear magnetic resonance'/mj/exp OR radiodiagnosis/mj/exp OR spectroscopy/mj/exp OR scintigraphy/mj/exp OR dye/mj/exp OR fluorescence/mj/exp OR radioisotope/mj/exp OR echography/mj/exp OR photoacoustics/mj/exp OR technetium/mj OR 'contrast medium'/mj OR (imaging OR radiodiagnos OR Scintigra* OR lymphoscintigra* OR dye OR icg OR indocyanine-green OR fluorescen* OR radioisotope* OR technetium* OR spect OR tomograph* OR ct OR mri OR (magnet* NEAR/3 resonan*) OR Visualization* OR Visualisation* OR Lymphangiogra* OR Lymphogra* OR Mapping OR Quantitat* OR Quantif* OR detect* OR locating* OR echogra* OR ultraso* OR photoacoustic* OR optoacoustic* OR photo-acoustic* OR opto-acoustic* OR 99-tc OR 99tc OR spectroscop* OR near-infrared* OR near-infra-red* OR contrast-medi*):ti) AND (lymphedema/exp OR 'lymphaticovenular anastomosis'/de OR 'lymphovenous anastomosis'/de OR 'lymph node dissection'/de OR (lymphedem* OR lymph-oedem* OR lymph-edem* OR lymphoedem* OR ((Lymphaticovenul* OR Lymphoven* OR Lympho-ven*) NEAR/3 (shunt* OR bypass* OR anastomo*)) OR (lymph-node NEAR/3 dissect*) OR lymphadenectom*):ab,ti) AND (limb/exp OR 'limb disease'/exp OR head/exp OR neck/exp OR 'head and neck tumor'/exp OR (limb OR extremit* OR arm OR arms OR leg OR legs OR foot OR feet OR hand OR hands OR head OR neck):ab,ti) NOT ([animals]/lim NOT [humans]/lim) NOT [conference abstract]/lim NOT [letter]/lim NOT [note]/lim NOT (review/exp OR 'meta analysis'/de OR (review OR meta-analys*):ti)	954
Medline All via Ovid	
(Lymphatic Vessels/ OR Lymphography/ OR Lymphatic System/ OR Lymphoscintigraphy/ OR ((lymph* ADJ3 (vessel* OR venule* OR flow* OR function* OR pump* OR vascul* OR channel* OR contractil* OR transport* OR system*)) OR lymphogra* OR lymphangiogra* OR lymphoscintigra*).ab,ti.) AND (exp * Diagnostic Imaging/ OR exp * Magnetic Resonance Imaging/ OR exp * Radiography/ OR exp * Spectrum Analysis/ OR * Coloring Agents/ OR exp * Fluorescence/ OR * Radionuclide Imaging/ OR Radioisotopes/ OR exp * Ultrasonography/ OR * Technetium/ OR * Contrast Media/ OR (imaging OR radiodiagnos OR Scintigra* OR lymphoscintigra* OR dye OR icg OR indocyanine-green OR fluorescen* OR radioisotope* OR technetium* OR spect OR tomograph* OR ct OR mri OR (magnet* ADJ3 resonan*) OR Visualization* OR Visualisation* OR Lymphangiogra* OR Lymphogra* OR Mapping OR Quantitat* OR Quantif* OR detect* OR locating* OR echogra* OR ultraso* OR photoacoustic* OR optoacoustic* OR photo-acoustic* OR opto-acoustic* OR 99-tc OR 99tc OR spectroscop* OR near-infrared* OR near-infra-red*).ti.) AND (exp Lymphedema/ OR Lymph Node Excision/ OR (lymphedem* OR lymph-oedem* OR lymph-edem* OR lymphoedem* OR ((Lymphaticovenul* OR Lymphoven* OR Lympho-ven*) ADJ3 (shunt* OR bypass* OR anastomo*)) OR (lymph-node ADJ3 dissect*) OR lymphadenectom*).ab,ti.) AND (exp Extremities/ OR exp Head/ OR exp Neck/ OR exp Head and Neck Neoplasms/ OR (limb OR extremit* OR arm OR arms OR leg OR legs OR foot OR feet OR hand OR hands OR head OR neck).ab,ti.) NOT (exp animals/ NOT humans/) NOT (Review/ OR Systematic Review/ OR Meta-Analysis/ OR (review OR meta-analys*).ti.)	700
Web of Science Core Collection	
TS=((((lymph* NEAR/2 (vessel* OR venule* OR flow* OR function* OR pump* OR vascul* OR channel* OR contractil* OR transport* OR system*)) OR lymphogra* OR lymphangiogra* OR lymphoscintigra*)) AND ((lymphedem* OR lymph-oedem* OR lymph-edem* OR lymphoedem* OR ((Lymphaticovenul* OR Lymphoven* OR Lympho-ven*) NEAR/2 (shunt* OR bypass* OR anastomo*)) OR (lymph-node NEAR/2 dissect*) OR lymphadenectom*)) AND ((limb OR extremit* OR arm OR arms OR leg OR legs OR foot OR feet OR hand OR hands OR head OR neck))) AND TI=((imaging OR radiodiagnos OR Scintigra* OR lymphoscintigra* OR dye OR icg OR indocyanine-green OR fluorescen* OR radioisotope* OR technetium* OR spect OR tomograph* OR ct OR mri OR (magnet* NEAR/2 resonan*) OR Visualization* OR Visualisation* OR Lymphangiogra* OR Lymphogra* OR Mapping OR Quantitat* OR Quantif* OR detect* OR locating* OR echogra* OR ultraso* OR photoacoustic* OR optoacoustic* OR photo-acoustic* OR opto-acoustic* OR 99-tc OR 99tc OR spectroscop* OR near-infrared* OR near-infra-red* OR contrast-medi*) NOT ((animal* OR rat OR rats OR murine OR mouse OR mice) NOT (human* OR patient*))) AND DT=(article) NOT TI=(review OR meta-analys*)	563
Cochrane CENTRAL Register of Trials	
(((lymph* NEAR/3 (vessel* OR venule* OR flow* OR function* OR pump* OR vascul* OR channel* OR contractil* OR transport* OR system*)) OR lymphogra* OR lymphangiogra* OR lymphoscintigra*):Ab,ti) AND ((imaging OR radiodiagnos OR Scintigra* OR lymphoscintigra* OR dye OR icg OR indocyanine NEXT green OR fluorescen* OR radioisotope* OR technetium* OR spect OR tomograph* OR ct OR mri OR (magnet* NEAR/3 resonan*) OR Visualization* OR Visualisation* OR Lymphangiogra* OR Lymphogra* OR Mapping OR Quantitat* OR Quantif* OR detect* OR locating* OR echogra* OR ultraso* OR photoacoustic* OR optoacoustic* OR photo NEXT acoustic* OR opto NEXT acoustic* OR 99 NEXT tc OR 99tc OR spectroscop* OR "near infrared*" OR "near infra red*" OR contrast NEXT medi*):ti) AND ((lymphedem* OR lymph NEXT oedem* OR lymph NEXT edem* OR lymphoedem* OR ((Lymphaticovenul* OR Lymphoven* OR Lympho NEXT ven*) NEAR/3 (shunt* OR bypass* OR anastomo*)) OR (lymph NEXT node NEAR/3 dissect*) OR lymphadenectom*):ab,ti) AND ((limb OR extremit* OR arm OR arms OR leg OR legs OR foot OR feet OR hand OR hands OR head OR neck):ab,ti)	37

Supplementary table 2: Characteristics of included studies on lymphoscintigraphy

Study information		Patient characteristics				LE type (No.)			Limbs (No.)	
Year	Author	M (No.)	F (No.)	Age* (years)	ISL stage (%)	P	S	H	UL	LL
Diagnosis, severity staging and treatment indication										
2021	Bourgeois[1]	5	7	43.3 (21 - 70)	-	7	5	-	HN: 12	
2020	Pappalardo[2]	-	141	60.2 ± 12.4 (26 - 82)	-	-	141	-	-	141
2019	Campisi[3]	65	183	51.2 (9 -84)	-	151	97	-	48	200
2018	Tartaglione[4]	96		52 ± 9	-	-	96	-	58	80
2018	Cheng[5]	19	266	56.2 ± 14.3 (2 - 89)	-	30	155	-	126	159
2017	Maclellan[6]	134		27 (1 – 88)	I: 54 II: 30 III 16	106	28	-	24	157
2017	Hassanein[7]	64	163	36.7 ± 23	-	116	45	58	227	
2015	Yoo[8]	-	72	53.0 ± 8.1	-	-	72	-	72	-
2014	Devoogdt[9]	-	10	50 (30 – 67)	-	-	10	-	20	-
2012	Kalawat[10]	10	14	47 (13 - 74)	I: 15 II: 5 III: 30 IV: 50	Unclear etiology			-	48
2012	Infante[11]	16	44	43 (1 – 84)	-	32		28	4	56
2011	Mikami[12]	1	77	55.5 ± 13.2 (22 - 84)	I: 43.6 II: 53.8 III: 2.6	-	78	-	78	-
2010	Maegawa[13]	9	102	63 (38 - 92)	I: 15.8 II: 69.8 III: 14.4	-	111	-	-	142
2008	Pecking[14]	4328		(23 – 78)	0: 2.6 I: 12 II: 58 III: 27.4	NR		-	-	4328
2008	Dabrowski[15]	67		58 (11 – 87)	-	67		37	-	104
2000	Williams[16]	700		-	-	NR		-	700	
Predictive value										
2019	Kim[17]	-	80	51.2 ± 10.3 (30 - 75)	I: 36.3 II: 50.0 III: 13.7	-	80	-	80	-
2017	Chiewvit[18]	3	77	59.5 (12 - 72)	-	NR		-	80	
Tracer injection methodology										
2010	Tartaglione[19]	12	32	-	-	21	23	-	15	29
2006	O'Mahony[20]	-	6	(41 – 67)	-	-	6	-	6	-
2004	O'Mahony[21]	10	2	(24 – 40)	-	-	-	24	24	-
2003	Stanton[22]	-	13	54.7 ± 6.4	-	-	13	-	13	-
SPECT-CT										
2015	Baulieu[23]	39	61	52 (1 – 86)	-	100		-	3	94
2013	Baulieu[24]	7	34	67 (9 – 84)	-	17	5	-	-	41
2007	Pecking[25]	115		(23 – 77)	0: 25.2 I: 74.8	NR		-	-	115

**Values are mean (range) or ± standard deviation; M: male; F: female; ISL: International Society of Lymphology; P: primary; S: secondary; H: healthy; UL: upper limbs; LL: lower limbs; LE: lymphedema; NR: not reported; HN: head and neck*

Supplementary table 3: Contrast agents and imaging methods used for lymphoscintigraphy

	Tracer administration						**Acquisition moments (minutes post-injection)**	
Authors	Contrast agent (^{99m}Tc-labeled)	A (MBq)	Dose (mL)	Type	Injection site	Rest/stress/massage	Static	Dynamic
Bourgeois[1]	HSA nanocolloid	81	0.2	sc	Forehead	Massage	-	-
Pappalardo[2]	phytate	37	0.5	sc	1^{st} ids feet	Rest	5 and 120	-
Campisi[3]	HSA nanocolloid	30-50	-	sc & sf	sc: 2^{nd} ids hands and feet sf: palmar surface hands and feet	Stress	30 and 60	-
Tartaglione[4]	nanocolloid	50-80	0.3	id	UL: 1^{st} + 4^{th} ims LL: 1^{st} ims + peroneal malleolus area	Massage & stress	0 (pre-stress), multiple (post-stress), 60	-
Cheng[5]	pytate	37	0.5	sc	2^{nd} ids hands or 1^{st} ids feet	Stress	5, 120	-
Maclellan[6]	filtered sulfur colloid	-	-	id	NR	NR	45, 120, 240	-
Hassanein[7]	filtered sulfur colloid	37	-	id	2^{nd} and 4^{th} ids hands and feet	NR	45, 120, 240	-
Yoo[8]	pytate	185	-	sc	2^{nd} ids hands	Stress	30, 60 and 120	
Devoogdt[9]	HSA nanocolloid	85	0.2	sc	1^{st} and 2^{nd} ids hands	Rest & stress	1, 45 and 116 (injection sites), 120 (axilla), 124 (whole body)	3.5 (duration of 40 min 10s/frame)
Kalawat[10]	sulfur colloid	20	0.2	sc	1^{st} and 2^{nd} ids feet	Rest (stress in some cases)	0, 60, 240 and 1140	-
Infante[11]	nanocolloid	37	0.1	id	1^{st} and 2^{nd} ids hands or feet	Massage	30 and 120	-
Mikami[12]	HSA nanocolloid	40	0.2	sc	2^{nd} and 4^{th} ids hands	Rest	30 and 120	-
Maegawa[13]	HSA nanocolloid	40	0.2	sc	1^{st} and 3^{rd} ids feet	Rest	30 and 120	-
Pecking[14]	HSA nanocolloid	-	0.2	sc	1^{st} ids feet	Stress	60	0 (injection sites 30 s/frame)
Dabrowski[15]	HSA nanocolloid	37	-	sc	1^{st}, 2^{nd}, 3^{rd} and 4^{th} ids feet	Stress	120	0 (injection site) 20 (lymph nodes)
Williams[16]	HSA nanocolloid	18.5	-	id	2^{nd} ids foot or hand	Rest, Massage & stress	30, 35 and 180/240	0 (duration = 15 min)
Kim[17]	phytate	148	-	sc	2^{nd} and 3^{rd} ids hands	Stress	60 and 120	-
Chiewvit[18]	dextran	37	-	sc	1^{st} and 2^{nd} ids hands or feet	Massage and stress	15, 30 ,45, 60 and 240	-
Tartaglione[19]	HSA nanocolloid	50	0.3-0.4	id	1^{st} ids hands and feet	Massage & stress	0 (pre-exercise) and until tracer reached lymph nodes (post-exercise)	-
O'Mahony[20]	HIG	40	0.1	sc/id	2^{nd} ids hands	-	10-16, 37-68, 82-95, 108-133, 148-171	-
O'Mahony[21]	nanocolloid OR HIG	40	0.1	sc/id	2^{nd} ids hands	-	Sequential images over 120/180	-
Stanton[22]	polyclonal HIG	35	0.2	im	Forearm	Massage	Every 30-60 min for 5 hours	0 (duration = 30 min)
Baulieu[23]	HSA nanocolloid	111	-	sc	1^{st} ids foot or hand	Rest and stress	40, 240	0 (duration = 40 min)
Baulieu[24]	HSA nanocolloid	111	0.2	sc	1^{st} ids foot	Rest and stress	40, 240	0 (duration = 40 min)
Pecking[25]	nanocolloid	-	0.2	sc	1^{st} ids feet	Stress	40	-

HAS: human serum albumin; HIG: human immunoglobulin; UL: upper limb; LL: lower limb; id: intradermal; sc: subcutaneous; sf = subfascial; im: intramuscular; ids: interdigital space; ims: intermetacarpal space; A: activity

Supplementary table 4: Characteristics of included studies on near-infrared fluorescence lymphography

Study information		**Patient characteristics**				**LE type (No.)**			**Limbs (No.)**	
Year	Author	M (No.)	F	Age* (years)	ISL/*Campisi* stage (%)	P	S	H	UL	LL
Diagnosis, severity staging and surgical planning										
2021	Jørgensen[26]	-	237	59.68 ± 9.94	-	-	237	-	237	-
2020	Thomis[27]	-	45	61.3 ± 9.9 (37 – 82)	I: 20 IIa: 40 IIb: 40	-	45	-	45	-
2020	Medina[28]	-	19	59 (53 - 68)	IIa: 42.1 IIb: 57.9	-	19	-	19	-
2020	Kinugawa[29]	1	13	70.2 (46 – 86)	-	-	14	-	-	14
2020	Lee[30]	12	3	28.3 ± 4.5 (24 – 41)	-	-	-	15	-	15
2019	Suami[31]	-	100	57.73 ± 9.78	-	-	100	-	103	-
2019	Matsumoto[32]	4	59	56.0 (20 – 78)	0: 23 I: 27 IIa: 28 IIb: 11	6	55	-	-	112
2019	Garza[33]	22	190	53.12 ± 11.7	-	32	180	-	130	82
2017	Shinaoka[34]	-	54 7	54.8 ± 9.7 58.4 ± 14.1	0: 39 I: 37.3 II: 23.1 III: 4.6	-	54 -	- 7	-	108 14
2017	Gentileschi[35]	1	15	58.8 ± 13.1 (27 – 77)	IIa: 43.8 IIb: 56.2	-	16	-	16	-
2016	Tashiro[36]	2	88	59	0: 15.5 I: 16.1 II: 51.7 III: 16.7	-	90	-	-	180
2016	Akita[37]	-	190	56.7 ± 12.4	-	-	190	-	190	-
2014b	Mihara[38]	-	5	53.8 (32 – 72)	IIa: 60 IIb: 40	-	5	-	-	5
2014a	Mihara[39]	-	72	54.5 (25 – 88)	*0: 6.9 I: 15.3* *II: 26.4. III: 33.3* *IV: 18.1*	-	72	-	-	144
2013	Akita[40]	-	100	54.8 (32 – 76)	-	-	100	-	-	100
2012	Suami[41]	-	3 34	- 54.5 ± 8.5	-	-	- 34	3 -	3 34	-
2012	Aldrich[42]	1 1	17 5	(45 – 68) (26 – 68)	-	-	18 -	- 6	18 6	-
2011a	Yamamoto[43]	1	27	47.2 (19 - 71)	-	-	28	-	-	56
2011c	Yamamoto[44]	-	20	57.5 (35 – 80)	*I: 20 II: 30* *III: 30 IV: 20*	-	20	-	20	-
2011b	Yamamoto[45]	-	45	48 (17 – 73)	*I: 12.8 II: 34.6* *III: 34.6 IV: 15.4* *V: 2.6*	3	42	-	-	90
2007	Unno[46]	1 7	11 3	64.3 ± 13.6 44.9 ± 17.3	-	-	12 -	- 10	-	12 10
2020	Johnson[47]	-	23	51.6	-	-	23	-	23	-
2017	Tashiro[48]	-	29	60.5 (36 - 84)	I: 13 II: 80 III: 7	-	29	-	30	-
Quantitative										
2020	Kelly[49]	10	-	25.7 ± 1.3	-	-	-	10	20	-
2019	Granoff[50]	-	17	60.5 ± 14.2	-	-	17	-	17	-
2017	Groenlund[51]	10	-	(20 – 30)	-	-	-	10	-	20
2014	Yamamoto[52]	-	15	57.5 (41 - 74)	0: 13.3 I: 20 II: 53.3 III: 13.3	-	30	-	30	-
2013	Yamamoto[53]	- -	12 3	23.89 (20.4 - 30.4)	0: 29.2 I: 29.2 II: 33.3 III: 8.3	- -	12 -	- 3	-	24 6
2010	Rasmussen[54]	1 5	19 19	49.7 ± 16.7 38.2 ± 11.0	-	3 -	17 -	- 24	10 12	10 12
2008	Unno[55]	10 17	- -	33.1 ± 7.9 74.7 ± 7.5	-	- Other		10 -	-	10 17
Injection methodology										
2020	Hara[56]	7	96	57.8 (11 - 82)	I: 28.2 IIa: 10.2 IIb: 41.7 III: 5.3	10	93	-	-	206
2019	Hara[57]	4	105	60.8 (30 - 88)	I: 32.1 IIa: 24.8 IIb: 35.8 III: 7.3	7	102	-	10	186
2013	Hara[58]	2	23	54 (25 – 75)	0: 25.6 I: 7.0 II: 65.1 III: 2.3	4	21	-	2	41
Comparison with scintigraphy										
2021	Yoon[59]	14	30	52.92 ± 15.13	-	-	44	-	-	44
2020	Yoon[60]	-	47	55.85 ± 10.51	-	-	47	-	47	-
2013	Mihara[61]	-	29	58.6 (32 – 79)	0: 22. I: 36.2 IIa: 15.5 IIb: 22.4 III: 3.4	-	29	-	-	58
2013	Akita[62]	19	115	58.5 (9 – 82)	-	39	95	-	-	234

**Values are mean (range) or ± standard deviation; M: male; F: female; ISL: International Society of Lymphology; P: primary; S: secondary; H: healthy; UL: upper limbs; LL: lower limbs; LE: lymphedema*

Supplementary table 5: Contrast agent administration methods for near-infrared fluorescence lymphography

Authors	**System**	**Dose (mL)**	**Type**	**Contrast medium (ICG)**	**Injection site**	
					Interdigital space	Other
Jørgensen[26]	Hyperye	0.1	sc & id	Verdye 0.25%, Diagnostic Green GmbH	1st, 3rd (hand)	ulnar border palmaris longus tendon at wrist level
Thomis[27]	PDE	0.2	id	NR	1st, 4th (hand)	-
Medina[28]	PDE	0.3	-	Verdye 0.5%, Diagnostic Green GmbH	2nd, 4th (hand)	-
Kinugawa[29]	PDE	0.2	-	NR	1st, 4th(feet)	lateral and medial ankles
Lee[30]	Moment K	1	sc	Dongindang Pharm.	2nd (hands)	-
Suami[31]	PDE	0.5 – 1	id	Verdye 0.5%, Diagnostic Green GmbH	1st, 4th ids hand &	ulnar and volar wrist region
Garza[33]	PDE	0.02	id	Akron Inc.	1st, 2nd, 3rd, 4th (hand/foot)	radial & ulnar wrist/inferior to the medial and lateral malleoli
Shinaoka[34]	PDE	0.06 0.04	sc id	Diagnogreen 0.625%, Daiichi Pharm. Diagnogreen 0.625%, Daiichi Pharm.	1st, 4th (foot)	lateral side foot and backside ankle
Gentileschi[35]	PDE	0.1	id	Verde Indocianina Pulsion	2nd (hand)	ulnar border of the palmaris longus
Tashiro[36]	PDE	0.1	sc	Diagnogreen 0.5%, Daiichi Pharm.	1st (feet)	lateral border Achilles tendon
Akita[37]	PDE	0.3	sc	NR	1st (hand)	-
Mihara[38]	PDE	0.2	sc	Diagnogreen 0.25%, Daiichi Pharm.	1st (feet)	lateral border Achilles tendon
Mihara[39]	PDE	0.2	id	Diagnogreen 0.5%, Daiichi Pharm.	1st (feet)	-
Akita[40]	PDE	0.3	sc	NR	1st (feet)	-
Suami[41]	PDE	0.02	id	NR	1st, 2nd, 3rd, 4th (hand)	-
Aldrich[42]	Custom	0.1	id	0.025%	-	Medial, lateral, ventral sides wrist & upper lateral forearm
Yamamoto[43]	PDE	0.2	sc	Diagnogreen 0.25%, Daiichi Pharm.	1st (feet)	lateral border Achilles tendon
Yamamoto[44]	PDE	0.1	sc	Diagnogreen 0.25%, Daiichi Pharm.	2nd (hands)	wrist at ulna
Yamamoto[45]	PDE	0.2	sc	Diagnogreen 0.25%, Daiichi Pharm.	1st (feet)	lateral border Achilles tendon
Unno[46]	PDE	0.2	sc	Diagnogreen 0.5%, Daiichi Pharm.	Dorsum of the foot	-
Johnson[47]	PDE	0.1	id	0.0625 %, Akorn Inc.	1st, 4th	volar forearm & cephalic vein (US guided)
Tashiro[48]	PDE	0.2	id	Diagnogreen 0.5%, Daiichi Pharm.	2nd (hand)	ulnar border palmaris longus tendon (wrist level)
Kelly[49]	Custom	0.1	id	Nomeco 0.30 %	2nd, 4th (hand)	palmar side wrist
Granoff[50]	PDE	0.1	id	ICG with albumin 0.0625%	1st, 4th (hand)	volar forearm & lateral upper ipsilateral arm
Groenlund[51]	Custom	0.1	id	Nomeco 0.0305 %	1st, 4th ims (feet)	behind medial malleolus
Yamamoto[52]	PDE	0.1	sc	Diagnogreen 0.25%, Daiichi Pharm.	2nd (hands)	-
Yamamoto[53]	PDE	0.2	sc	Diagnogreen 0.25%, Daiichi Pharm.	1st (feet)	-
Rasmussen[54]	Custom	0.1	id	0.025%	2 locations (hand/feet)	UL: 2 forearm and 2 upper arms LL: 2 medial ankles, 1 heel, 2 calf and 1 thigh
Unno[55]	PDE	0.3	sc	Diagnogreen 0.5%, Daiichi Pharm.	2nd, 4th (hands)	palmar side wrist
Hara[56]	PDE	0.5		Diagnogreen 0.5% Daiichi Pharm.	1st (feet)	proximal side of lateral condyle and lateral side of the superior edge of the knee
Hara[57]	PDE	0.1	sc	Diagnogreen 0.5%, Daiichi Pharm.	**Control**: 1st (feet), 2nd(hands)	**Multi-injection**: no linear pattern with 1 injection → also medial or lateral ankle or knee
Hara[58]	PDE	0.2	id	Diagnogreen 0.5%, Daiichi Pharm.	1st (feet) or 2nd (hands)	-
Yoon[59]	Moment K	0.2	sc	Diagnogreen 0.25%, Daiichi Pharm.	1st (feet)	lateral border Achilles tendon
Yoon[60]	Moment K	0.2	sc	Diagnogreen 0.25%, Daiichi Pharm.	1st, 3rd (hands)	-
Mihara[61]	PDE	0.2	id	Diagnogreen 0.5%, Daiichi Pharm.	1st (feet)	-
Akita[62]	PDE	0.3	sc	NR	1st (feet)	-

PDE: photodynamic eye (Hamamatsu Photonics K.K., Hamamatsu, Japan); sc: subcutaneous; id: intradermal; ims: intermetacarpal space; NR: not reported

Supplementary table 6: Quantitative near-infrared fluorescence lymphography parameters

		Kelly[49]	*Granoff*[50]	*Groenlund*[51]	*Yamamoto*[52]	*Yamamoto*[53]	*Rasmussen*[54]
Contractions (min^{-1})							
Arm	*control*	0.9 ± 0.4					1.3 ± 1.2
	unaffected						1.2 ± 1.0
	affected		1.13 (0.67 – 2.5)				0.3 ± 0.3
Leg	*control*			0.60 ± 0.23			0.4 ± 0.3
	unaffected						0.3 ± 0.2
	affected						0.2 ± 0.2
Velocity (cm/s)							
Arm	*control*	1.1 ± 0.3			0.5 ± 0.3		0.8 ± 0.4
	unaffected						0.8 ± 0.4
	affected				(0.01 - 0.2)		0.7 ± 1.0
Leg	*control*			1.51 ± 0.42		0.2 ± 0.06	0.9 ± 0.7
	unaffected						0.8 ± 0.5
	affected					(0.02 - 0.12)	0.8 ± 0.4

Supplementary table 7: Characteristics of included studies on magnetic resonance lymphangiography

Study information		Patient characteristics				LE type (No.)			Limbs (No.)	
Year	Author	M (No.)	F (No.)	Age* (years)	ISL stage (%)	P	S	H	UL	LL
Visualization, diagnosis and severity										
2021	Soga[63]	11	45	50.9 ± 16.9	0: 38.4 I: 18.8 II: 37.5 III: 5.4	23	33	-	-	112
2020	Sheng[64]	-	50	52.5 (42 - 63)	I: 14 II: 56 III: 30	-	50	-	100	-
2020	Abdelfattah[65]	-	59	-	-	-	59	-	59	-
2018	Ripley[66]	5 6	37 36	50.8 ± 14.2 55.4 ± 13.6	-	-	42 42	-	27 27	15 15
2017	Gennaro[67]	-	20	57.6	-	3	17	-	15	5
2016	Jeon[68]	9	18	39.6 ± 20.5	-	5	22	-	9	24
2016	Liu[69]	335	375	35 (5 - 78)	II: 89.6 III:10.4	378	332	-	NR	NR
2015	Borri[70]	-	3	(49 – 61)	-	-	3	-	6	-
2014	Zhou[71]	24	37	34 ± 17 (5 – 80)	I: 21.9 II: 57.8 III: 20.3	NR			-	48
2013	Liu[72]	20	25	49.2 (11 - 78)	I: 20.9 II: 45.8 III: 33.3	-	45	-	9	36
2012	Lu[73]	-	40	52.3 ± 11.9 (27 - 74)	-	-	40	-	-	48
2009	Notohamiprodjo[74]	4	12	44 ± 29	-	NR			-	16
2008	Dimakakos[75]	8	6	38.7 (10 – 66)	I: 66.7 II: 33.3	NR		2	-	14
2007b	Lohrmann[76]	3	7	44 (21 - 64)	-	8	2	-	-	20
2007a	Lohrmann[77]	1	2	53 (22 - 76)	-	2	1	-	-	3
2006c	Lohrmann[78]	4	8	47 (25 - 71)	-	11	1	-	-	24
2006b	Lohrmann[79]	2	8	42 (20 - 79)	-	8	2	-	-	10
2006a	Lohrmann[80]	2	1	60 (54 - 69)	-	1	2	-	-	3
Pre-operative LVB planning										
2020	Yasunga[81]	2	16	57.7 ± 14.2 (30 - 77)	IIa: 70 IIb: 30	3	15			20
2019	Pons[82]	5	77	45.5	I: 9.8 II: 73.2 III: 17.1	21	61		50	32
2018	Zeltzer[83]	1	21	39.7 (22 - 63)	-	NR		-	25	-
2017	Mazzei[84]	6	24	30 (18 - 70)	I: 13.3 II: 86.7	6	24		13	17
Comparison with scintigraphy										
2018	Bae[85]	0 1	6 6	61 ± 9 28 ± 5	II: 100 -	- -	6 -	- 7	6 7	- -
2014	Weiss[86]	13	42	41 (9 – 79)	-	27	18	-	-	83
2012	Notohamiprodjo[87]	9	21	44 ± 19	I: 23 II: 62.5 III: 12.5	NR			-	32
Non-contrast MRL										
2020b	Cellina[88]	25	25	62 (35 - 77)	I: 44 II: 24 III: 32	-	50	-	-	75
2020a	Cellina[89]	10	-	66.1 ± 5.2 (56 - 75)	-	-	10	-	-	17
2017	Cresenzi[90]	- -	25 11	62 (44 - 80) 50 (33 – 68)	0: 56 I-II: 44	-	25 -	- 11	25	36
2005	Liu[91]	27	12	(3 - 71)	-	36	2	-	1	37
PET-MR										
2019	Hou[92]	-	13	48.6 ± 9.5	-	NR		-	-	13
2017	Long[93]	2	9	49.8 ± 12.4	I: 36 II: 36 III: 28	NR		-	-	22

**Values are mean (range) or ± standard deviation; M: male; F: female; ISL: International Society of Lymphology; P: primary; S: secondary; H: healthy; UL: upper limbs; LL: lower limbs; LE: lymphedema; NR: not reported*

Supplementary table 8: Contrast agent administration and imaging methods for magnetic resonance lymphography

Author	Field (T)	Dose (mL)	Contrast agent	Type	Site	MRL	Acquisition (min post-injection)
Soga[63]	1.5	0.9	Gadoteridol (Prohance)	ic	1st–4th ids feet	3D two-point DIXON	NR
Sheng[64]	3.0	0.9	Gd-DTPA (Magnevist)	ic	2nd–4th ids hands	T1w 3D GRE with FS	Before, 20
Abdelfattah[65]	3.0	0.8	Gd-BOPTA (Multihance)	ic	1st–4th ids hands	T1w 3D GRE with FS	NR
Ripley[66] Gennaro[67]	3.0	1.0 5 mg/kg	Gd-BOPTA (Multihance) Ferumoxytol	ic iv	1st–4th ids hands or feet intravenous	3D two-point DIXON	10, 20, 30, 40, 50, 60 and 70
Jeon[68]	1.5	0.7-0.8	Gd-BOPTA (Multihance)	ic	1st–4th ids feet	T1w 3D GRE with FS	Before & 5, 10, 15, 20, 25, 30, 35 and 40
Liu[69]	3.0	< 2	Gadobutrol (Gadovist)	ic	1st–3rd ids hand(s) or feet	T1w 3D FSE with FS intermediate-w 3D FSE (VISTA)	NR
Borri[70]	3.0	0.7-0.8	Gd-BOPTA (Multihance)	ic	1st and 2nd ids hands/feet	T1w 3D GRE with FS	Before & consecutive time points after
Zhou[71]	1.5	0.9 & 0.02	Gadoteridol (Prohance)	ic	1st–4th ids hands	T1w 3D GRE with FS	Before & several time post over a period of 45 min
Liu[72]	3.0	0.7-0.8	Gd-BOPTA (Multihance)	ic	1st–4th ids feet	T1w 3D GRE with FS	Consecutive time points. 6 acquisitions leg (duration = 3 min) and 5 acquisitions in the inguinal region and thigh
Lu[73]	3.0	0.9	Gd-DPTA (Mangevist)	ic	1st–3rd ids feet	T1w 3D THRIVE with FS	Before and 20
Notohamiprodjo[74]	3.0	0.9	Gd-DTPA (Magnevist)	ic	1st–3rd ids feet	T1w 3D FLASH with FS	NR
Dimakakos[75]	1.5	0.9	Gadobutrol (Gadovist)	sc	1st–4th ids feet	T1w 3D GRE	5, 10, 15, 30, 45, 60, 90 and 120
Lohrmann[76]	1.5	1.8	Gadoteridol (Prohance)	ic	1st– 4th ids feet & pp	T1w 3D GRE (VIBE)	Before & 15, 25, 35, 45 and 55
Lohrmann[77]	1.5	1.8	Gadodiamide (Omniscan)	ic	1st–4th ids feet & pp	T1w 3D GRE (VIBE)	15 and 40
Lohrmann[78]	1.5	1.8	Gadodiamide (Omniscan)	ic	1st–4th ids feet & pp	T1w 3D GRE (VIBE)	Before & 15, 25, 35, 45 and 55
Lohrmann[79]	1.5	1.8	Gadodiamide (Omniscan)	ic	1st–4th ids feet & pp	T1w 3D GRE (VIBE)	Before & 5, 15, 25, 35, 45 and 55
Lohrmann[80]	1.5	0.9	Gadodiamide (Omniscan)	ic	1st–4th ids feet & pp	T1w 3D FLASH	Before & 5, 15, 25, 35, 45 and 55
Yasunga[81]	3.0	0.5	Meglumine gadoterate (Magnescope)	sc	1st–4th feet, base of the 1st and 5th toe & medial and lateral malleoli	T1w 3D GRE with FS	10-25, 30-45
Pons[82]	3.0	0.8	Gd-BOPTA (Multihance)	-	2nd and 4th ids	T1w 3D GRE with FS	NR
Zeltzer[83]	3.0	0.8	Gd-BOPTA (Multihance)	ic	1st–4th ids hand	T1w 3D GRE with FS	15, 30
Mazzei[84]	1.5	0.9	Gd-BOPTA (Multihance)	sc	1st – 4th ids hands or feet	T1w 3D GRE with FS	Before & 5, 20, 35
Bae[85]	3.0	0.9	Gadobutrol	ic	1st – 4th ids hand	T1w 3D GRE with FS	Every 5 min for 70 min
Weiss[86]	3.0	1.0	Gd-DPTA (Mangevist)	ic	1st – 3rd ids feet	T1w 3D GRE with FS	10, 20, 30, 40
Notohamiprodjo[87]	3.0	0.6	Gd-DPTA (Mangevist)	ic	1st – 3rd ids feet	T1w 3D GRE with FS	NR
Cellina[88]	1.5	-	-	-	-	T2w 3D TSE	-
Cellina[89]	1.5	-	-	-	-	T2w 3D FSE	-
Cresenzi[90]	3.0	-	-	-	-	3D TSE with SPIR FS	-
Liu[91]	1.5	-	-	-	-	T2w 3D TSE with FS (HASTE)	-
Hou[92]	NR	0.5	^{68}Ga-NOTA Evans Blue	sc	1st ids feet	TOF PET imaging T1W FSE with FS	20, 40
Long[93]	- 3.0	0.5 0.6 - 0.8	^{68}Ga-NOTA Evans Blue Gd-DTPA (Magnevist)	sc sc	1st ids feet	PET T1w 3D	60, 90 NR

subcutaneous; ic: intracutaneous; iv: intravenous; Gd-BOPTA: Gadobenate dimeglumine. Gd-DPTA: Gadopentate dimeglumine; VIBE: volumetric interpolated breath hold examination; GRE: gradient-recalled echo; TSE: turbo spin echo; VISTA: volumetric isotropic turbo-spin echo acquisition; FLASH: fast low angle shot; FS: fat suppression; NR: not reported

Supplementary table 9: Characteristics of included studies on ultrasound

Study information		Patient characteristics				LE type (No.)			Limbs (No.)	
Year	Author	M (No.)	F (No.)	Age* (years)	ISL stage (%)	P	S	H	UL	LL
Diagnosis										
2021	Hara[94]	0	14	59.7 (48 - 84)	I: 32.1 IIa: 25.0 IIb: 28.6. III: 14.3	-	14	-	-	28
2020	Hara[95]	0	31	62.0 (42 - 86)	I: 34.4 IIa: 13.1 IIb: 42.6. III: 9.9	1	30	-	-	61
Pre-operative LVB planning										
2020	Czedik-Eysenberg[96]	7	21	-	I: 3.8 II: 76.9 III: 19.2	10	18	-	-	28
2020	Bianchi[97]	7	19	57.6 (42 - 78)	-	-	26	-	14	12
2019	Hayashi[98]	5	25	55.7 (36 - 74)	-	-	30	-	13	17
2018	Mihara[99]	2	42	61.4 (40 - 83)	I: 25.0 IIa: 21.2 IIb: 45.0 III: 8.8	2	42	-	3	77
2018	Hayashi[100]	2	53	50.7 (32 - 84)	II: 100	-	55	-	-	55
2016	Hayashi[101]	4	22	40 (19 - 53)	-	-	-	26	-	26

**Values are mean (range) or ± standard deviation; M: male; F: female; ISL: International Society of Lymphology; P: primary; S: secondary; H: healthy; UL: upper limbs; LL: lower limbs; LE: lymphedema; NR: not reported*

Supplementary table 10: Ultrasound imaging methods and performance

Author	Imaging system	f (MHz)	Vessel diameter* (mm)	Depth* (mm)	Sensitivity (%)	Specificity (%)	Accuracy (%)	Gold standard
					Diagnostic performance			
Hara[94]	Noblus EUP-L65 (Hitachi Medical Corp.)	18	-	-	95.0	100	94.6	NIRF-L
Hara[95]	Noblus EUP-L65 (Hitachi Medical Corp.)	18	Thigh supine: 0.43 ± 0.02 Thigh upright: 0.40 ± 0.02 LL supine: 0.68 ± 0.04 LL sitting 0.63 ± 0.04 LL upright 0.63 ± 0.04	-	-	-	-	-
					Lymphatic vessel detection performance			
Czedik-Eysenberg[96]	Aplio i800 (Canon)	24	Leg: 1.15 ± 0.47	UL: 13.2 ± 3.9 LL 8.9 ± 3.5	-	90.2	-	Intraoperative findings
Bianchi[97]	Vevo MD (FUJIFILM VisualSonics)	48, 70	Significant correlation between inner and outer diameter and wall thickness between US and histology findings	-	-	-	-	Histology
Hayashi[98]	*UHFUS*: Vevo MD (FUJIFILM VisualSonics) *CHFUS*: Prosound F75 (Hitachi Medical Corp.)	18, 70	*UHFUS*: Arm: 0.336 ± 0.008 Leg: 0.417 ± 0.001 *CHFUS*: Arm: 0.403 ± 0.002 Leg: 0.468 ± 0.003	*UHFUS*: 4.6 *CHFUS*: 6.4	*UHFUS*: 94.9 *CHFUS*: 66.3	*UHFUS*: 98.3 *CHFUS*: 91.3	-	NIRF-L
Mihara[99]	Noblus EUP-L65 (Hitachi Medical Corp.)	18	-	-	T: 82.3 N: 66.7 E: 82.9 C: 85.7 S: 85.7	100	T: 46.8 N: 0 E: 62.9 C: 50.0 S: 14.2	Intraoperative findings
Hayashi[100]	Noblus EUP-L65 (Hitachi Medical Corp.)	18	0.66 ± 1.18	Groin: (<5 - 15) Thigh: (5 - 25) Knee (5 - 25) LL: (<5 - 15)	88.2	92.7	-	Intraoperative findings
Hayashi[101]	Noblus EUP-L65 (Hitachi Medical Corp.)	15	-		95.5	92.9	-	NIRF-L

**Values are mean ± standard deviation;f: frequency; LL: lower leg; UL: upper leg; NIRF-L: near infrared fluorescence lymphography; mm: millimeter*

Appendix II: MREC application process with a non-CE marked medical device

Introduction and disclaimer

This appendix describes the research set up process and the medical research ethics committee (MREC) proposal for the researcher initiated clinical research with a non-CE marked device (Acoustic X, Cyberdyne Inc., Tsukuba, Japan). This process is specifically written for the Acoustic X, a non-CE marked light emitting diode (LED) based photoacoustic (PA) and ultrasound (US) imaging system for research use. It is capable of 2D and 3D PA and US imaging at video frame rates and is suitable for structural and functional biomedical imaging in a research-setting and exploratory clinical studies.

An overview of the entire process is displayed in Supplementary figure 1 and described in the following paragraphs of this appendix. Further information outside the scope of this thesis on clinical research under the medical device regulation (MDR) can be found at https://www.ccmo.nl/onderzoekers/klinisch-onderzoek-naar-medische-hulpmiddelen and in the document 'Leidraad MDR: Review of a clinical investigation with a medical device – guidance document for MRECs'. Procedures described were in effect in the period June – September 2021 and are subject to change with time.

Create study in PaNaMa

Any clinical study conducted at the Erasmus MC must be registered in the PaNaMa database for quality management purposes, preferably in the earliest concept phase. It is a research management system for studies involving human subjects. It also helps researchers in the set-up process via workflows, actions and tasks tailored to the standard operating procedures of the Erasmus MC. Furthermore, the trial master file (TMF) and/or investigator site file (ISF) must be stored in PaNaMa in the context of Medical Research Involving Human Subjects Act (in Dutch: Wet Medisch-wetenschappelijk Onderzoek met Mensen, WMO or WMO-plichtig onderzoek). The super user of a research department can create this study in PaNaMa.

Does the MDR apply?

To determine if the MDR applies, the device must fall under the definition of a medical device (Article 2, paragraph 1 of the Medical Device Regulation (European Union, EU) 2017/745).

For the Acoustic X, the following definition applies: "Any apparatus intended by the manufacturer to be used, alone or in combination, for human beings for diagnosis, prevention, monitoring, prediction, prognosis, treatment or alleviation of disease."[102] It also does not achieve its principal intended action by pharmacological, immunological or metabolic means, in or on the human body. The Acoustic X can therefore be defined as a medical device.

Regulatory pathways for clinical investigations under the MDR

Clinical investigations under the EU MDR are subject to different articles within the MDR depending on the CE-marking status and goal of the clinical investigations with the medical device (see Supplementary figure 2). Depending on which article applies, different ethics committee or competent authority reviews the research dossier (see Supplementary table 11). For clinical research for conformity purposes (Article 62 and 74.2) with high-risk devices must be validated by the 'Centrale Commissie Mensgebonden Onderzoek' (CCMO) before assessment of specific ethical committees can take place.[103]

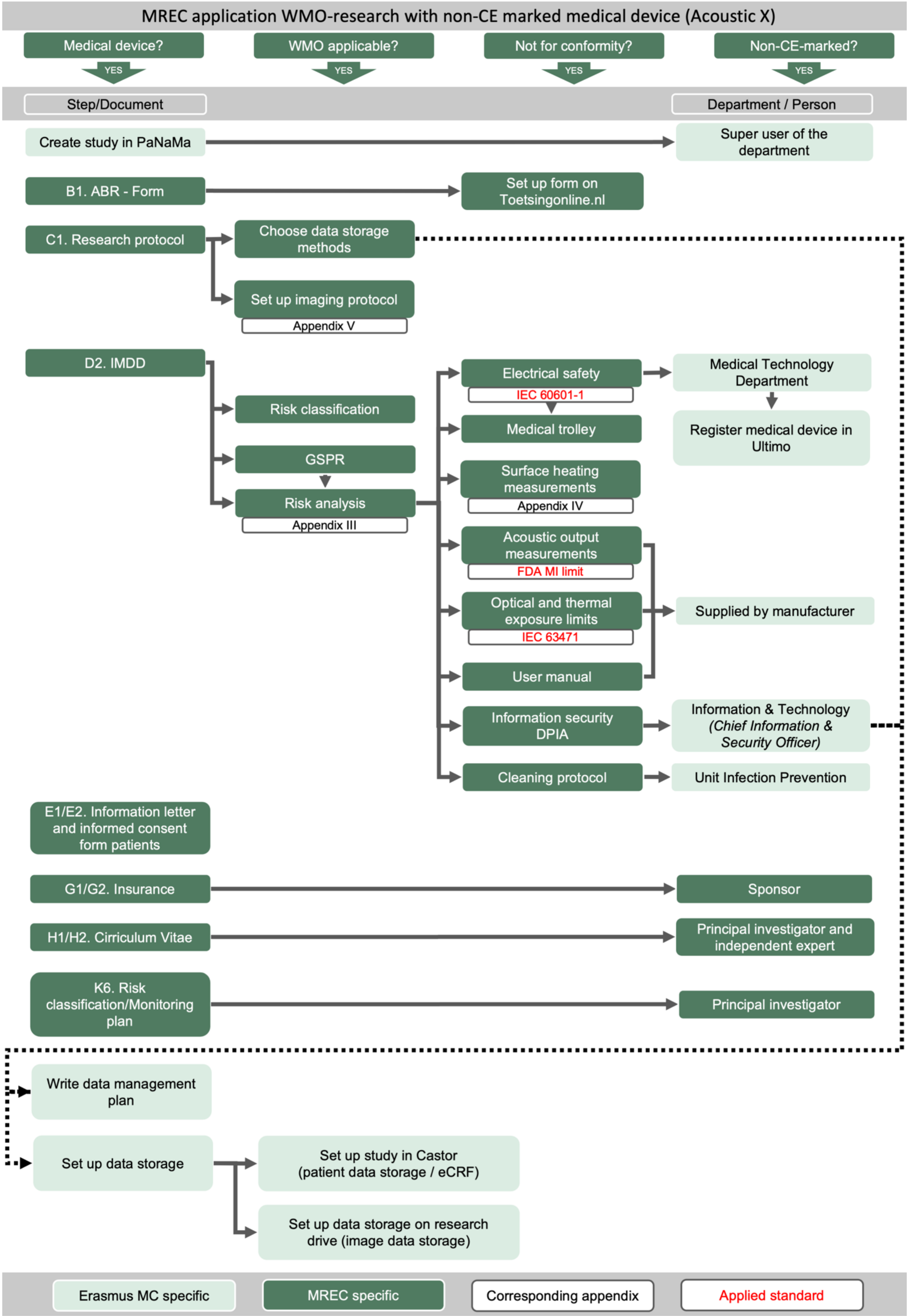

Supplementary figure 1: Workflow of study set up and MREC application process. GSPR: General Safety and Performance Requirements. IMDD: Investigational Medical Device Dossier. DPIA: Data Protection Impact Assessment. eCRF: electronic Case Report Form

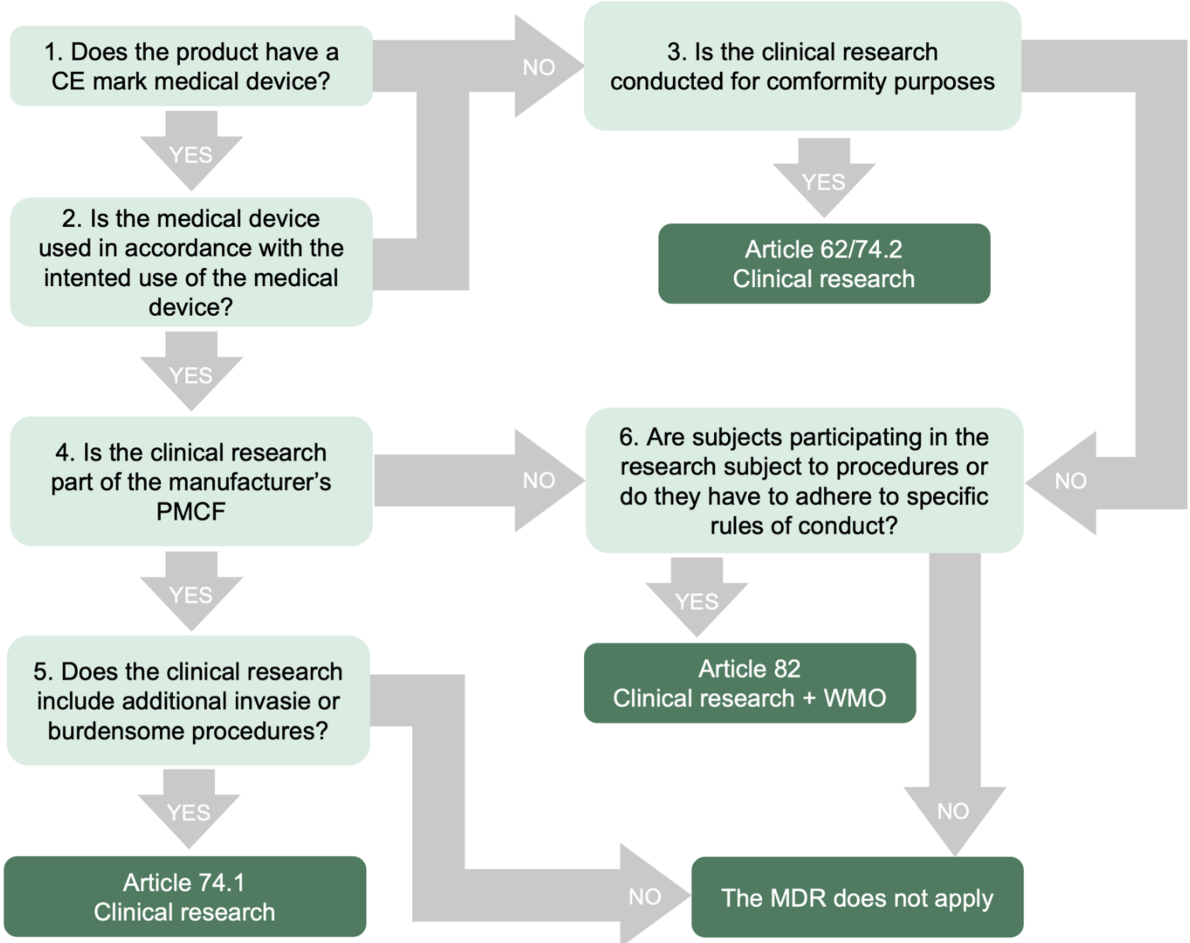

Supplementary figure 2: Clinical research under MDR - Definition and framework of regulatory pathways. Translated from ref [104]. PMCF: post market clinical follow-up. WMO: wet medisch-wetenschappelijk onderzoek. MDR: medical device regulation

Supplementary table 11: Reviewing committees per regulatory pathway

Category investigation	Class medical device	Reviewing committee
Conformity MDR article 62/74.2	Class III Class IIb invasive Class IIa invasive	Validation by CCMO and reviewing by accredited academic MREC, MEC-U
	Class IIb non-invasive Class IIa non-invasive Class I	Validation by CCMO and reviewing by accredited academic MREC
Post-market clinical follow-up investigation MDR article 74.1	All classes	Accredited MREC or CCMO
Other MDR article 82	All classes	Accredited MREC or CCMO

In case of the investigator-initiated research described in Chapter 4 of this thesis, article 82 of the MDR applies, since it the Acoustic X is a non-CE marked medical device, medical scientific research[1] is not conducted for conformity purposes or Post Market Clinical Follow-up (PMCF) and participating subjects are subjected to actions/rules of conduct are imposed on them (i.e., 'WMO-plichtig' research). The research dossier was therefore submitted directly to the MREC of the Erasmus MC.

Research dossier for MREC application with a non-CE-marked medical device

For a MREC submission the research dossier consists of several basic documents listed below. All documents are reviewed by the MREC for final approval. Templates of most documents are available on the website of the CCMO: https://www.ccmo.nl/onderzoekers/klinisch-onderzoek-naar-medische-hulpmiddelen/standaardonderzoeksdossier-medische-hulpmiddelen.

B1. ABR form

The 'Algemeen beoordelings- en registratieformulier' (ABR) form is a general assessment and registration form that can be filled in online at www.toetsingonline.nl. After completing the registration, the study gets a number in the registry starting with 'NL'.

C1. Research protocol

In this document the design and conduct of the clinical investigation are set out. The first part of the research protocol introduces the research subject, study objective, study population, outcome parameters and (statistical) analysis. This information is described in Chapter 4 of this thesis.
All (non) investigational products used for the research are also described along with the related risks and benefits (see paragraph D2. IMDD).
Further, ethical considerations such as informed consent procedures, benefit-risk analysis for participants, compensation for injury, (serious) adverse event reporting and reasons for early termination and possible compensation for participation are described.
Lastly, administrative aspects such as handling and storage of data (also present in the data management plan), monitoring and public disclosure and publication policies are reported.

D2. IMDD

The investigational medical device dossier (IMDD) specifies all items that must be covered for an application to a MREC. It is written for non-CE-marked medical devices within the scope of the MDR (EU) 2017/745, which are intended for clinical investigation. The goal of the IMDD is to give a full description of the device and essentially show how the manufacturer and the researchers ensure safe use.

The IMDD if the device is under clinical investigation in two cases:

- The device is not CE-marked, also if the device is manufactured and used only within a single health institution (in-house), or
- The device is CE-marked but used outside the intended use (only some aspects of the IMDD are applicable)

Some of the most important aspects of the IMDD for the Acoustic X are described below.

---

[1] 'Medical scientific research is research that aims to answer a question in the field of disease and health (etiology, pathogenesis, signs/symptoms, diagnosis, prevention, outcome or treatment of disease), by systematically collecting and studying of data. The research aims to contribute to medical knowledge that also applies to populations outside the direct study population.' Definition by Pols, M. *Definitie medisch-wetenschappelijk onderzoek* CCMO (2005).

Device description and specifications

Product description: The Acoustic X is a LED-based photoacoustic (PA) and ultrasound (US) imaging system for research use. Compared to conventional laser-based PA systems, Acoustic X utilizes LED arrays as tissue illumination sources. For acoustic detection a clinical grade linear array probe (7 MHz) is used. Acoustic X is capable of 2D and 3D PA and US imaging at video frame rates and is suitable for structural and functional biomedical imaging in a research-setting and exploratory clinical studies.

Performance specifications: Imaging depth – 2 cm, Spatial resolution: 250 µm, Max frame ratio - 30 Hz (max combined US + PA)

Principles of operation of the device and its mode of action: Photoacoustic imaging is a novel technique in which tissue is illuminated with short light pulses, which then gets absorbed by intrinsic optical absorbers like hemoglobin (or contrast agents like Indocyanine green if injected) to generate US signals inside the tissue. These optically generated US signals can be detected on tissue surface to generate optical absorption maps of the tissue with imaging depth and spatial resolution of pulse echo US technique. In the Acoustic X, LED arrays are used for tissue illumination.

Rationale for the qualification of the product as a device: The device falls under the definition of a medical device (Article 2, paragraph 1 of the Medical Device regulation (EU) 2017/745): “Any apparatus intended by the manufacturer to be used, alone or in combination, for human beings for diagnosis, prevention, monitoring, prediction, prognosis, treatment or alleviation of disease.” It also does not achieve its principal intended action by pharmacological, immunological or metabolic means, in or on the human body.

Risk classification: Classification according to the MDR (EU) 2017/745, Annex VIII, Chapter I: (1) the device is intended for transient use (paragraph 1.1) and (2) the device is not invasive or implantable. It is an active device[2] intended for diagnosis or monitoring, it supplies information for detecting, diagnosing, monitoring or treating physiological conditions, states of health, illnesses or congenital deformities and is powered by electricity. Classification according to the MDR (EU) 2017/745, Annex VIII, Chapter III, paragraph 6, Active devices. Paragraph 6.2, rule 10 states:

- The device is intended for diagnosis and monitoring and supplies energy which will be absorbed by the human body (optical and acoustic) outside the visible spectrum.
- The device can also image in vivo distribution of radiopharmaceuticals (e.g., indocyanine green).
- It is not intended for diagnosis or monitoring of vital physiological processes.
- It does not emit ionizing radiation

The Acoustic X can therefore be classified as Class IIa medical device.

Key functional element, list of configuration and accessories of the device: Supplementary figure 3 gives on overview of the device and its components. Supplementary figure 4 gives an overview of the internal communication between different components of the device and processing steps. Only one

[2] ‘Active device’ means any device, the operation of which depends on a source of energy other than that generated by the human body for that purpose, or by gravity, and which acts by changing the density of or converting that energy. Devices intended to transmit energy, substances or other elements between an active device and the patient, without any significant change, shall not be deemed to be active devices.

configuration of the device is used for the clinical study, namely with the 7 MHz ultrasound probe and 820/940 nm LED arrays. For providing good acoustic coupling between tissue and Acoustic X probe, a custom-made US gel pad will be used. This is a non-irritating medical grade gel pad with a solid hydrogel layer.

Reference to previous and similar generations of the device: There are no previous generations of the device. Other comparable devices in the EU and international markets are the MSOT Acuity by iThera Medical (https://www.ithera-medical.com/products/msot-acuity/) and Imagio by Seno Medical (https://senomedical.com/). In both these systems, tissue is illuminated using pulsed lasers, which are bulky and expensive. In addition, when using these laser-based systems, they must be installed only in special laser-safe rooms users and patients must protect their eyes using laser safety goggles, because of eyes safety concerns.
Compared to these systems, Acoustic X is different as it uses LEDs with low optical output (orders of magnitude lower than a laser) for illuminating tissue and thus is safe for skin and eyes.

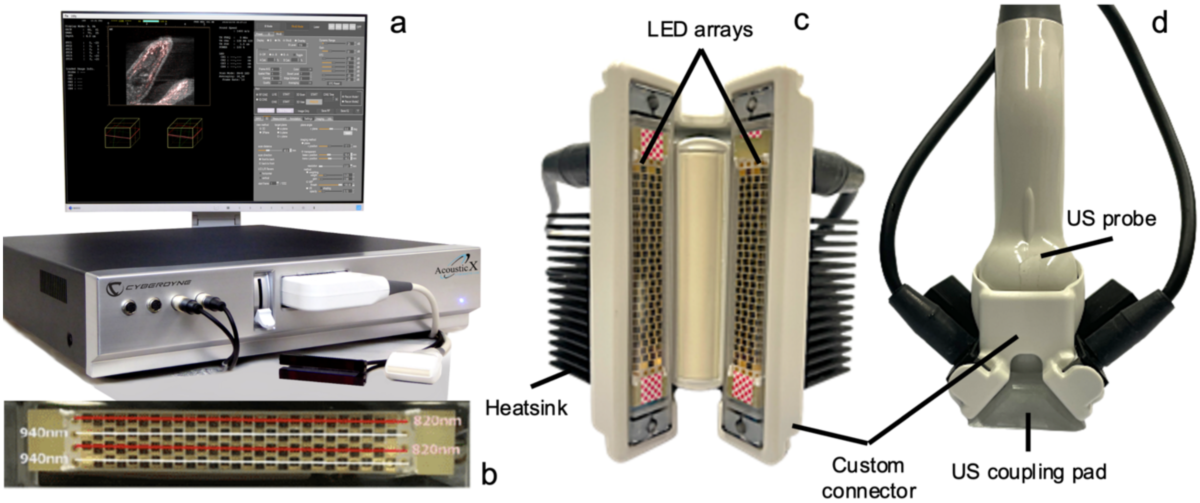

*Supplementary figure 3: Photograph of **(a)** AcousticX system, **(b)** internal details of 820nm/940nm combination LED array, row 1 and row 3 are embedded with 820 nm elements and row 2 and row 4 with 940 nm elements.*
***(c)** view of arrangement of LED arrays connected to the US probe, **(d)** side view of the LED arrays connection to US probe, light from LED arrays approximately fall on the focus of US probe and US coupling is done with a custom-made gel pad*

Information to be supplied by the manufacturer

The manufacturer must provide the instructions for use in the languages accepted in the Member States where the device is envisaged to be sold and have documentation on all device elements and its serial number, labels and packaging. This documentation was provided to the MREC but is not included in this thesis.

Design and manufacturing information

If applicable, all design stages and steps of the manufacturing process must be described. The complete information and specifications, including the manufacturing processes and their validation, their adjuvants, the continuous monitoring and the final product testing have to be given.
In our case (i.e., researcher-initiated research), we do not have a complete insight into the design and fabrication processes in detail since the manufacturer (Cyberdyne) is a commercial company providing the device for our research.

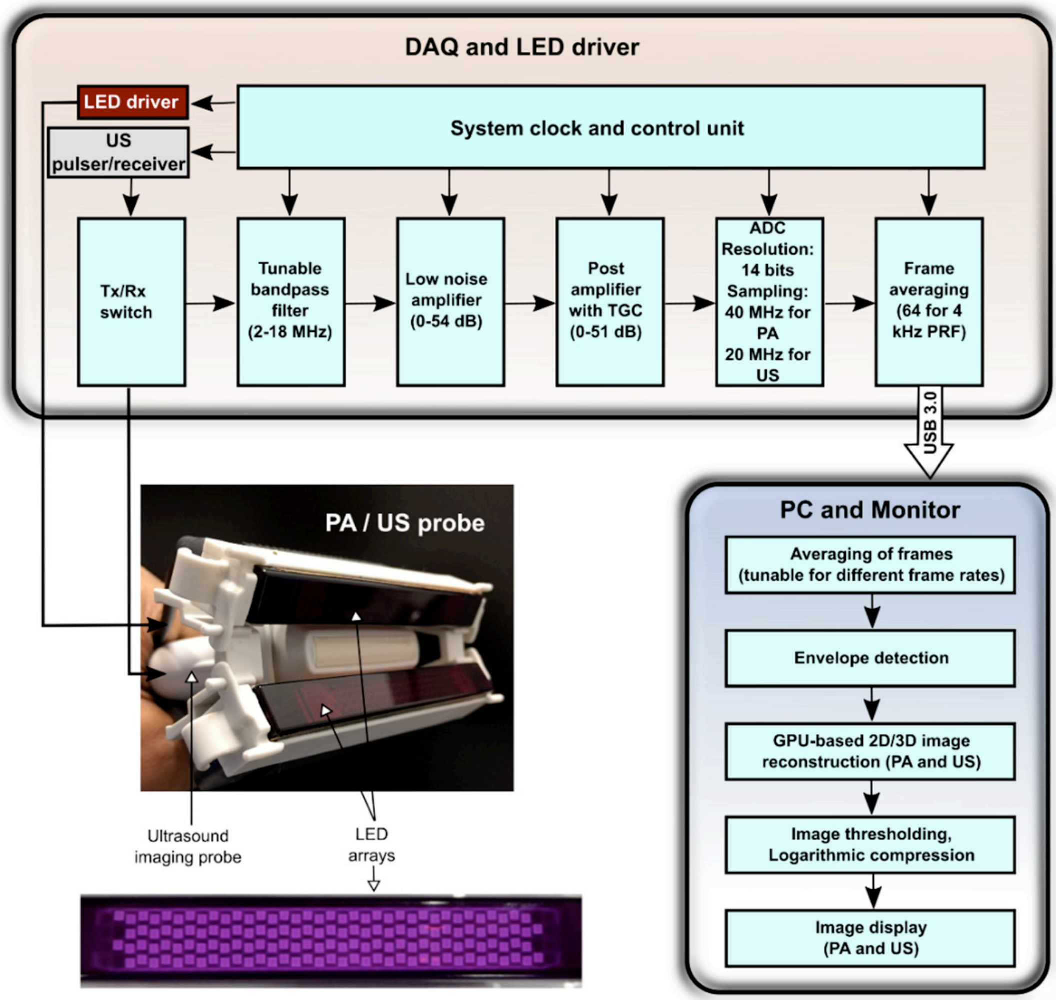

Supplementary figure 4: Block diagram of the light-emitting diode (LED)-based photoacoustic (PA) and ultrasound (US) imaging system. Middle left: photograph of the arrangement of the two LED arrays and the US imaging probe. The two arrays are positioned on both sides of the US imaging probe, angled towards the imaging plane. Bottom left: photograph of an LED array (wavelength: 850 nm). It consists of four rows of 36 LEDs (dimensions: 1 mm x 1 mm). DAQ: data acquisition; Tx: transmit; Rx: receive; TGC: time gain compensation; ADC: analog-to-digital converter; PRF: pulse repetition frequency; USB: universal serial bus; PC: personal computer; GPU: graphics processing unit. Reprinted from ref[105].

General safety and performance requirements

The documentation contains information for the demonstration of conformity with the general safety and performance requirements set out in Annex I or the MDR that are applicable to the device taking into account its intended purpose and includes a justification, validation and verification of the solutions adopted to meet those requirements.

Benefit-risk analysis and risk management

One of the most important aspects of the IMDD is the risk analysis. Here all potential risks of the device are described and what is done to mitigate or eliminate the risk. Table C.1 of NEN-EN-ISO 14971:2019 gives an extensive overview of potential hazards that should be addressed.

Types of risk that must be covered (if applicable) are:

- Energy hazards: acoustic, electric, mechanical, potential (stored) and radiation energy
- Biological hazards and chemical hazards from biological, chemical or immunological agents
- Functionality and information hazards such as data, delivery and diagnostic information hazards

Appendix III contains the complete risk analysis for the Acoustic X.

E1/E2 Research subject information and informed consent forms

Informed consent is required for the participation of a subject in medical scientific research. This is a process where oral and written information, exchange of views and asking questions are very important. The aim of the process and the written information is to inform the potential subjects in such a way that they can make an informed choice about whether to participate in the study.

G1/G2 Insurance

The sponsor/investigator must always have a liability insurance which is in accordance with article 7 of the WMO. Depending on the risk of the research a WMO-subject insurance must be taken out. For the clinical research with the Acoustic X described in Chapter 4 of this thesis, participation in this research does not impose any risks on the patient. The MREC Erasmus MC has given dispensation from the statutory obligation to provide insurance for subjects participating in medical research (article 7, subsection 6 of the WMO and Medical Research (Human Subjects) Compulsory Insurance Decree of 23 June 2003).

H1/H2 Curriculum Vitae

Recent resume for review from the independent expert and the principal investigator (dated and signed) must be submitted.

K6 – Research Risk classification

Supplementary table 12: Risk Matrix

Probability of occurrence	Extent of damage		
	Light damage	Mild damage	Serious damage
Small chance	Negligible risk	Negligible risk	Intermediate risk
Moderate chance	Negligible risk	Intermediate risk	High risk
Likely	Intermediate risk	High risk	High risk

For clinical research a risk classification is done based on the extent to which a research participant runs additional risk, which depends on the chance, seriousness, treatability and reversibility of the damage that occurs. This concern possible physical (e.g., pain, discomfort), social (e.g., fear, stress) and psychological (e.g., privacy, stigma, insurability) risks. It may also be that the risk of harm and its degree of severity are different for research participants and for some groups (severely ill, acutely ill, the elderly, children, psychiatric patients, addicts) or in some situations (multicenter, multidisciplinary, polypharmacy, inexperienced research team). Supplementary table 12 shows the risk matrix used for risk classification of the proposed research. Based on the risk classification, a monitoring plan must be drawn up. The higher the risk classification, the more frequent monitoring takes place.

The clinical research with the Acoustic X described in Chapter 4 of this thesis was classified as ‘negligible risk’.

Appendix III: Risk analysis Acoustic X

Scope

This Risk Analysis covers all potential hazards identified that could lead to harm to either a human subject or the operator of the system, when used within the intended use statement and other guidelines given below. The authors compiled who this document came from a wide variety of background (Researchers with medical background, Researchers with technical backgrounds and physicians) and based the contents on the advice of the Medical Technology Department of the Erasmus MC, University Medical Center Rotterdam.

Intended use

LED-based photoacoustic (PA) and ultrasound (US) imaging system for research use. Compared to conventional laser-based PA systems, Acoustic X utilizes LED arrays as tissue illumination sources. For acoustic detection clinical-grade linear array probe (7 MHz) is used. Acoustic X is capable of 2D and 3D PA and US imaging at video frame rates and is suitable for structural and functional biomedical imaging in a research-setting and exploratory clinical studies.

Hazard identification and estimation of risks

Severity Level

Severity Levels are defined based on the level of harm that could occur to either the patient or the operator of the system, as listed in Supplementary table 13.

Supplementary table 13: Severity level definition

Severity level	Definition
Catastrophic	Results in death of subject or operator
Critical	Results in permanent impairment or life-threatening injury
Serious	Results in injury or impairment requiring professional medical intervention
Minor	Results in temporary injury or impairment not requiring professional medical intervention
Negligible	Annoyance, inconvenience, or temporary discomfort

Probability of occurrence

The probability of occurrence is defined as the probability the event will occur during the examination of a patient. In a clinical setting 1-5 patients are imaged over the course of 1 day. The probability of occurrence ranges is listed in Supplementary table 14.

Supplementary table 14: Risk probability level definition

Probability level	Probability
Frequent	> 1 in 5
Probable	1 in 5 – 1 in 10
Occasional	1 in 10 – 1 in 1000
Remote	1 in 1000 – 1 in 1.000.000
Improbable	< 1 in 1.000.000

Relative risk level definition

Based on these definitions of Severity and Probability of Occurrence, individual Relative Risk Levels are defined using a Relative Risk Category, based on the risk evaluation table shown below.

Relative Risk Levels have been grouped into three Relative Risk Categories of Unacceptable, Marginal, and Acceptable, as defined here.

- **UNACCEPTABLE:** Relative Risk Levels, highlighted in red in the table, are not acceptable. Additional risk control measures must be taken to reduce the severity and/or probability of the associated hazard.
- **MARGINAL:** Relative Risk Levels, highlighted in yellow in the table, must be evaluated carefully to determine if a reduction in Relative Risk is feasible. At a minimum, documentation must be provided to the users of the system to warn them of every potential hazard with a marginal Relative Risk Level.
- **ACCEPTABLE:** Relative Risk Levels, highlighted in green in the table, represent acceptable levels of risk. No additional evaluation or risk control measures are required.

Supplementary table 15: Relative risk level definition

Probability	Severity				
	Catastrophic	Critical	Serious	Minor	Negligible
Frequent					
Probable					
Occasional					
Remote					
Improbable					

Listing of identified hazards, risk evaluation and risk control

For each hazard listed below in Supplementary table 16, the identified risk and risk level are followed by risk control and mitigation measures.

Supplementary table 16: Risk analysis Acoustic X

Hazard	Type	Description	Severity	Probability	Acceptable (Yes/No)	Mitigation measures
Electrical shock due to fault in AC line	Energy (Electrical)	Fault in AC line may result in electric shock for the user who is touching the AcousticX data acquisition system (DAS).	Minor	Remote	Yes	The AC line input devices and wiring methods used in the AcousticX system conform to related standards for use as laboratory test equipment, reducing minor single fault situations. In the event of an AC line isolation fault, the fault current will be shunted to ground through the direct connection of the system chassis to the AC line power ground conductor, and thus the operator would not be exposed to a potential of more than a few volts from contact with the system chassis or other grounded components. Electrical safety was tested by the medical technology department of the Erasmus MC. They also deemed the device to be electrically safe according to IEC 60601-1 and registered the device into the maintenance system including test results.
Electrical shock from LED arrays driven by high voltage electronic drivers	Energy (Electrical)	LED arrays in AcousticX are driven by high voltage circuits (400 Volts). Any leakage in cables or the array itself may result in electric shock for the user or subject under evaluation.	Minor	Improbable	Yes	AcousticX DAS is fully enclosed within a grounded metal chassis and covers, there is no chance of user contact other than at the external connector interfaces to the system. The only location at which the user could come into contact with voltages from the internal 400 V. Power supplies are the LED array head and connecting cables which are well insulated to be even used in water-based setups.

Electrical shock from US probe driven by high voltage electronic drivers	Energy (Electrical)	US probe in AcousticX is driven by high voltage circuits for acoustic transmission. Any leakage may result in electric shock for the user or subject under evaluation.	Minor	Improbable	Yes	Acoustic X DAS is fully enclosed within a grounded metal chassis and covers, there is no chance of user contact other than at the external connector interfaces to the system. The only location at which the user could come into contact with voltages from the internal power supplies is the US probe connector. Power at this port will be active when a US probe is connected and locked in to provide extra safety in this regard. Also, US transmission will start only once the user press start button in the AcousticX GUI.
Tissue heating or damage caused by US exposure in tissue	Energy (Acoustic)	During US imaging, high acoustic pressure on tissue may cause irritations or damage to tissue.	Minor	Improbable	Yes	Since US imaging is also performed using AcousticX, it is important to keep the transmitted acoustic energy well below the allowed limits to avoid tissue burns or irritations. MI (mechanical index) is a unitless number that can be used as an index of cavitation bio-effects; a higher MI value indicates greater exposure. Levels below 0.3 are generally considered to have no detectable effects. Currently the FDA stipulates that diagnostic US scanner cannot exceed a mechanical index of 1.9. In AcousticX, MI is 0.274 when using 7 MHz probe at a frame rate of 15 Hz, and this is fixed in software and hardware (fixing transmission voltage) eliminating any risks.
Damage to eyes and skin caused by pulsed light exposure.	Energy (Optical, non-ionizing radiation)	During PA imaging, pulsed light exposure directly on eyes or skin may cause damage.	Minor	Remote	Yes	Compared to conventional PA imaging systems using solid-state lasers or laser diodes, eye and skin safety of the subject and the user is not a major concern. Since we propose to use LED arrays as illumination source, we do not foresee any issues in this direction. Considering the pulse energy, beam shape, and repetition rates, light exposure on skin is expected to be far lower than the maximum permissible exposure for humans (0.11 mJ/cm^2 when using current prototype of LED arrays). The LED-based PA imaging system described here is safe for both skin and eye exposure. Since LED emissions are incoherent, the ANSI safety limits for collimated laser beams do not apply. Instead, the international electrotechnical commission (IEC) 62471 is followed. According to IEC 62471, the exposure limit for skin is based on thermal injury due to the temperature rise in tissue. Assuming that the illumination on the same skin area lasts continuously for 5 seconds using two LED bars (820/940 nm) working at 4 kHz pulse repetition rate, the estimated exposure is 4.57×10^3 W/m^2 which is below the thermal hazard limit for skin of 5.98×10^3 W/m^2. For eye safety, two aspects need to be considered, which are retinal thermal hazard exposure limit (weak visual

						stimulus) and infrared radiation eye safety limit. Assuming a continuous illumination at the front of the eye for 5 seconds using two 820/940-nm LED bars working at 4 kHz pulse repetition rate, the estimated exposures are 2.92×10^3 W/m^2/sr for retinal thermal exposure and 4.57×10^3 W/m^2 for infrared radiation exposure, both lower than the safety limits for eye of 1.34×10^5 W/m^2/sr and 5.38×10^3 W/m^2, respectively.
Electrical hazardous condition resulting from liquid spills onto or into system	Energy (Electrical)	Liquid spilling on to the DAS of AcousticX may cause serious problems in electronic boards inside.	Major	Occasional	Marginal	AcousticX system enclosure and internal hardware design is not intended to provide any level of protection from liquid spills. Exposure to a spill could significantly disrupt system functionality, including the performance of risk control features identified elsewhere in this document, and thus subject the user and imaging subject to an increased Relative Risk Level. Making the DAS waterproof is not an option as this may have serious impact in water-cooling. If the user follows the suggested guidelines, the probability of harm will be dramatically reduced.
Tissue heating or damage caused by high temperature on probe head generated by heating of LED arrays.	Energy (Thermal)	LED elements are driven at high pulse repetition rate (4 KHz) which results in increase in temperature on LED array head, consequently resulting in tissue heating/damage.	Minor	Occasional	Marginal	The manufacturer recommends not to continuously acquire data for more than 10 seconds to avoid excessive heating, especially when there is no water coupling used. If the user follows the suggested guidelines, the probability of harm will be dramatically reduced. Since measurements of 2 minutes will be done in the proposed study. Additional self-heating measurements were conducted to ensure that the device surfaces stayed below safe temperatures during the intended use. Surfaces in direct contact with the patient reached a maximum temperature of 25.7 degrees Celsius and the hottest surface (heat sinks) reached maximum temperatures of 50.3 degrees Celsius. This surface is only incidentally touched by the user. Both temperatures are below the allowed surface temperatures defined in IEC 60601-1.
System malfunction because of a software crash	Functionalit y (software)	AcousticX software may crash and lose its connectivity with the DAS hardware resulting in unwanted/uncontrol led optical or acoustic energy on subjects.	Minor	Improbable	Yes	AcousticX system is capable of sensing software crashes and consequently shutting down the acoustic and optical transmission. On top of this, user must immediately restart the AcousticX PC so that sound and light transmission will be reinitiated in a safe manner (PA and US imaging will be started only when the user clicks on Start acquisition in the GUI)

Image artifacts in shallow depths (1-5 mm) from the probe surface.	Functionality (artifacts)	PA signals will be generated on AcousticX probe surface itself because of optical absorption by LED arrays itself and also by vibrations caused by high voltage pulsing.	Negligible	High	Yes	These artifacts are unavoidable in live measurements. However, considering that the sensitive area for acoustic detection is after 10 mm (considering acoustic focus of US probe), it is recommended for the user to have a minimum gap of 1 cm between the probe and tissue surface. In this case, no features will be hidden by artifacts. In Cine mode, AcousticX offers a special feature 'skin suppression' in which anything above the skin surface (detected using US images) can be suppressed and this feature will be helpful to get rid of these artifacts.
Unauthorized persons can access the data.	Data (access)	Unauthorized personnel or other persons access the patient data stored on the device.	Serious	Improbable	Yes	The device will be kept in locked rooms outside its use to which only authorized users have access. Moreover, the device is protected by a password to make sure only authorized user can access the data. Furthermore, the device will not be connected to any network to prevent access from the outside.
Data loss during transfer	Data (transfer)	Data is lost after transfer from the device to an external hard drive.	Minor	Remote	Yes	Data can only be transferred via an external hard drive. The device cannot be connected to a network. Data should only be deleted from the device once a backup of the data has been made elsewhere. Ideally a second person checks if all the data has been transferred and backed-up before data is deleted from the device.
Data on the device are traced back to a patient	Data (confidentiality)	Data on the device are saved in such a way (for example with patient identifiable information in file names) so the data can be traced back to the patient.	Serious	Improbable	Yes	Only authorized users can obtain patient data. For good clinical research practice, data obtained with the device should be stored in an anonymized or pseudonymized way. This way data cannot be directly traced back to a patient.
Cleaning of the coupling pad, probe and LEDs	Biological/immunological	The user forgets to clean the device in between use	Negligible	Occasional	Yes	Only trained users that know the cleaning protocol should use the device. The chance of harm is very small since the device is only used in a non-sterile environment on the skin surface. The entire device and accessories can be cleaned with a damp cloth and 70% alcohol. The cleaning protocol was also discussed and approved by the unit infection prevention of the Erasmus University Medical Center.
Wrong connection of the LEDs	Mechanical	The user tries to connect the LEDs to other outlets	Serious	Improbable	Yes	The plug connections are designed in such a way that they are unique and can only be connected in one way. This prevents the user from connecting the LEDs to other plugs or other cables to the LEDs plug connections.
Wrong connection of the ultrasound transducer	Mechanical	The user tries to connect the ultrasound probe to other outlets	Serious	Improbable	Yes	The connections are designed in such a way that they are unique and can only be connected in one way. This prevents the user from connecting the ultrasound probe to other outlets or other cables to the ultrasound outlets. The ultrasound probe is also secured in the outlet with a locking system.

Breakage of the LED connector	Mechanical	The user drops the connector which can cause it to break	Minor	Improbable	Yes	If the connector breaks the device cannot be used until a new connector is available. The user is trained not to use the device when it is broken. The user will contact the manufacturer to obtain a new connector.
Burning/fire hazard	Thermal	The user forgets to turn off the device after use causing it to heat excessively and burn the surface it lays on.	Serious	Remote	Marginal	A checklist will be built into the imaging protocol that makes sure that the device is turned off directly after use. For this, two trained researchers have to be present to ensure the safety checks are done.
Electrical hazard due to use of damaged LEDs	Mechanical and electrical	The user breaks the LEDs and uses the device while broken. This can cause electrical shock when inside parts of the LEDs can be touched.	Critical	Improbable	Marginal	The user is trained to not use the device when it is broken. It is also written in the user manual. Only trained users who are part of the research team are allowed to operate the device.
Electrical hazard due to use of damaged ultrasound probe	Mechanical and electrical	The user breaks the ultrasound probe and uses the device while broken. This can cause electrical shock when inside parts of the probe can be touched.	Critical	Improbable	Marginal	The user is trained to not use the device when it is broken. It is also written in the user manual. Only trained users who are part of the research team are allowed to operate the device.

Appendix IV: Surface heating measurements Acoustic X

Scope

This appendix provides surface heating measurements and the associated analysis regarding the safety of the Acoustic X transducer and LEDs and specified imaging settings. These measurements cover potential hazards, because of self-heating of the LEDs, that could cause harm. Outcomes are compared to established surface heating standards for different material types. The results show that the self-heating of the LEDs of the Acoustic X system fall within the safety limits.

Ultrasound transducer characteristics

Array type	Linear
Transmit frequency	7 MHz
Manufacturer	Cyberdyne Inc.

LED characteristics

LED strips	High-Density High-Power LED
Wavelength	820 and 940 nm
Pulse width	70 ns
Frequency	4 kHz
Manufacturer	Cyberdyne Inc.

Photoacoustic system

System	Acoustic X
Manufacturer	Cyberdyne Inc.
Frame rate	30 Hz
PA processing channels	128
Driver ports	4
Power AC	100 V – 240 V

Standards

Several safety standards are listed in Supplementary table 17 that define maximum allowable temperatures of several materials. These standards are used in this document to determine if the device can be used safely under the intended use based on thermal measurement outputs.

Supplementary table 17: Surface heating standards Yellow are the standards applicable to the heat sink and green are the standards applicable to the gel pad.
(source: https://slpower.com/data/collateral/AN_Maximum_Allowable_Temperature.pdf).

<table>
<tr><th></th><th>Part</th><th>Metal</th><th>Vitreous Material (glass, ceramics etc.)</th><th>Plastic, Rubber</th><th>Coated Metal (non-metallic paint)</th></tr>
<tr><td rowspan="3">IEC 60950-1:2005 Table 4C – Touch/surface limits</td><td>Handles, knobs, grips etc. continuously in normal use</td><td>55 ℃</td><td>65 ℃</td><td>75 ℃</td><td>-</td></tr>
<tr><td>Handles, knobs, grips etc. Held or touched for short periods</td><td>60 ℃</td><td>70 ℃</td><td>85 ℃</td><td>-</td></tr>
<tr><td>External surfaces or parts inside the equipment that may be touched</td><td>70 ℃</td><td>80 ℃</td><td>95 ℃</td><td>-</td></tr>
<tr><td rowspan="2">IEC 61010-1:2010 Table 19</td><td>Handles and knobs held or touched in normal use</td><td>55 ℃</td><td>65 ℃</td><td>70 ℃</td><td>70 ℃</td></tr>
<tr><td>Outer surface of enclosure touched unintentionally</td><td>65 ℃</td><td>80 ℃</td><td>85 ℃</td><td>80 ℃</td></tr>
<tr><th></th><th>Part</th><th>Contact duration for a time ‘t’</th><th>Metal and liquids</th><th>Glass, Porcelain, Vitreous Material</th><th>Plastic, Rubber, Wood, Molded Material</th></tr>
<tr><td rowspan="7">IEC 60601-1</td><td rowspan="4">Medical electrical equipment</td><td>t < 1 s</td><td>74 ℃</td><td>80 ℃</td><td>86 ℃</td></tr>
<tr><td>1 s ≦ t ≦ 10 s</td><td>56 ℃</td><td>66 ℃</td><td>71 ℃</td></tr>
<tr><td>10 s ≦ t ≦ 1 min</td><td>51 ℃</td><td>56 ℃</td><td>60 ℃</td></tr>
<tr><td>1 min ≦ t</td><td>48 ℃</td><td>48 ℃</td><td>48 ℃</td></tr>
<tr><td rowspan="3">Applied part having contact with patient</td><td>t < 1 min</td><td>51 ℃</td><td>56 ℃</td><td>60 ℃</td></tr>
<tr><td>1 min ≦ t ≦ 10 min</td><td>48 ℃</td><td>48 ℃</td><td>48 ℃</td></tr>
<tr><td>10 min ≦ t</td><td>43 ℃</td><td>43 ℃</td><td>43 ℃</td></tr>
</table>

Methods

During the intended use a gel pad used for acoustic coupling is in continuous contact with the patient’s skin. Heatsinks on the back surface of the LEDs are made to cool down the LEDs and can get warm. During normal use these are not in contact with either the patient’s or the user’s skin. The heatsinks may be touched unintentionally for a brief period ($t < 1$ second). The heatsinks are metal and the coupling pad falls under the plastic/rubber material category.

Therefore, the temperature increase of the heat sinks was tested in a series of three consecutive measurements with an infrared inferred temperature measurement with a thermal camera (Fluke Ti125). Every measurement was 4 minutes. The first 2 minutes the device was turned on, then the device was turned off for the second half of the measurement to monitor the cooling. The temperature was registered every 10 seconds. The starting temperature differed for every series:

- Series 1: start at base temperature of device (not turned on before).
- Series 2: start at the final temperature of series 1.
- Series 3: start at the final temperature of series 2.

Heating of the gel pad was measured for three minutes with the device turned on. The temperature was monitored every 10 seconds.

See Supplementary figure 5 for images of the measurements set up.

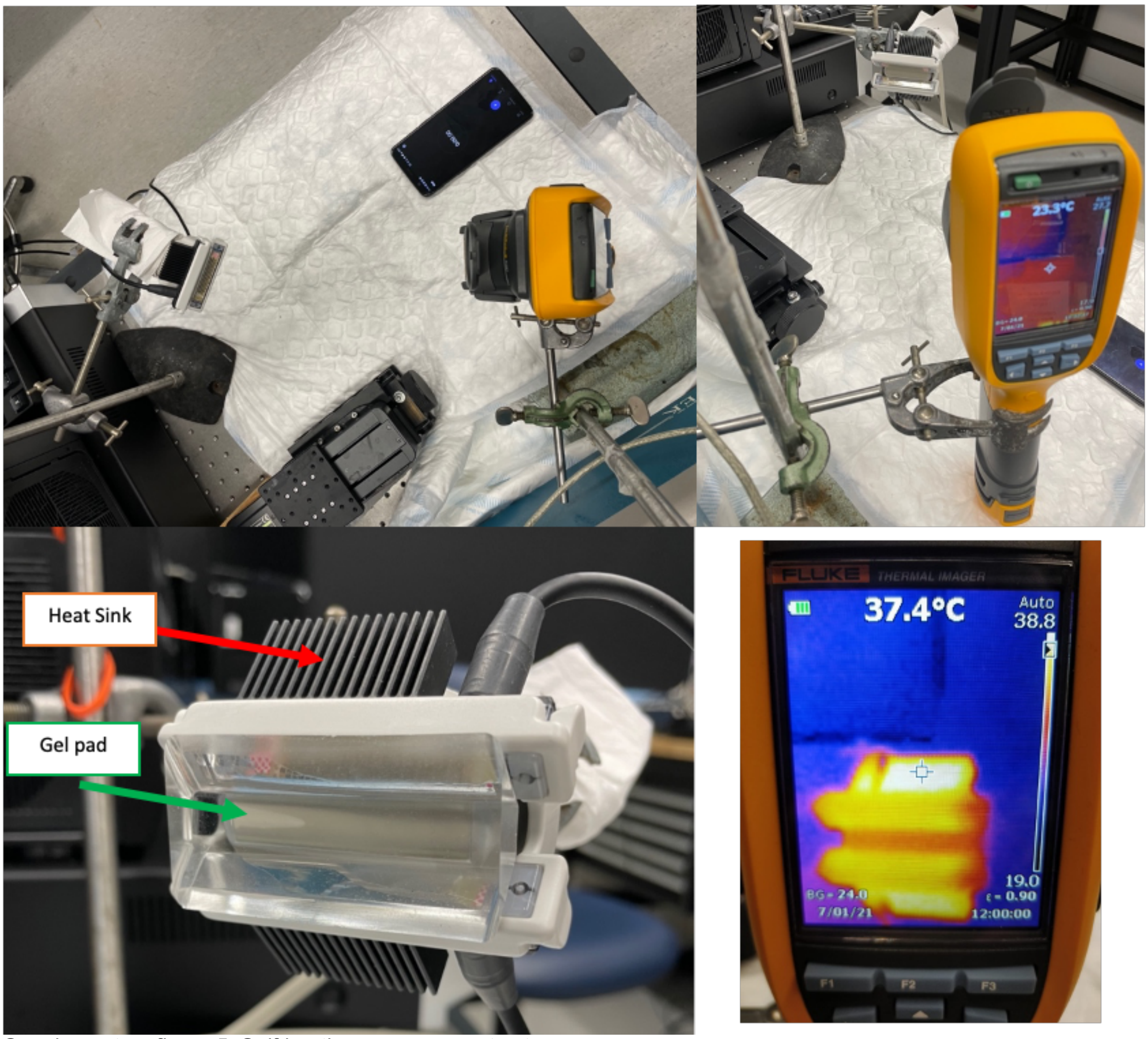

Supplementary figure 5: Self heating measurement set-up

Results

Supplementary figure 6 shows the monitored temperature during the measurement series of the heat sinks and Supplementary table 18 shows the total temperature increase and decrease, and maximum temperatures reached during the measurements. The recorded temperature of the gel pad surface can be seen in Supplementary figure 7. The maximum temperature of the gel pad was 25.7 ℃.

Supplementary table 18: Total temperature increase, decrease and maximum temperature during the measurements

	Temperature increase (After 2 minutes)	Temperature decrease (After 2 minutes)	Maximum temperature
Series 1	14.9 ℃	4.6 ℃	38.0 ℃
Series 2	12.0 ℃	6.4 ℃	45.4 ℃
Series 3	11.3 ℃	8.3 ℃	50.3 ℃

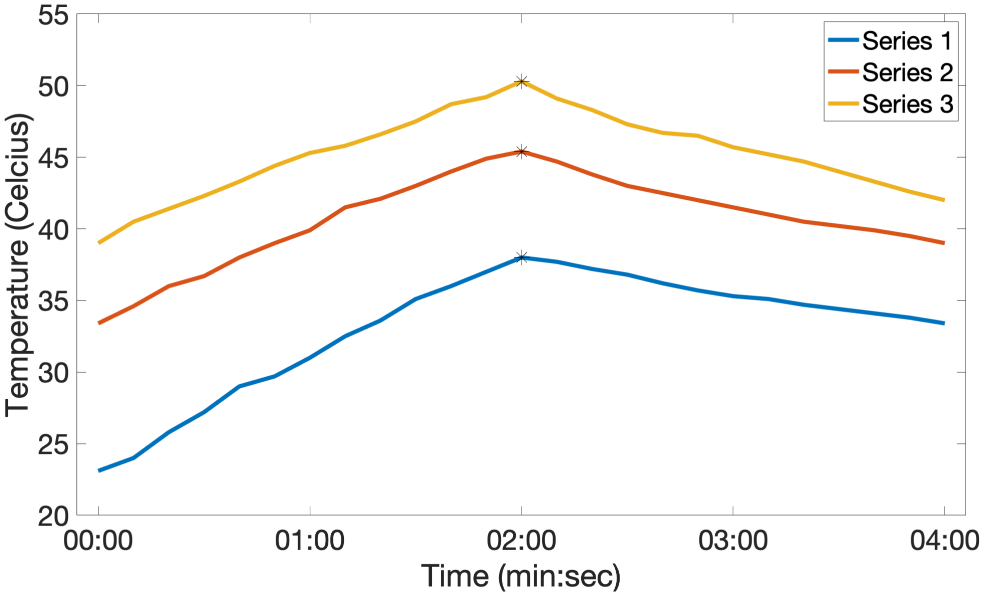

Supplementary figure 6: The recorded temperature of the heat sinks for three series of 4-minute measurements. For the first half of the measurement the device is on, for the second half the device was off. The moment that the device is turned off is marked with the black star

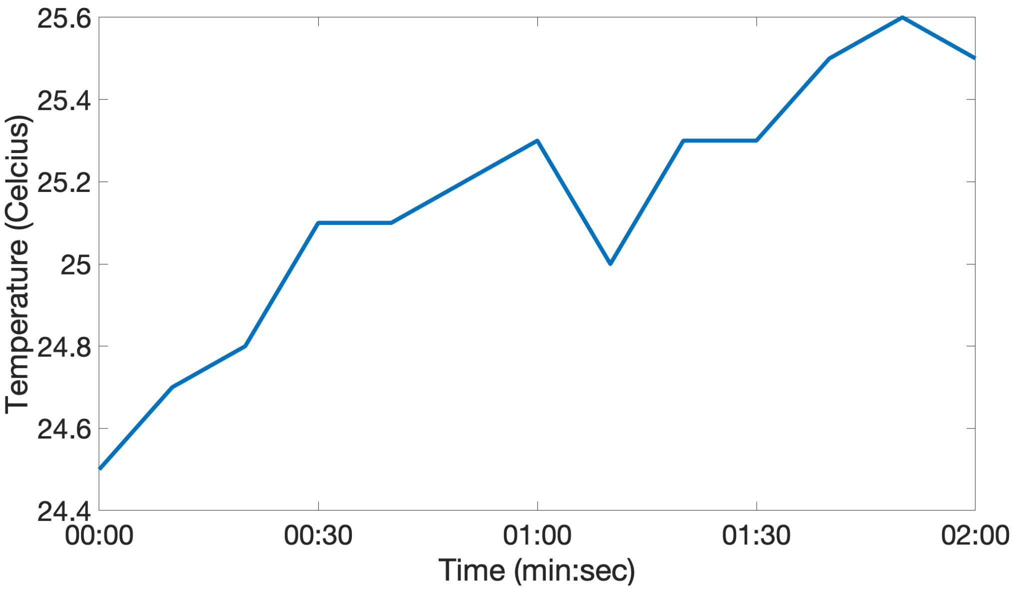

Supplementary figure 7: The recorded temperature of the gel pad surface during a three-minute measurement.

Conclusions

These results show that the self-heating of the Acoustic X device (as a result of heat formation in the LEDs), given the reported protocol, falls within the safety limits specified in Supplementary table 17 (yellow for the heat sinks and green for the gel pad). The software controlling the LEDs and ultrasound transducer will ensure that the transmission settings to not exceed the maximum values listed in this report.

Appendix V: Imaging protocol

Introduction

This document described the entire imaging protocol step by step for the PAI lymph study.

Data storage structure

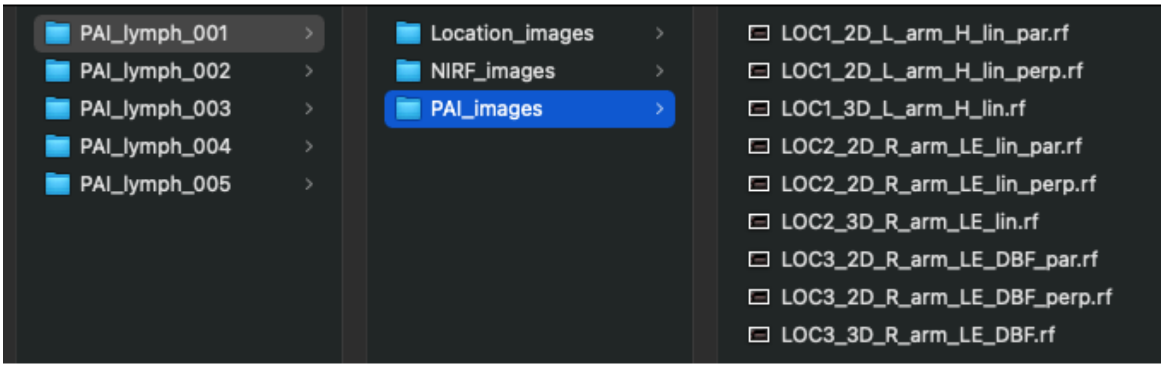

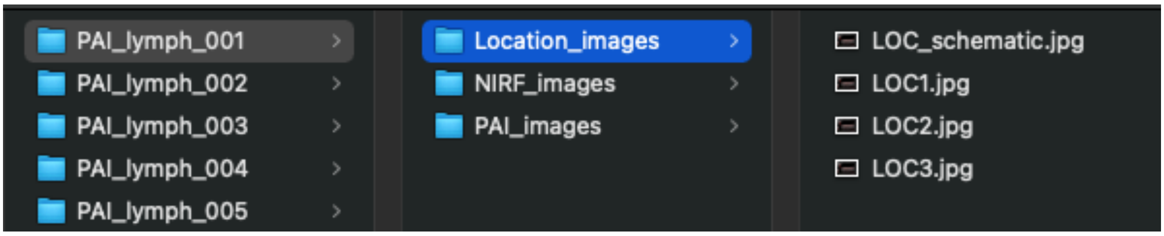

Near infrared fluorescence (Photodynamic Eye) image protocol

Near infrared lymphography is executed conform the regular imaging protocol.

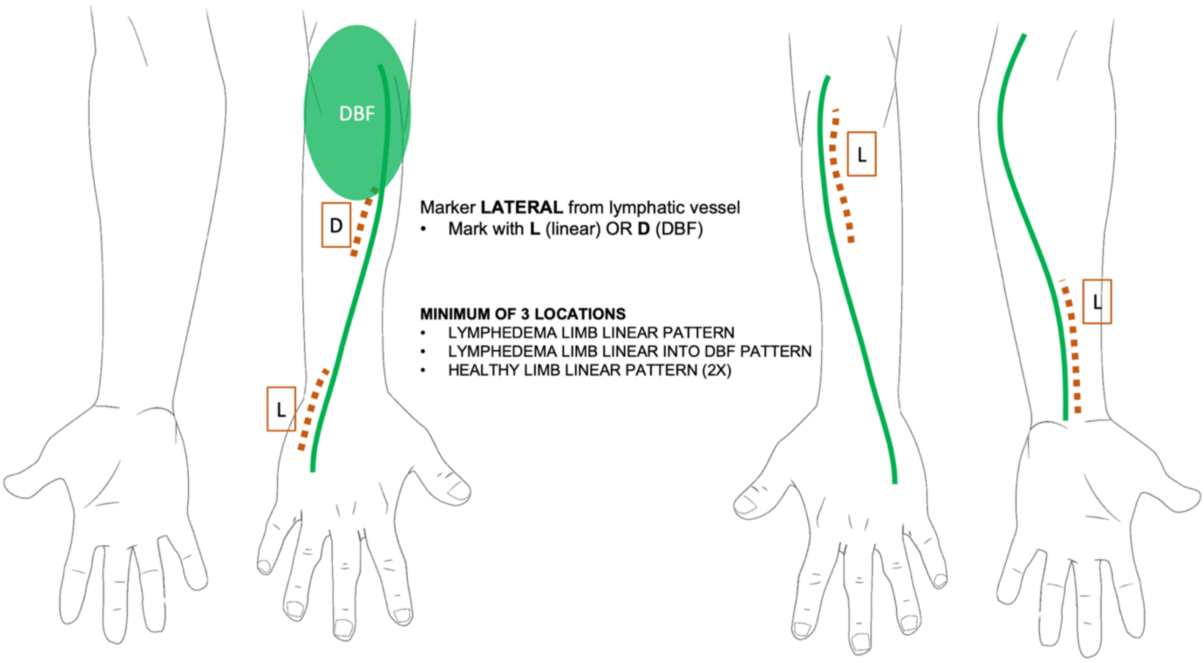

Photoacoustic imaging (Acoustic X) imaging protocol – preparation

STARTING		CHECK
Connect the probe and lock it in place. Connect the LEDs to channel 1 and channel 2 (820/940 nm).	 	Only go further if the probe and LEDs are connected
Connect the coupling piece to the probe. Connect the LEDs to the probe with the connection piece.		
Turn on the PC via the main power switch and then the front power switch.	 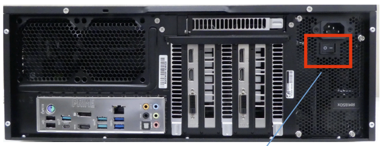 Front Power switch Main Power switch	
You will be prompted to type in the password.		
Wait until the pop-up "POWER ON" appears Turn on the Data Acquisition System via the power switch Click "Yes it's ON"	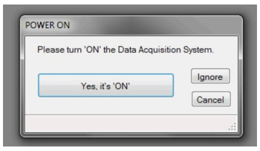  Power indication LED  Power switch	
The image acquisition software will start	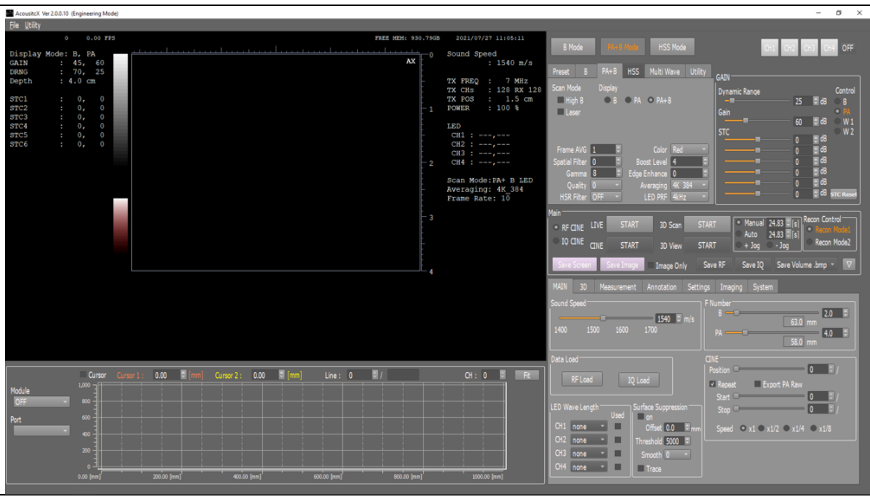	

SETTINGS		CHECK

PRESETS

Set preset to *PAI lymph_study*

Set Channel 1 and Channel 2 to 820&940 nm

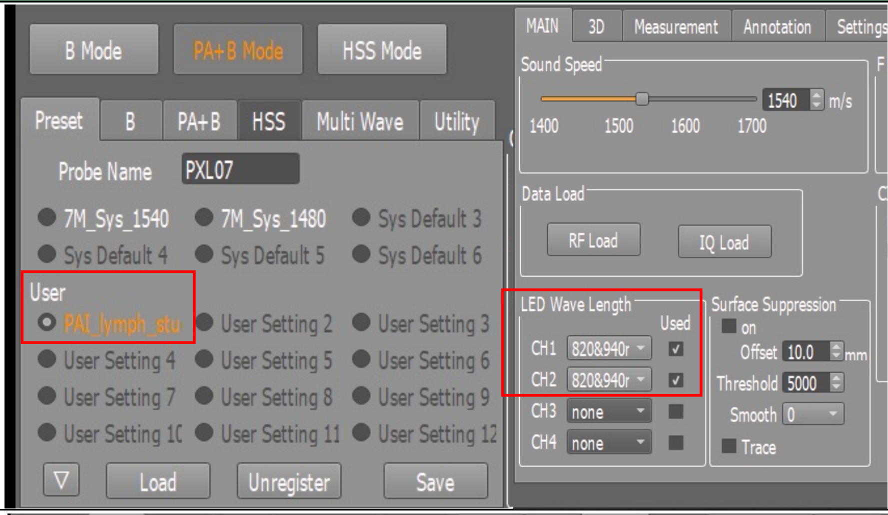

B-MODE & PA+B

Check if all settings are the same as in the images on the right.

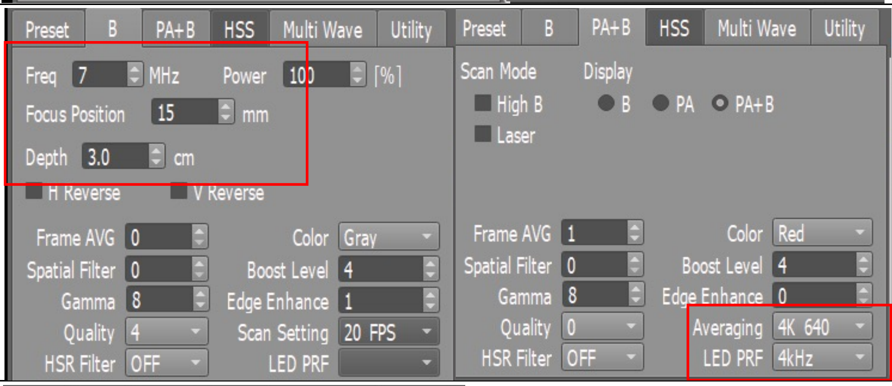

MULTI WAVE

Make sure *Toggle* is checked and preset is set to 820&940 nm.

Make sure W1 en W2 are set to 1.00

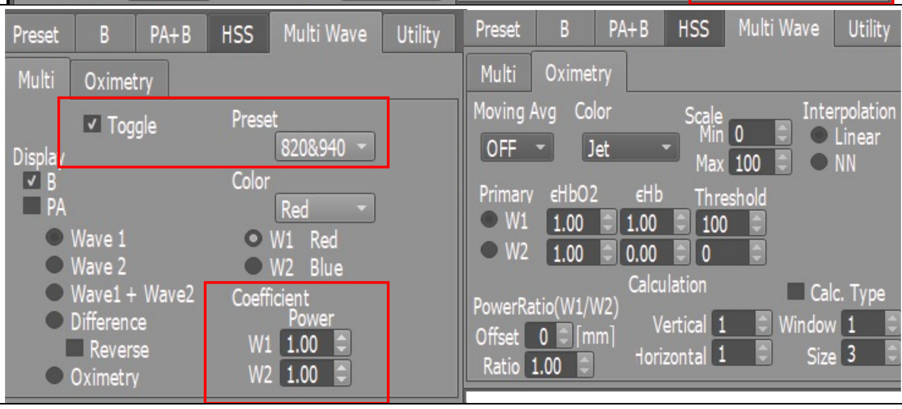

Are all settings correct?

MAKE NEW PATIENT FOLDER		CHECK
SYSTEM Change the data at *Data Location* to the patient identification code *PAI_lymph_001.* Only replace *PAI_lymph_settings* Change prefix_1 for every type of image to the correct name. Make sure the box *prefix* is checked.	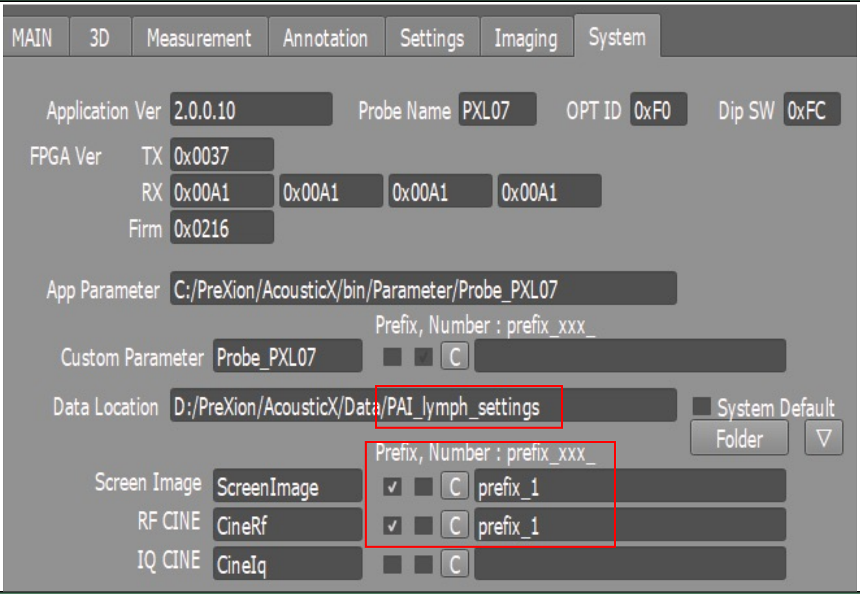	
IMAGING		**CHECK**
General steps	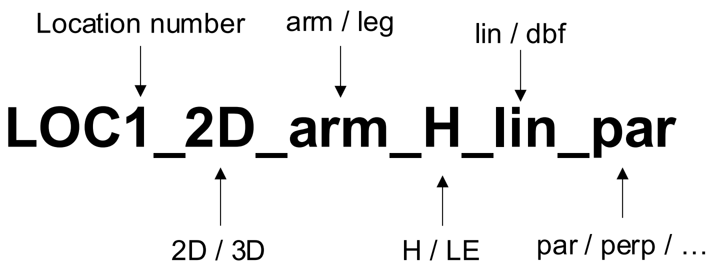 **2D (probe stationairy) AND 3D SCAN (swipe motion)** 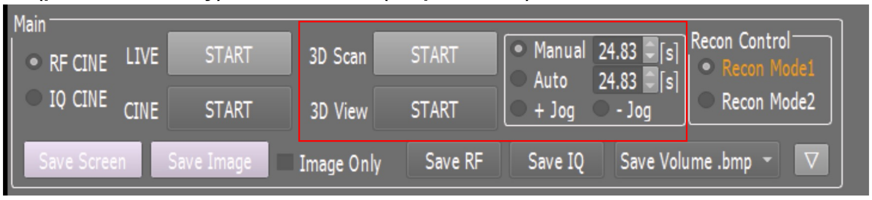 **SAVE DATA** 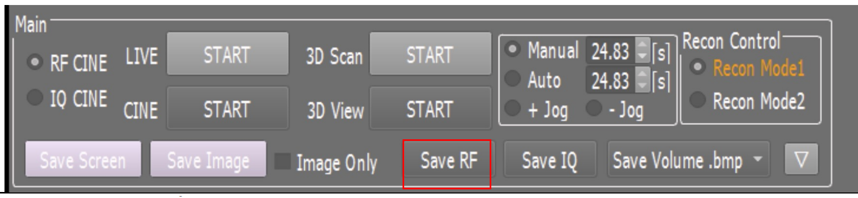	
PROBE DIRECTION Make sure that the direction mark is always pointe to the left of the patient (perpendicular scan) OR proximally in case of a parallel scan.	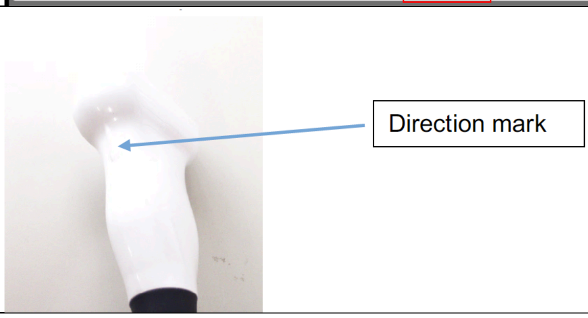	

	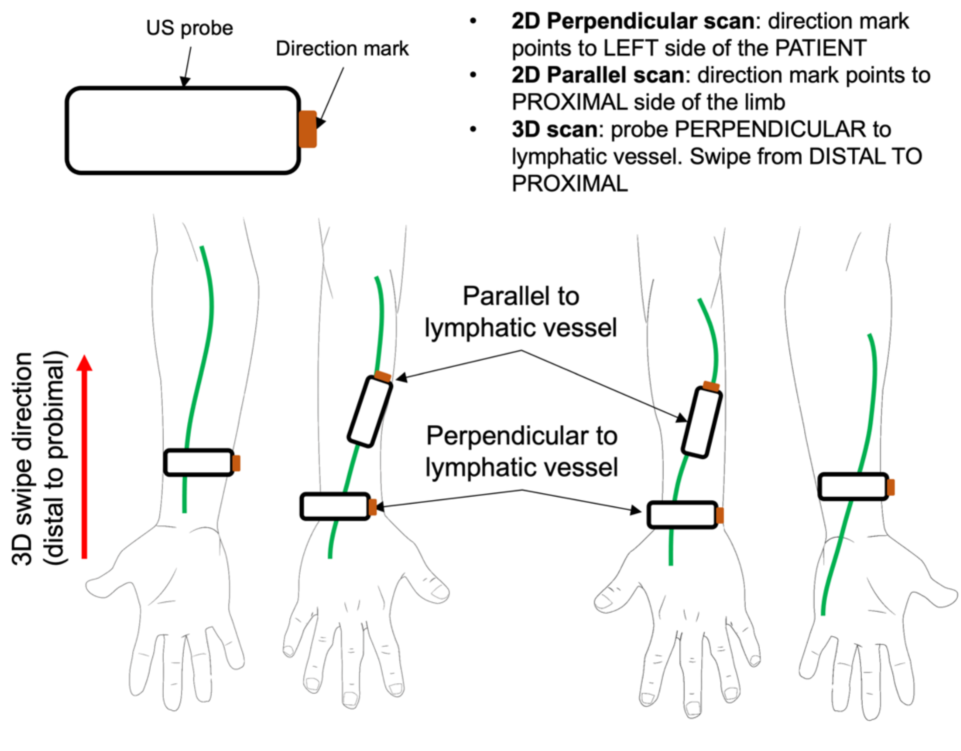US probe Direction mark • **2D Perpendicular scan**: direction mark points to LEFT side of the PATIENT • **2D Parallel scan**: direction mark points to PROXIMAL side of the limb • **3D scan**: probe PERPENDICULAR to lymphatic vessel. Swipe from DISTAL TO PROXIMAL Parallel to lymphatic vessel Perpendicular to lymphatic vessel 3D swipe direction (distal to probimal)

Photoacoustic imaging (Acoustic X) imaging protocol – execution

	INDICATE LOCATION ON LOCATION FORM Indicate the imaging location on the imaging location form on the last page of this imaging protocol. Give each location its unique number with the prefix LOC.		
	Main tab → Set Ch1+Ch2 to 820 + 940 → Check		
	Start live measurement and freeze		
LOC 1	**3D SWIPE LE LIMB (DBF)** (25 sec)	• In System tab change prefix_1 in RF CINE to ***LOC1_3D_arm/leg_LE_dbf*** • Start the 3D scan • Click Save RF	SAVE RF
	2D IMAGE LE LIMB PERPENDICULAR (DBF)	• *LOC1_**2D**_..._LE_dbf_**perp*** • Start the 3D scan: START and image the lymphatic vessel axially • Click Save RF	SAVE RF
	2D IMAGE LE LIMB PARALLEL (DBF) (4 x 25 sec min + 2 min)	• *LOC1_2D_..._LE_dbf_**par*** • Start the 3D scan • Click Save RF after every 25 second measurement • Wait for 2 min to cool down the LEDs	SAVE RF SAVE RF SAVE RF SAVE RF
	Check if files are saved correctly		
LOC 2	**3D SWIPE LE LIMB (LINEAR)** (25 sec)	• ***LOC2_3D_..._**LE_**lin*** • Start the 3D scan:START and swipe from distal to proximal in one constant movement over the lymphatic vessel. • Click Save RF	SAVE RF
	2D IMAGE LE LIMB PERPENDICULAR (LINEAR)	• *LOC2_**2D**_..._LE_lin_**perp*** • Start the 3D scan:START and image the lymphatic vessel axially • Click Save RF	SAVE RF
	2D IMAGE LE LIMB PARALLEL (LINEAR) (4 x 25 sec min + 2 min)	• *LOC2_2D_..._LE_lin_**par*** • Start the 3D scan • Click Save RF after every 25 second measurement • Wait for 2 min to cool down the LEDs	SAVE RF SAVE RF SAVE RF SAVE RF
	Check if files are saved correctly		
LOC 3	**3D SWIPE HEALTHY LIMB**	• ***LOC3_3D**_..._**H**_lin* • Start the 3D scan • Click Save RF	SAVE RF
	2D IMAGE HEALTHY LIMB PERPENDICULAR	• *LOC3_**2D**_..._H_lin_**perp*** • Start the 3D scan • Click Save RF	SAVE RF
	2D IMAGE HEALTHY LIMB PARALLEL (4 x 25 sec min + 2 min)	• *LOC3_2D_..._H_lin_**par*** • Start the 3D scan • Click Save RF after every 25 second measurement • Wait for 2 min to cool down the LEDs	SAVE RF SAVE RF SAVE RF SAVE RF
	Check if files are saved correctly		
LOC 4	**3D SWIPE HEALTHY LIMB**	• ***LOC4_3D**_..._**H**_lin* • Start the 3D scan • Click Save RF	SAVE RF
	2D IMAGE HEALTHY LIMB PERPENDICULAR	• *LOC4_**2D**_..._H_lin_**perp*** • Start the 3D scan • Click Save RF	SAVE RF
	2D IMAGE HEALTHY LIMB PARALLEL	• *LOC4_2D_..._H_lin_**par*** • Start the 3D scan • Click Save RF after every 25 second measurement	SAVE RF SAVE RF SAVE RF

	(4 x 25 sec min + 2 min)	• Wait for 2 min to cool down the LEDs	SAVE RF
	RESTART	• Click Exit • Wait for device to restart	All files saved correctly?
CHECK IF THE DEVICE IS TURNED OFF			2 people agree?
CLEANING			

Transfer the data

At the end of the day:

- Transfer the pseudonymized data from the Acoustic X to the PAI lymph study encrypted hard drive
- Transfer the pseudonymized data from the Photodynamic Eye to the PAI lymph study encrypted hard drive
- Transfer the data from the encrypted hard drive to the permanent storage location (Research Suite Storage)

Location form

Subject ID: ___________________________

Date: ________________________________

Side of lymphedema: Left / Right

INDICATE AT LEAST THE FOLLOWING 4 LOCATIONS

- HEALTHY LIMB LINEAR PATTERN (2X)
- LYMPHEDEMA LIMB LINEAR PATTERN
- LYMPHEDEMA LIMB LINEAR INTO DBF PATTERN

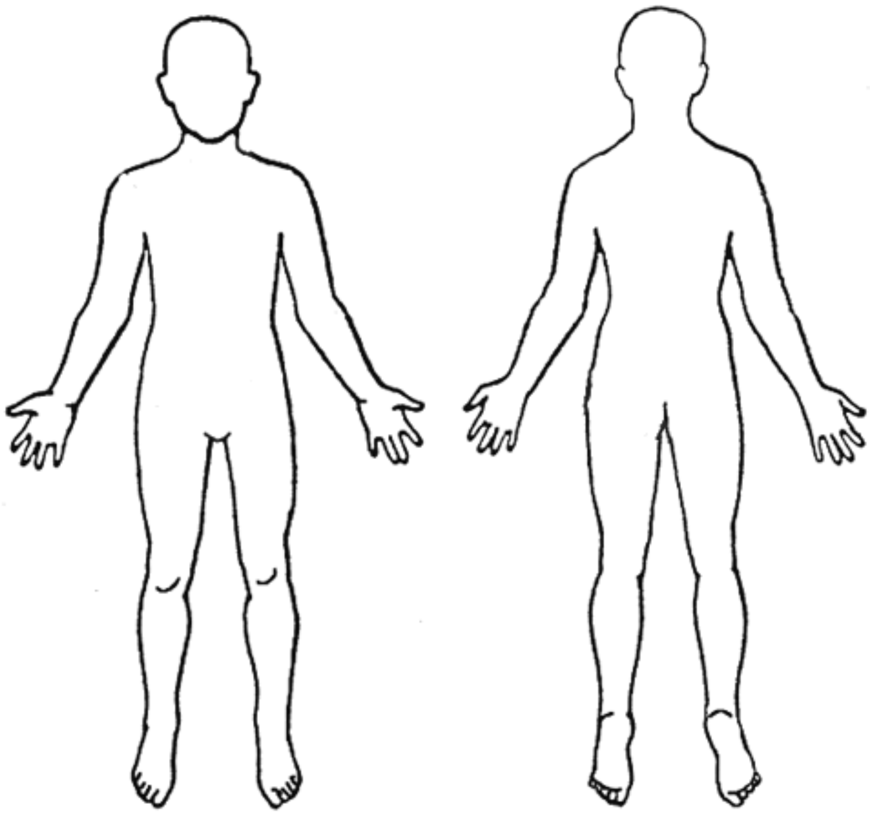

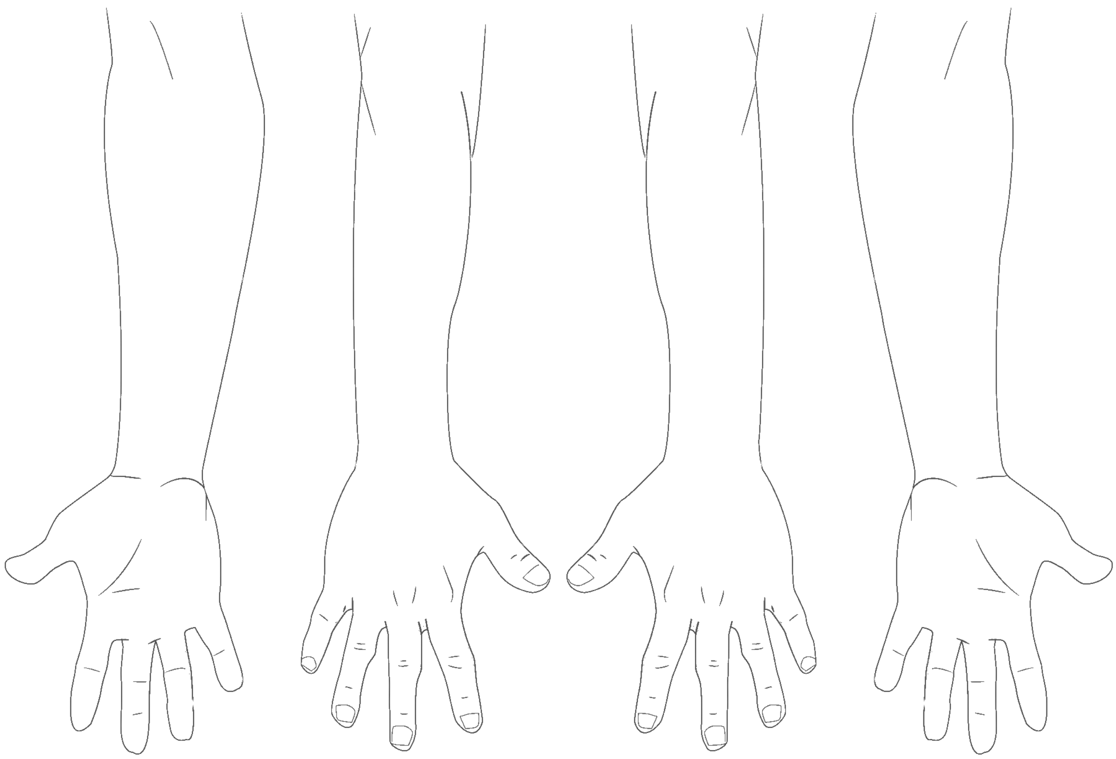

References

1 Bourgeois, P., Peters, E., Van Mieghem, A. et al. Edemas of the face and lymphoscintigraphic examination. *Sci. rep.* 2021;(11):6444.
2 Pappalardo, M., Lin, C., Ho, O. A. et al. Staging and clinical correlations of lymphoscintigraphy for unilateral gynecological cancer-related lymphedema. *J. Surg. Oncol.* 2020;(121):422-434.
3 Campisi, C. C., Ryan, M., Villa, G. et al. Rationale for Study of the Deep Subfascial Lymphatic Vessels During Lymphoscintigraphy for the Diagnosis of Peripheral Lymphedema. *Clin. Nucl. Med.* 2019;(44):91-98, doi:10.1097/rlu.0000000000002400.
4 Tartaglione, G., Visconti, G., Bartoletti, R. et al. Stress lymphoscintigraphy for early detection and management of secondary limb lymphedema. *Clin. Nucl. Med.* 2018;(43):155-161, doi:10.1097/rlu.0000000000001963.
5 Cheng, M. H., Pappalardo, M., Lin, C. et al. Validity of the Novel Taiwan Lymphoscintigraphy Staging and Correlation of Cheng Lymphedema Grading for Unilateral Extremity Lymphedema. *Ann. Surg.* 2018;(268):513-525, doi:10.1097/sla.0000000000002917.
6 Maclellan, R. A., Zurakowski, D., Voss, S. et al. Correlation Between Lymphedema Disease Severity and Lymphoscintigraphic Findings: A Clinical-Radiologic Study. *J. Am. Coll. Surg.* 2017;(225):366-370, doi:10.1016/j.jamcollsurg.2017.06.005.
7 Hassanein, A. H., Maclellan, R. A., Grant, F. D. et al. Diagnostic Accuracy of Lymphoscintigraphy for Lymphedema and Analysis of False-Negative Tests. *Plast. reconstr. surg., Glob. open.* 2017;(5).
8 Yoo, J. N., Cheong, Y. S., Min, Y. S. et al. Validity of Quantitative Lymphoscintigraphy as a Lymphedema Assessment Tool for Patients With Breast Cancer. *Ann. Rehabil. Med.* 2015;(39):931-940.
9 Devoogdt, N., Van Den Wyngaert, T., Bourgeois, P. et al. Reproducibility of lymphoscintigraphic evaluation of the upper limb. *Lymphatic. Res. Biol.* 2014;(12):175-184, doi:10.1089/lrb.2013.0034.
10 Kalawat, T. C., Chittoria, R. K., Reddy, P. K. et al. Role of lymphoscintigraphy in diagnosis and management of patients with leg swelling of unclear etiology. *Indian. J. Nucl. Med.* 2012;(27):226-230, doi:10.4103/0972-3919.115392.
11 Infante, J. R., García, L., Laguna, P. et al. Lymphoscintigraphy for differential diagnosis of peripheral edema: Diagnostic yield of different scintigraphic patterns. *Rev. Esp. Med. Nucl. Imagen. Mol.* 2012;(31):237-242, doi:10.1016/j.remn.2011.11.011.
12 Mikami, T., Hosono, M., Yabuki, Y. et al. Classification of lymphoscintigraphy and relevance to surgical indication for lymphaticovenous anastomosis in upper limb lymphedema. *Lymphology.* 2011;(44):155-167.
13 Maegawa, J., Mikami, T., Yamamoto, Y. et al. Types of lymphoscintigraphy and indications for lymphaticovenous anastomosis. *Microsurgery.* 2010;(30):437-442, doi:10.1002/micr.20772.
14 Pecking, A. P., Albérini, J. L., Wartski, M. et al. Relationship between lymphoscintigraphy and clinical findings in lower limb lymphedema (LO): Toward a comprehensive staging. *Lymphology.* 2008;(41):1-10.
15 Dabrowski, J., Merkert, R. & Kuśmierek, J. Optimized lymphoscintigraphy and diagnostics of lymphatic oedema of the lower extremities. *Nucl. Med. Rev.* 2008;(11):26-29.
16 Williams, W. H., Witte, C. L., Witte, M. H. et al. Radionuclide lymphangioscintigraphy in the evaluation of peripheral lymphedema. *Clin. Nucl. Med.* 2000;(25):451-464, doi:10.1097/00003072-200006000-00013.
17 Kim, Y. H., Hwang, J. H., Bae, J. H. et al. Predictive value of lymphoscintigraphy in patients with breast cancer-related lymphedema undergoing complex decongestive therapy. *Breast. Cancer. Res. Treat.* 2019;(173):735-741, doi:10.1007/s10549-018-5041-2.
18 Chiewvit, S. & Kumnerdnakta, S. Lymphoscintigraphic findings that predict favorable outcome after lymphaticovenous anastomosis. *Lymphology.* 2017;(50):1-8.
19 Tartaglione, G., Pagan, M., Morese, R. et al. Intradermal lymphoscintigraphy at rest and after exercise: A new technique for the functional assessment of the lymphatic system in patients with lymphoedema. *Nucl. Med. Commun.* 2010;(31):547-551, doi:10.1097/MNM.0b013e328338277d.
20 O'Mahony, S., Solanki, C. K., Barber, R. W. et al. Imaging of lymphatic vessels in breast cancer-related lymphedema: Intradermal versus subcutaneous injection of 99mTc-immunoglobulin. *Am. J. Roentgenol.* 2006;(186):1349-1355, doi:10.2214/ajr.04.1341.
21 O'Mahony, S., Rose, S. L., Chilvers, A. J. et al. Finding an optimal method for imaging lymphatic vessels of the upper limb. *Eur. J. Nucl. Med. Mol. Imaging.* 2004;(31):555-563, doi:10.1007/s00259-003-1399-3.
22 Stanton, A. W., Mellor, R. H., Cook, G. J. et al. Impairment of lymph drainage in subfascial compartment of forearm in breast cancer-related lymphedema. *Lymphat. Res. Biol.* 2003;(1):121-132, doi:10.1089/153968503321642615.
23 Baulieu, F., Tauveron, V., Erra, B. et al. Lymphoscintigraphy in limb lymphoedema: Current methodology and interests. *Med Nucl.* 2015;(39):26-42, doi:10.1016/j.mednuc.2015.02.009.
24 Baulieu, F., Bourgeois, P., Maruani, A. et al. Contributions of SPECT/CT imaging to the lymphoscintigraphy investigations of the lower limb lymphedema. *Lymphology.* 2013;(46):106-119.
25 Pecking, A. P., Wartski, M., Cluzan, R. V. et al. SPECT-CT fusion imaging radionuclide lymphoscintigraphy: potential for limb lymphedema assessment and sentinel node detection in breast cancer. *Cancer. Treat. Res.* 2007;(135):79-84.
26 Jørgensen, M. G., Toyserkani, N. M., Hansen, F. C. G. et al. Prospective validation of indocyanine green lymphangiography staging of breast cancer-related lymphedema. *Cancers.* 2021;(13), doi:10.3390/cancers13071540.
27 Thomis, S., Dams, L., Fourneau, I. et al. Correlation between Clinical Assessment and Lymphofluoroscopy in Patients with Breast Cancer-Related Lymphedema: A Study of Concurrent Validity. *Lymphatic. Res. Biol.* 2020;(18):539-548, doi:10.1089/lrb.2019.0090.

28 Medina-Rodríguez, M. E., de-la-Casa-Almeida, M., Mena-Rodríguez, A. et al. Relationship between perimetric increase and fluoroscopic pattern type in secondary upper limb lymphedema observed by Indocyanine green lymphography. *Medicine (Baltimore).* 2020;(99):e20432, doi:10.1097/md.0000000000020432.
29 Kinugawa, K., Nuri, T., Iwanaga, H. et al. Lymph Vessel Mapping Using Indocyanine Green Lymphography in the Nonaffected Side of Lower Leg. *Plast. reconstr. surg., Glob. open.* 2020;(8):e2929.
30 Lee, Y. W., Lee, S. H., You, H. J. et al. Lymphatic vessel mapping in the upper extremities of a healthy Korean population. *Arch. Plast. Surg.* 2018;(45):152-157, doi:10.5999/aps.2017.00983.
31 Suami, H., Heydon-White, A., Mackie, H. et al. A new indocyanine green fluorescence lymphography protocol for identification of the lymphatic drainage pathway for patients with breast cancer-related lymphoedema. *BMC Cancer.* 2019;(19), doi:10.1186/s12885-019-6192-1.
32 Matsumoto, K., Shinaoka, A., Yamada, K. et al. Exercise-Loaded Indocyanine Green Fluorescence Lymphangiography for Diagnosing Lymphedema. *J. Reconstr. Microsurg.* 2019;(35):138-144, doi:10.1055/s-0038-1667366.
33 Garza, R. M., Ooi, A. S. H., Falk, J. et al. The Relationship Between Clinical and Indocyanine Green Staging in Lymphedema. *Lymphat. Res. Biol.* 2019;(17):329-333.
34 Shinaoka, A., Koshimune, S., Yamada, K. et al. Accelerated Lymph Flow in Early-Stage Secondary Lymphedema Detected by Indocyanine Green Fluorescence Lymphography. *J. Reconstr. Microsurg.* 2017;(33):596-602, doi:10.1055/s-0037-1603740.
35 Gentileschi, S., Servillo, M., Albanese, R. et al. Lymphatic mapping of the upper limb with lymphedema before lymphatic supermicrosurgery by mirroring of the healthy limb. *Microsurgery.* 2017;(37):881-889, doi:10.1002/micr.30247.
36 Tashiro, K., Yamashita, S., Saito, T. et al. Proximal and distal patterns: Different spreading patterns of indocyanine green lymphography in secondary lower extremity lymphedema. *J. Plast. Reconstr. Aesthetic. Surg.* 2016;(69):368-375, doi:10.1016/j.bjps.2015.10.042.
37 Akita, S., Nakamura, R., Yamamoto, N. et al. Early Detection of Lymphatic Disorder and Treatment for Lymphedema following Breast Cancer. *Plast. Reconstr. Surg.* 2016;(138):192e-202e, doi:10.1097/prs.0000000000002337.
38 Mihara, M., Seki, Y., Hara, H. et al. Predictive lymphatic mapping: a method for mapping lymphatic channels in patients with advanced unilateral lymphedema using indocyanine green lymphography. *Ann Plast Surg.* 2014;(72):706-710, doi:10.1097/SAP.0b013e31826a18b1.
39 Mihara, M., Hayashi, Y., Hara, H. et al. High-accuracy diagnosis and regional classification of lymphedema using indocyanine green fluorescent lymphography after gynecologic cancer treatment. *Ann Plast Surg.* 2014;(72):204-208.
40 Akita, S., Mitsukawa, N., Rikihisa, N. et al. Early diagnosis and risk factors for lymphedema following lymph node dissection for gynecologic cancer. *Plast. Reconstr. Surg.* 2013;(131):283-290.
41 Suami, H., Chang, D., Skoracki, R. et al. Using indocyanine green fluorescent lymphography to demonstrate lymphatic architecture. *J. Lymphoedema.* 2012;(7):25-29.
42 Aldrich, M. B., Guilliod, R., Fife, C. E. et al. Lymphatic abnormalities in the normal contralateral arms of subjects with breast cancer-related lymphedema as assessed by near-infrared fluorescent imaging. *Biomed. Opt. Express.* 2012;(3):1256-1265.
43 Yamamoto, T., Matsuda, N., Doi, K. et al. The earliest finding of indocyanine green lymphography in asymptomatic limbs of lower extremity lymphedema patients secondary to cancer treatment: the modified dermal backflow stage and concept of subclinical lymphedema. *Plast. Reconstr. Surg.* 2011;(128):314e-321e.
44 Yamamoto, T., Yamamoto, N., Doi, K. et al. Indocyanine green-enhanced lymphography for upper extremity lymphedema: a novel severity staging system using dermal backflow patterns. *Plast. Reconstr. Surg.* 2011;(128):941-947.
45 Yamamoto, T., Narushima, M., Doi, K. et al. Characteristic indocyanine green lymphography findings in lower extremity lymphedema: the generation of a novel lymphedema severity staging system using dermal backflow patterns. *Plast. Reconstr. Surg.* 2011;(127):1979-1986.
46 Unno, N., Inuzuka, K., Suzuki, M. et al. Preliminary experience with a novel fluorescence lymphography using indocyanine green in patients with secondary lymphedema. *J. Vasc. Surg.* 2007;(45):1016-1021, doi:10.1016/j.jvs.2007.01.023.
47 Johnson, A. R., Granoff, M. D., Suami, H. et al. Real-time visualization of the mascagni-sappey pathway utilizing ICG lymphography. *Cancers.* 2020;(12), doi:10.3390/cancers12051195.
48 Tashiro, K., Yamashita, S., Koshima, I. et al. Visualization of Accessory Lymphatic Pathways in Secondary Upper Extremity Lymphedema Using Indocyanine Green Lymphography. *Ann. Plast. Surg.* 2017;(79):393-396, doi:10.1097/sap.0000000000001120.
49 Kelly, B., Mohanakumar, S., Telinius, N. et al. Function of Upper Extremity Human Lymphatics Assessed by Near-Infrared Fluorescence Imaging. *Lymphat. Res. Biol.* 2020;(18):226-231.
50 Granoff, M. D., Johnson, A. R., Lee, B. T. et al. A Novel Approach to Quantifying Lymphatic Contractility during Indocyanine Green Lymphangiography. *Plast. Reconstr. Surg.* 2019;(144):1197-1201, doi:10.1097/prs.0000000000006176.
51 Groenlund, J. H., Telinius, N., Skov, S. N. et al. A Validation Study of Near-Infrared Fluorescence Imaging of Lymphatic Vessels in Humans. *Lymphat. Res. Biol.* 2017;(15):227-234.
52 Yamamoto, T., Narushima, M., Yoshimatsu, H. et al. Dynamic Indocyanine Green (ICG) lymphography for breast cancer-related arm lymphedema. *Ann. Plast. Surg.* 2014;(73):706-709, doi:10.1097/SAP.0b013e318285875f.
53 Yamamoto, T., Narushima, M., Yoshimatsu, H. et al. Indocyanine green velocity: lymph transportation capacity deterioration with progression of lymphedema. *Ann. Plast. Surg.* 2013;(71):591-594.
54 Rasmussen, J. C., Tan, I., Marshall, M. V. et al. Human lymphatic architecture and dynamic transport imaged using near-infrared fluorescence. *Transl. Oncol.* 2010;(3):362-372, doi:10.1593/tlo.10190.

55 Unno, N., Nishiyama, M., Suzuki, M. et al. Quantitative lymph imaging for assessment of lymph function using indocyanine green fluorescence lymphography. *Eur. J. Vasc. Endovasc. Surg.* 2008;(36):230-236.

56 Hara, H. & Mihara, M. Multilymphosome injection indocyanine green lymphography can detect more lymphatic vessels than lymphoscintigraphy in lymphedematous limbs. *J. Plast. Reconstr. Aesthetic. Surg.* 2020;(73):1025-1030, doi:10.1016/j.bjps.2020.01.021.

57 Hara, H. & Mihara, M. Multi-area lymphaticovenous anastomosis with multi-lymphosome injection in indocyanine green lymphography: A prospective study. *Microsurgery.* 2019;(39):167-173, doi:10.1002/micr.30398.

58 Hara, H., Mihara, M., Seki, Y. et al. Comparison of indocyanine green lymphographic findings with the conditions of collecting lymphatic vessels of limbs in patients with lymphedema. *Plast. Reconstr. Surg.* 2013;(132):1612-1618.

59 Yoon, J. A., Shin, M. J. & Kim, J. H. Indocyanine green lymphography and lymphoscintigraphy severity stage showed strong correlation in lower limb lymphedema. *Lymphatic. Res. Biol.* 2021;(19):80-85, doi:10.1089/lrb.2020.0043.

60 Yoon, J. A., Shin, M. J., Shin, Y. B. et al. Correlation of ICG lymphography and lymphoscintigraphy severity stage in secondary upper limb lymphedema. *J. Plast. Reconstr. Aesthetic. Surg.* 2020;(73):1982-1988, doi:10.1016/j.bjps.2020.08.055.

61 Mihara, M., Hara, H., Narushima, M. et al. Indocyanine green lymphography is superior to lymphoscintigraphy in imaging diagnosis of secondary lymphedema of the lower limbs. *J. Vasc. Surg. Venous. Lymphatic. Disord.* 2013;(1):194-201, doi:10.1016/j.jvsv.2012.07.011.

62 Akita, S., Mitsukawa, N., Kazama, T. et al. Comparison of lymphoscintigraphy and indocyanine green lymphography for the diagnosis of extremity lymphoedema. *J. Plast. Reconstr. Aesthetic. Surg.* 2013;(66):792-798, doi:10.1016/j.bjps.2013.02.023.

63 Soga, S., Onishi, F., Jinzaki, M. et al. Analysis of collateral lymphatic circulation in patients with lower limb lymphedema using magnetic resonance lymphangiography. *J. Vasc. Surg. Venous. Lymphati.c Disord.* 2021;(9):471-481.e471, doi:10.1016/j.jvsv.2020.04.029.

64 Sheng, L., Zhang, G., Li, S. et al. Magnetic Resonance Lymphography of Lymphatic Vessels in Upper Extremity With Breast Cancer-Related Lymphedema. *Ann. Plast. Surg.* 2020;(84):100-105, doi:10.1097/sap.0000000000001994.

65 Abdelfattah, U., Jaimez, P. M., Clavero, J. A. et al. Correlation between superficial and deep lymphatic systems using magnetic resonance lymphangiography in breast cancer-related lymphedema: Clinical implications. *J. Plast. Reconstr. Aesthetic. Surg.* 2020;(73):1018-1024, doi:10.1016/j.bjps.2019.11.053.

66 Ripley, B., Wilson, G. J., Lalwani, N. et al. Initial clinical experience with dual-agent relaxation contrast for isolated lymphatic channel mapping. *Radiology.* 2018;(286):705-714, doi:10.1148/radiol.2017170241.

67 Gennaro, P., Borghini, A., Chisci, G. et al. Could MRI visualize the invisible? An Italian single center study comparing magnetic resonance lymphography (MRL), super microsurgery and histology in the identification of lymphatic vessels. *Eur. Rev. Med. Pharmacol. Sci.* 2017;(21):687-694.

68 Jeon, J. Y., Lee, S. H., Shin, M. J. et al. Three-dimensional isotropic fast spin-echo MR lymphangiography of T1-weighted and intermediate-weighted pulse sequences in patients with lymphoedema. *Clin. Radiol.* 2016;(71):e56-e63, doi:10.1016/j.crad.2015.10.015.

69 Liu, N. & Zhang, Y. Magnetic Resonance Lymphangiography for the Study of Lymphatic System in Lymphedema. *J. Reconstr. Microsurg.* 2016;(32):66-71, doi:10.1055/s-0034-1384213.

70 Borri, M., Schmidt, M. A., Gordon, K. D. et al. Quantitative Contrast-Enhanced Magnetic Resonance Lymphangiography of the Upper Limbs in Breast Cancer Related Lymphedema: An Exploratory Study. *Lymphatic. Res. Biol.* 2015;(13):100-106, doi:10.1089/lrb.2014.0039.

71 Zhou, G. X., Chen, X., Zhang, J. H. et al. MR lymphangiography at 3.0 Tesla to assess the function of inguinal lymph node in low extremity lymphedema. *J. Magn. Reson. Imaging.* 2014;(40):1430-1436, doi:10.1002/jmri.24499.

72 Liu, N. F., Yan, Z. X., Wu, X. F. et al. Magnetic resonance lymphography demonstrates spontaneous lymphatic disruption and regeneration in obstructive lymphedema. *Lymphology.* 2013;(46):56-63.

73 Lu, Q., Delproposto, Z., Hu, A. et al. MR Lymphography of Lymphatic Vessels in Lower Extremity with Gynecologic Oncology-Related Lymphedema. *PLoS One.* 2012;(7), doi:10.1371/journal.pone.0050319.

74 Notohamiprodjo, M., Baumeister, R. G. H., Jakobs, T. F. et al. MR-lymphangiography at 3.0T - A feasibility study. *Eur. Radiol.* 2009;(19):2771-2778, doi:10.1007/s00330-009-1461-z.

75 Dimakakos, E. P., Koureas, A., Koutoulidis, V. et al. Interstitial magnetic resonance lymphography: The clinical effectiveness of a new method. *Lymphology.* 2008;(41):116-125.

76 Lohrmann, C., Foeldi, E., Bartholomae, J. P. et al. Gadoteridol for MR imaging of lymphatic vessels in lymphoedematous patients: Initial experience after intracutaneous injection. *Br. J. Radiol.* 2007;(80):569-573, doi:10.1259/bjr/95414884.

77 Lohrmann, C., Foeldi, E., Bartholomä, J. P. et al. Magnetic resonance imaging of lymphatic vessels without image subtraction: A practicable imaging method for routine clinical practice? *J. Comput. Assisted. Tomogr.* 2007;(31):303-308, doi:10.1097/01.rct.0000237814.33925.32.

78 Lohrmann, C., Föld, E., Bartholomä, J. P. et al. MR imaging of the lymphatic system: Distribution and contrast enhancement of gadodiamide after intradermal injection. *Lymphology.* 2006;(39):156-163.

79 Lohrmann, C., Foeldi, E., Speck, O. et al. High-resolution MR lymphangiography in patients with primary and secondary lymphedema. *Am. J. Roentgenol.* 2006;(187):556-561.

80 Lohrmann, C., Foeldi, E. & Langer, M. Indirect magnetic resonance lymphangiography in patients with lymphedema. Preliminary results in humans. *Eur. J. Radiol.* 2006;(59):401-406, doi:10.1016/j.ejrad.2006.02.012.

81 Yasunaga, Y., Nakajima, Y., Mimura, S. et al. Magnetic resonance lymphography as three-dimensional navigation for lymphaticovenular anastomosis in patients with leg lymphedema. *J. Plast. Reconstr. Aesthetic. Surg.* 2020, doi:10.1016/j.bjps.2020.10.099.

82 Pons, G., Clavero, J. A., Alomar, X. et al. Preoperative planning of lymphaticovenous anastomosis: The use of magnetic resonance lymphangiography as a complement to indocyanine green lymphography. *J. Plast. Reconstr. Aesthet. Surg.* 2019;(72):884-891.
83 Zeltzer, A. A., Brussaard, C., Koning, M. et al. MR lymphography in patients with upper limb lymphedema: The GPS for feasibility and surgical planning for lympho-venous bypass. *J. Surg. Oncol.* 2018;(118):407-415, doi:10.1002/jso.25145.
84 Mazzei, M. A., Gentili, F., Mazzei, F. G. et al. High-resolution MR lymphangiography for planning lymphaticovenous anastomosis treatment: a single-centre experience. *Radiol. Med.* 2017;(122):918-927, doi:10.1007/s11547-017-0795-x.
85 Bae, J. S., Yoo, R. E., Choi, S. H. et al. Evaluation of lymphedema in upper extremities by MR lymphangiography: Comparison with lymphoscintigraphy. *Magn. Reson. Imaging.* 2018;(49):63-70, doi:10.1016/j.mri.2017.12.024.
86 Weiss, M., Burgard, C., Baumeister, R. et al. Magnetic resonance imaging versus lymphoscintigraphy for the assessment of focal lymphatic transport disorders of the lower limb: First experiences. *Nuklearmedizin.* 2014;(53):190-196, doi:10.3413/Nukmed-0649-14-03.
87 Notohamiprodjo, M., Weiss, M., Baumeister, R. G. et al. MR lymphangiography at 3.0 T: Correlation with lymphoscintigraphy. *Radiology.* 2012;(264):78-87, doi:10.1148/radiol.12110229.
88 Cellina, M., Martinenghi, C., Panzeri, M. et al. Noncontrast MR Lymphography in Secondary Lower Limb Lymphedema. *J. Magn. Reson. Imaging.* 2020, doi:10.1002/jmri.27328.
89 Cellina, M., Gibelli, D., Martinenghi, C. et al. Noncontrast Magnetic Resonance Lymphography in Secondary Lymphedema Due to Prostate Cancer. *Lymphat. Res. Biol.* 2020, doi:10.1089/lrb.2020.0034.
90 Crescenzi, R., Donahue, P. M. C., Hartley, K. G. et al. Lymphedema evaluation using noninvasive 3T MR lymphangiography. *J. Magn. Reson. Imaging.* 2017;(46):1349-1360, doi:10.1002/jmri.25670.
91 Liu, N., Wang, C. & Sun, M. Noncontrast three-dimensional magnetic resonance imaging vs lymphoscintigraphy in the evaluation of lymph circulation disorders: A comparative study. *J. Vasc. Surg.* 2005;(41):65-75, doi:10.1016/j.jvs.2004.11.013.
92 Hou, G., Hou, B., Jiang, Y. et al. 68Ga-NOTA-Evans Blue TOF PET/MR Lymphoscintigraphy Evaluation of the Severity of Lower Limb Lymphedema. *Clin. Nucl. Med.* 2019;(44):439-445, doi:10.1097/rlu.0000000000002584.
93 Long, X., Zhang, J., Zhang, D. et al. Microsurgery guided by sequential preoperative lymphography using 68Ga-NEB PET and MRI in patients with lower-limb lymphedema. *Eur. J. Nucl. Med. Mol. Imaging.* 2017;(44):1501-1510, doi:10.1007/s00259-017-3676-6.
94 Hara, H. & Mihara, M. Diagnosis of Lymphatic Dysfunction by Evaluation of Lymphatic Degeneration with Lymphatic Ultrasound. *Lymphat. Res. Biol.* 2021, doi:10.1089/lrb.2019.0071.
95 Hara, H. & Mihara, M. Change of the Lymphatic Diameter in Different Body Positions. *Lymphat. Res. Biol.* 2020, doi:10.1089/lrb.2020.0081.
96 Czedik-Eysenberg, M., Steinbacher, J., Obermayer, B. et al. Exclusive use of ultrasound for locating optimal LVA sites—A descriptive data analysis. *J. Surg. Oncol.* 2020;(121):51-56, doi:10.1002/jso.25728.
97 Bianchi, A., Visconti, G., Hayashi, A. et al. Ultra-High frequency ultrasound imaging of lymphatic channels correlates with their histological features: A step forward in lymphatic surgery. *J. Plast. Reconstr. Aesthetic. Surg.* 2020;(73):1622-1629, doi:10.1016/j.bjps.2020.05.053.
98 Hayashi, A., Giacalone, G., Yamamoto, T. et al. Ultra High-frequency Ultrasonographic Imaging with 70 MHz Scanner for Visualization of the Lymphatic Vessels. *Plast. reconstr. surg., Glob. open.* 2019;(7):e2086.
99 Mihara, M., Hara, H. & Kawakami, Y. Ultrasonography for classifying lymphatic sclerosis types and deciding optimal sites for lymphatic-venous anastomosis in patients with lymphoedema. *J. Plast. Reconstr. Aesthet. Surg.* 2018;(71):1274-1281.
100 Hayashi, A., Hayashi, N., Yoshimatsu, H. et al. Effective and efficient lymphaticovenular anastomosis using preoperative ultrasound detection technique of lymphatic vessels in lower extremity lymphedema. *J. Surg. Oncol.* 2018;(117):290-298, doi:10.1002/jso.24812.
101 Hayashi, A., Yamamoto, T., Yoshimatsu, H. et al. Ultrasound visualization of the lymphatic vessels in the lower leg. *Microsurgery.* 2016;(36):397-401.
102 The european parliament and the council of the european union. *REGULATION (EU) 2017/745 OF THE EUROPEAN PARLIAMENT AND OF THE COUNCIL of 5 April 2017 on medical devices, amending Directive 2001/83/EC, Regulation (EC) No 178/2002 and Regulation (EC) No 1223/2009 and repealing Council Directives 90/385/EEC and 93/42/EEC.* Official Journal of the European Union (2017).
103 CCMO. *Validering door CCMO van klinisch onderzoek voor conformiteitsdoeleinden*, <https://www.ccmo.nl/onderzoekers/klinisch-onderzoek-naar-medische-hulpmiddelen/primaire-indiening-onderzoek-medische-hulpmiddelen/validering-door-ccmo-van-klinisch-onderzoek-voor-conformiteitsdoeleinden> (2021) Accessed 08 September 2021.
104 CCMO. *Klinisch onderzoek: definitie en kaders*, <https://www.ccmo.nl/onderzoekers/klinisch-onderzoek-naar-medische-hulpmiddelen/wet-en-regelgeving-richtsnoeren-en-standaarden-voor-onderzoek-medische-hulpmiddelen/klinisch-onderzoek-definitie-en-kaders> (2021) Accessed 08 September 2021.
105 Xia, W., Kuniyil Ajith Singh, M., Maneas, E. et al. Handheld Real-Time LED-Based Photoacoustic and Ultrasound Imaging System for Accurate Visualization of Clinical Metal Needles and Superficial Vasculature to Guide Minimally Invasive Procedures. *Sensors (Basel).* 2018;(18):1394, doi:10.3390/s18051394.